Optical *in-situ* analysis of the cavitation damage on technical alloys under repeated single bubbles

Von der Fakultät für Ingenieurwissenschaften, Abteilung Maschinenbau und Verfahrenstechnik der

Universität Duisburg-Essen

zur Erlangung des akademischen Grades

eines

Doktors der Ingenieurwissenschaften

Dr.-Ing.

genehmigte Dissertation

von

Jonas Kühlmann

aus

Bielefeld

Gutachter: Univ.-Prof. Dr.-Ing. Sebastian Kaiser

Univ.-Prof. Dr.-Ing. Romuald Skoda

Tag der mündlichen Prüfung: 30.10.2024

DOI: 10.17185/duepublico/82609
URN: urn:nbn:de:hbz:465-20241127-104007-6

Acknowledgment

I'm deeply grateful to my supervisor, Prof. Sebastian A. Kaiser, for his support, guidance, and accessibility throughout my journey. His open-door policy and willingness to discuss my work have been invaluable, shaping my understanding and improving my research.

I also want to thank our project partner, Prof. Stefanie Hanke, for her insights and collaboration. Additionally, I'm very grateful to my colleague, Christina Lopez, whose contributions have greatly enriched our work.

All my colleagues, especially Niklas Jüngst and Judith Laichter, deserve my deepest thanks for their friendship, support and teamwork, which made working on this project truly rewarding at all times. I would also like to thank Erdal Akyildiz, Jörg Albrecht, Natascha Schlösser, and Joel Albrecht for their support with the experiment and for providing the experimental infrastructure. I would like to extend my gratitude to Barbara Nota, Barbara Graf, Kerstin Czaplinski, and Sonay Saritas for their exemplary administrative support and swift handling of the purchase.

I thank my parents for nurturing my curiosity and supporting my academic pursuits.

Last but not least, I deeply appreciate my wife for her unwavering support and encouragement. Her belief in me and her presence during key moments have been the cornerstone of my journey.

Abstract

Single cavitation bubbles were used to investigate the effect of cavitation collapses onto a solid surface in a spatially and temporally controlled way. The focus of this work was on damage to Cu- and Fe-base alloys, as well as pure aluminum to make the connection to existing research. The single bubbles were induced by a focused laser pulse in distilled water. The expansion and the collapse of the bubbles in the vicinity of solid samples were recorded with up to two high-speed cameras using shadowgraphy. Also, a microscope observed damage on the solid surface *in situ*. This method provides insights into both small surface changes caused by the collapse of one single bubble as well as the cumulative damage caused by up to hundred-thousands of single-bubbles.

Damage from many single bubbles formed patterns that showed to be mainly dependent on the stand-off distance γ (the ratio of the distance from the bubble center to the surface and the maximum bubble radius). Somewhat surprisingly, even on the hardest material tested the first collapsing bubble could induce damage in the form of pits. The number of pits caused by one bubble varied stochastically from bubble to bubble. Across all materials, some bubbles caused no damage, while the maximum number of pits caused by one bubble decreased as the hardness of the tested material increased. As a parameter for the rate of early damage formation – the pitting – rate was defined as the slope of a linear fit to the number of pits per bubble. The pitting rate was dependent on both the stand-off distance and the bubble radius. The latter relation indicated a non-zero limit of the bubble radius that can cause pitting.

For γ ranging from 0.3 to 2, a correlation between pitting and the presence of stronger, non-axisymmetric regions during bubble collapse (for most γ values predominantly observed during the second collapse) was identified. These non-axisymmetric regions were the part of the bubble that collapses last, and thus were found to be associated with non-simultaneous nature of the collapse. For $\gamma > 2$, no damage could be observed even for many single-bubble collapses. For $\gamma = 1.4$ the stronger collapse regions were also the regions where a strong shock wave was emitted during the second collapse.

Kurzfassung

Einzel-Kavitationsblasen wurden verwendet um die Auswirkungen von Kavitation auf eine feste Oberfläche räumlich und zeitlich kontrolliert zu untersuchen. Der Schwerpunkt dieser Arbeit liegt auf der Schädigung von Cu- und Fe-Basislegierungen, aber es wurden auch Experimente an reinem Aluminium durchgeführt, um die Verbindung zu bestehender Forschung herzustellen. Die einzelnen Blasen wurden durch einen fokussierten Laserpuls induziert und ihre Dynamik wurde mit bis zu zwei Hochgeschwindigkeitskameras unter Aufnahme des Schattenwurfes beobachtet. Serien von Einzelblasen wurden nahe der Probe in destilliertem Wasser induziert. Mit einem Mikroskop wurden ihre Auswirkungen auf die Oberfläche zwischen den einzelnen Blasen *in situ* beobachtet.

Diese Methode ermöglicht sowohl Einblicke in kleine Oberflächenveränderungen, die durch das Kollabieren einer einzelnen Blase verursacht werden, als auch in kumulative Schäden, die durch das Kollabieren von mehr als hunderttausend einzelnen Blasen verursacht werden.

Die von vielen einzelnen Blasen verursachten Schäden bildeten Muster, die hauptsächlich von der *stand-off distance* γ (dem Verhältnis zwischen dem Abstand von Blasenmittelpunkt und der Oberfläche zu dem maximalen Blasenradius) abhingen. Es wurde festgestellt, dass selbst bei dem härtesten getesteten Material (Nickel-Aluminium-Bronze) durch die erste kollabierende Blase Schäden in Form von Pits (Eindrückungen im Material durch plastische Verformung) verursacht werden können. Die Anzahl der von einer Blase verursachten Pits schwankte stochastisch von Blase zu Blase. Bei allen Materialien verursachten einige Blasen keine Schäden, während die maximale Anzahl der von einer Blase verursachten Pits mit zunehmender Härte des geprüften Materials abnahm.

Als Parameter für die Rate der frühen Schadensbildung wurde die *pitting rate* als Steigung eines linearen *fits* an die Anzahl der Einzelschädigungen pro Blase definiert. Es wurde festgestellt, dass die *pitting rate* sowohl von γ als auch vom Blasenradius abhängt. Letzterer Zusammenhang deutet auf eine von Null abweichende Grenze für den Blasenradius hin, bei dem noch Pits verursacht werden.

Der Vergleich der Blasendynamik mit einzelnen Pits zeigte für γ zwischen 0.3 und 2 eine Korrelation zwischen dem Auftreten von Pits und stärkeren, nicht achsensymmetrischen Regionen (SCAs) des Blasenkollapses (dem zweiten Kollaps für die meisten γ). Es wurde festgestellt, dass diese Bereiche der Teil der Blase sind, der zuletzt kollabiert, und daher mit der Nicht-Gleichzeitigkeit des Kollapses zusammenhängen. Für $\gamma > 2$ konnten keine Schäden mehr aufgrund von Kavitationsblasen beobachtet werden. Für $\gamma = 1.4$ waren die SCAs auch die Regionen, in denen während des zweiten Kollapses eine starke Stoßwelle emittiert wurde.

List of Symbols

Symbol	Meaning	Unit
α	Maximum angular aperture	
a_1	Distance on the sample	m
a_2	Length of distance a_1 imaged on the sensor	m
d	Resolution	m
D	Distance of the bubble center from the solid boundary	m
ρ	Density	g/m³
E	Energy	J
ε	Strain	
f	Focal length	m
f_{lens}	Focal length of the lens	m
$f_{objective}$	Focal length of the objective lens	m
f_{tube}	Focal length of the tube lens	m
g	Gravitational constant	m³/s²·kg
h	Planck's constant	J·s
HV	Vickers hardness	N/m²
i	Distance of the image from the lens	m
m	Magnification	
n	Refractive index	
ν	Frequency of electromagnetic radiation	1/s
o	Distance of the object from the lens	m
p	Pressure	N/m²
p_B	Pressure within the bubble	N/m²
p_∞	Pressure far from the bubble	N/m²

v	Velocity	m/s
ν_L	Kinematic viscosity of the liquid	m²/s
R	Radius of the bubble (theoretical description)	m
r, r_{max}	Maximum radius of the bubble (in the experiment)	m
S	Surface tension	N/m²
σ	Stress	N/m²
σ_0	Yield strength	N/m²
σ_B	Ultimate strength	N/m²
σ_L	Fracture stress	N/m²
t	Time	s
θ	Incident angle of light ray	
z	Height	m

List of Abbreviations

Abbreviation	Description
316L	Low carbon 316 stainless steel
AI	Artificial intelligence
Al	Aluminum
ASTM	American Society for Testing and Materials
CFD	Computational fluid dynamics
NAB	Nickel-aluminum bronze
Nd:YAG	Neodymium-doped yttrium aluminum garnet
SCA	Strong collapse area
SEM	Scanning electron microscopy
CNN	Convolutional neural network
LED	Light-emitting diode
TEM modes	Transverse electromagnetic modes

Table of Contents

1. Introduction

Cavitation - the formation of vapor in liquids due to a local drop in static pressure below the liquid's vapor pressure - can cause severe damage if these vapor structures collapse repeatedly near a solid surface [1, 2]. Even materials with high cavitation-erosion resistance can be damaged this way [3]. Experiments investigating damage on technical alloys (either directly in the application [4, 5] or, for example, in acoustic cavitation experiments [6, 7]) typically involve a large number of bubbles at a time. On the one hand, this makes it difficult to relate a specific part of the damage to a single collapsing bubble, and on the other hand, multi-bubble phenomena can influence the experiment in an uncontrolled way.

Single cavitation bubbles are a common method to study the phenomenon of cavitation in spatially and temporally well controlled experiments [8, 9]. However, so far these experiments have mostly been performed on rather soft materials such as aluminum [10–12]. A soft material shows quite visible damage after only a few cavitation collapses, which makes it easier to evaluate these experiments even *ex situ*. It is not clear whether, and if so how, the findings from these experiments with soft materials can be transferred to technical alloys.

This work attempts to bridge the gap that exists between microscopically uncontrolled damage to technical alloys, by e.g., acoustic cavitation, and precisely reproducible loadings on soft materials by single bubbles. To do this, we developed an optical arrangement that allows for observing single bubbles and the surface being damaged at the same time. Close to a sample immersed in water, a series of single bubbles is induced by focused laser pulses and their effects are observed *in situ* with a microscope. Experiments with series of laser-induced single bubbles were carried out on Al-, Cu- and Fe-base alloys. This method not only provides insight into the progression of cavitation damage in technical alloys but can also be used to evaluate cavitation erosion resistance from the rate of single-bubble damage accumulation.

The bubble dynamics were recorded by up to two high-speed cameras and were correlated with the damage from a single cavitation bubble. The resulting pits were analyzed, and the different alloys were compared in their pitting behavior.

This thesis is “pseudo-cumulative” in the sense that its central 3 chapters (Chapter 4 - 6) are essentially each an unmodified peer-reviewed journal article published between 2021 and 2024. The author’s contributions to each article are declared in Section 9.1. The thesis begins with an introduction which is condensed from the introductions of the three papers. This is followed by the theoretical background, including information needed to understand this work (Chapter 2), and a literature review on single bubbles near solid boundaries to provide the scientific context of this work (Chapter 3). The first paper (Chapter 4) introduces the experimental setup and validates the microscope used for *in-situ* imaging. Early damage was observed on technical alloys and pits were counted after each bubble collapse. In the second paper (Chapter 5) the setup was used to correlate bubble dynamics with damage for specific experimental parameters. In the last paper (Chapter 6) we extended the range of parameters for the investigations of the first two papers. The conclusion (Chapter 7) is again condensed form the conclusions of all three papers and followed by an outlook on future work (Chapter 8) and additional results in the appendix.

The research underlying this thesis was performed in the DFG project “Optical in-situ analysis of the cavitation damage on technical alloys under repeated single bubbles” (Project number 451715773) jointly with Prof. Dr. Stefanie Hanke’s group. There, Christina Lopez de Arcaute y Lozano analyzed the metal samples with ex-situ microscopy methods. Some of her key results are included in this thesis where they complement the understanding gained by the in-situ imaging that is the focus of this work.

2. Physical Background

2.1 Cavitation

2.1.1 Introduction to Cavitation

Cavitation, i.e., phase change due to the ambient pressure falling below the liquid's saturation vapor pressure, is distinct from the transition to the gas phase by boiling which is caused by a rise of temperature [13]. Fig. 1 shows a schematic phase diagram of water. A given set of pressure and temperature is assigned one of three states of matter – solid, liquid and gaseous. The lines in the graph indicate a transition between these states [13]. The point where all lines intersect is called the triple point in which all three states are present. The end point of the gas-liquid intersection line is the critical point at which liquid and gas phase cannot be distinguished. The arrow where the line separating solid and liquid ends indicates that this line does not end at a critical point and both phases can still be distinguished. Cavitation can be represented with a vertical line between liquid and gas phase (isochoric) while boiling would be a horizontal line (isobaric) [13].

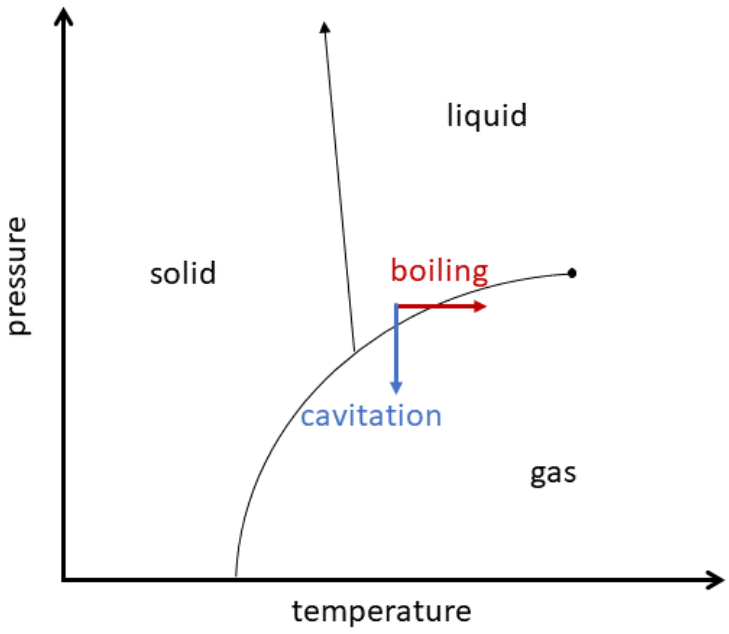

Fig. 1 Schematic phase diagram for water (adapted from [13]).

Often, a decrease in pressure and subsequent cavitation is caused by an increase in the liquid flow velocity v. In one-dimensional flow (e.g., along a streamline) this decrease can be described by Bernoulli´s equation of the energy of fluid parcel

$$\frac{v^2}{2} + gz + \frac{p}{\rho} = const. \quad (1)$$

with fluid velocity v, the acceleration due to gravity g, height z, the pressure at a chosen point of the fluid p and density of the fluid ρ [14]. Thus, an increase in the fluid velocity yields a decrease in the pressure as the density is constant.

The origin of cavitation bubbles in the increase in velocity of the fluid means that they are typically unstable and collapse when the velocity decreases and bubbles, therefore, reach areas of higher pressure. Fig. 2 shows cavitation occurring due an acceleration of the fluid near a rotating ship propeller. The cavitation occurring in this example is also limited to an area close to the blade of the propeller which means most bubbles collapse before leaving the vicinity of the blade. The collapse of these bubbles can then lead to cavitation damage and cavitation erosion, which is discussed in the next section.

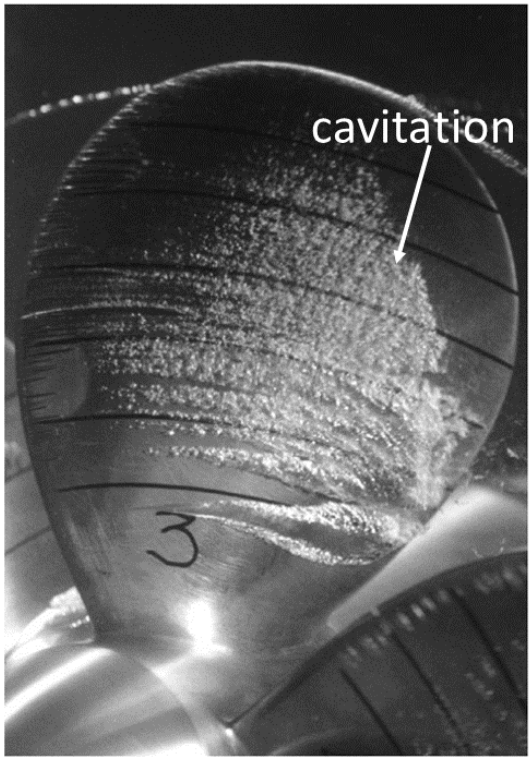

Fig. 2 Cavitation occurring near a ship propeller (adapted from [15]).

2.1.2 Cavitation Erosion

Cavitation erosion drew first attention over 100 years ago, observed on ship propellers [16]. Despite extensive research, there are still unsolved aspects, particularly regarding the details of the damage process due to cavitation. Understanding cavitation erosion is difficult because it involves both two-phase flow and solid mechanics.

Fig. 3 End stage of cavitation erosion of a ship propeller (adapted from [15]).

In addition to erosion of ship propellers, cavitation erosion can occur in applications such as nozzles, pumps, and turbomachinery [4, 5, 15, 17, 18]. Prevention of cavitation erosion is approached from different directions. In applications, there is a desire to first minimize the extent to which cavitation occurs in general as well as the distance from the solid surface near that it does [15]. Also, it is possible to select the material properties in such a way that there is a high resistance against cavitation erosion [19]. Cavitation resistance of technical alloys is typically tested according to the “American Society for Testing and Materials” (ASTM) standard G32 [3, 20, 21]. Fig. 4a shows a schematic of an experiment in which an oscillating sonotrode induces bubbles called acoustic cavitation. ASTM G32 looks at the material loss that occurs over a certain time period when the material is exposed to acoustic cavitation [21]. An example of data acquired in such experiments is shown in Fig. 4b.

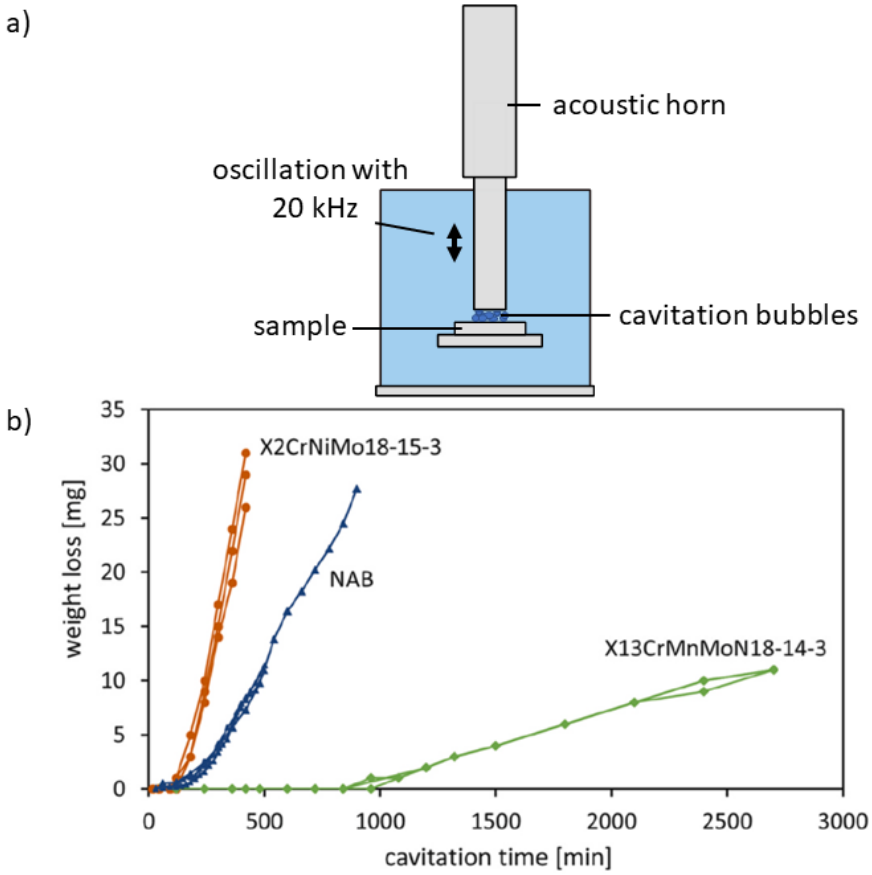

Fig. 4 a) Schematic of an acoustic cavitation experiment and b) data on weight loss over time under acoustic cavitation (adapted from [3]).

In both scenarios – whether in an application like a ship propeller or in laboratory experiments with acoustic cavitation – the correlation between the collapse of individual bubbles and the resulting material damage is often elusive due to the sheer multitude of simultaneous cavitation structures, as illustrated in Figure 2 [1, 22]. In contrast to that, single cavitation bubbles allow both spatially and temporally well controlled experiments. Section 3.3.2 discusses damage from single bubbles and the link to acoustic cavitation. However, a more fundamental description of free single bubbles is provided in the next section, and detailed descriptions of single-bubble experiments near a solid boundary are given in Section 3.1.

2.1.3 Free Single Bubbles

The model system of a collapsing single bubble is typically a spherical single bubble. Although bubbles may not be perfectly spherical in experiments or applications, assuming they are spherical simplifies calculations considerably and

aids in understanding single-bubble collapses. Fig. 5 gives an overview of the grow and collapse of a free spherical cavitation bubble that was induced with a focused laser pulse. The first image shows the plasma breakdown out of which the bubble forms. The maximum radius is reached at 84 µs. The bubble shows damped oscillation and does not dissolve after the first collapse (at 162 µs). These oscillations are typically referred to as the first, second, and third collapse, and so on.

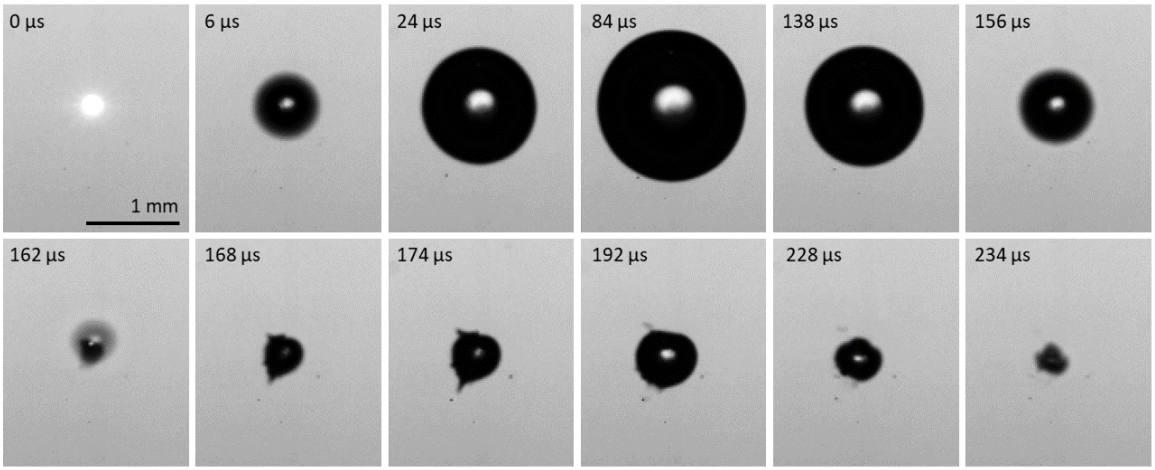

Fig. 5 Images from the grow and collapse of a free cavitation bubble that starts with the plasma breakdown. The first collapse takes place at 162 µs and the second at 234 µs.

The collapse of a free spherical cavitation bubble can be described by the Rayleigh-Plesset equation [23]

$$\frac{p_B(t)-p_\infty(t)}{\rho_L} = R\frac{d^2R}{dt^2} + \frac{2}{3}\left(\frac{dR}{dt}\right)^2 + \frac{4\nu_L}{R}\frac{dR}{dt} + \frac{2S}{\rho_L R} \qquad (2)$$

with the time-dependent radius of the spherical bubble R, the pressure in the liquid infinitely far from the bubble $p_\infty(t)$, the pressure within the bubble $p_B(t)$, the density of the liquid ρ_L, the kinematic viscosity of the liquid $\nu_L$and the surface tension S. The equation can be derived in different ways assuming incompressibility of the liquid, that the amount of gas contained in the bubble is constant, no heat transfer takes place and that the bubble is saturated with vapor, whose partial pressure is the vapor pressure at the temperature of the liquid [13, 24, 25].

This equation is no longer valid when the bubble collapses with radial interface velocities close to the speed of sound in the liquid, due to assumption of incompressibility of the liquid [25]. With this exception, the Rayleigh-Plesset equation can give valid predictions of the bubble radius and collapse time of the initial bubble collapse. As described above, however, a single bubble shows damped oscillation in size that cannot be represented by the Rayleigh-Plesset equation [26]. The details of the equations for a more correct description of free single bubbles are beyond the scope of this introduction; details are given in [25–27]. Fig. 6 shows the radius of a collapsing bubble versus the time from numerical and experimental investigations [26]. The bubble collapses several times dissipating some of its energy in each oscillation, which can be seen from the reduced maximum radius during the subsequent oscillation. At the minimum volume of the gas phase, the accelerated shrinking of the bubble causes a high-energy state (high pressure and temperature) that can only be relieved by the emission of a shock wave, at least during the first two collapses [28, 29]. How the dynamics of a free single bubble translates to a bubble collapse in the vicinity of a solid surface is described in detail in Chapter 3.

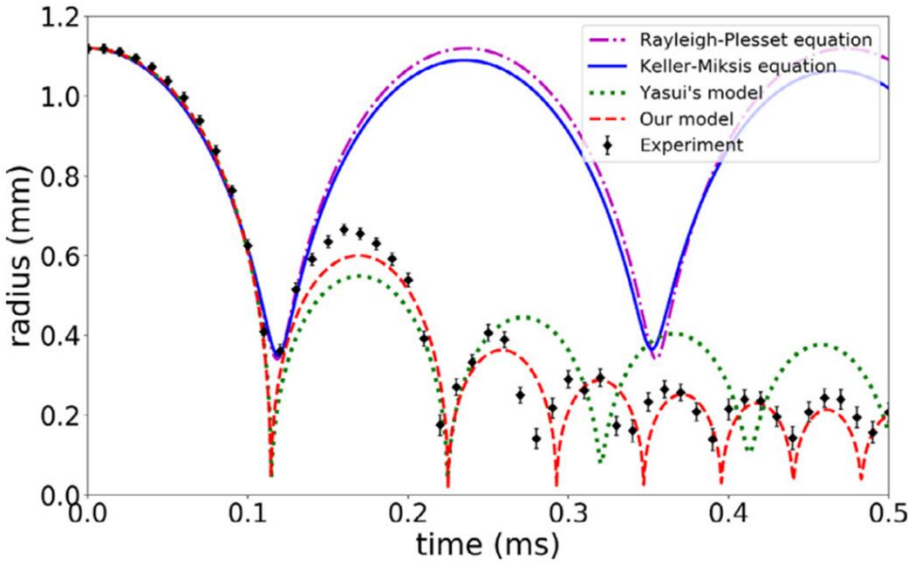

Fig. 6 Bubble radii from different models and experimental data from Zhong et al. (♦) [26]. Dash-dotted line are results given by the Rayleigh-Plesset equation [23]. The solid line represents results given by the Keller-Miksis equation [30], which takes liquid compressibility into account. Dotted line shows results given by the Yasui's model [27]. Dashed line are results given by Zhong et al. [26]. (Figure adapted from [26]).

2.2 Optics

The most complete description of light, a form of electromagnetic radiation, is quantum electromechanics. However, many optical phenomena can be understood by describing light in a “semi-classical” way as either a wave or a particle (photon) [31]. Here, the vacuum velocity of light is $c = 299\,792\,458\ \frac{m}{s}$ and a photon is carrying the energy

$$E = h\nu \tag{3}$$

with the Planck constant h and the frequency of the electromagnetic radiation ν.

When light waves travel through a medium their velocity v is reduced, described by the refractive index n of the medium. Due to this decrease of the velocity, at the interface between media with different refractive indices light is refracted as described by Snell´s law, illustrated in Fig. 7 [32].

$$\frac{n_2}{n_1} = \frac{v_1}{v_2} = \frac{\sin(\theta_1)}{\sin(\theta_2)} \tag{4}$$

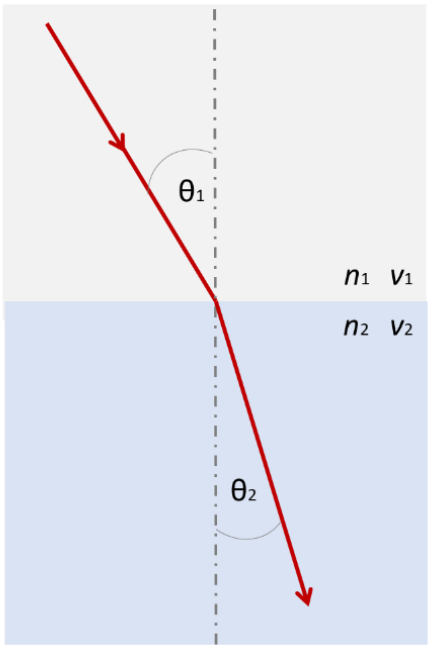

Fig. 7 Refraction of light at an interface of media with different refractive indices, with v_2 being lower than v_1 ($n_1 < n_2$).

For some purposes, an even simpler description is sufficient – geometric optics. Geometric optics describes light by rays that do not interact and are straight unless

refraction or reflection occur (like in Fig. 7) [32]. In particular, lenses and imaging can be well understood with this model. Often, the paraxial approximation is used with this model – a small-angle approximation where $\sin(\theta) \approx \theta$ is assumed [32]. Fig. 8 shows this approximation for a thin lens with focal length f_{lens} and how rays are refracted by it. In this example the lens is creating an image I of an object O. If the object is imaged correctly in the image plane the lens equation is fulfilled [32].

$$\frac{1}{f} = \frac{1}{o} + \frac{1}{i} \tag{5}$$

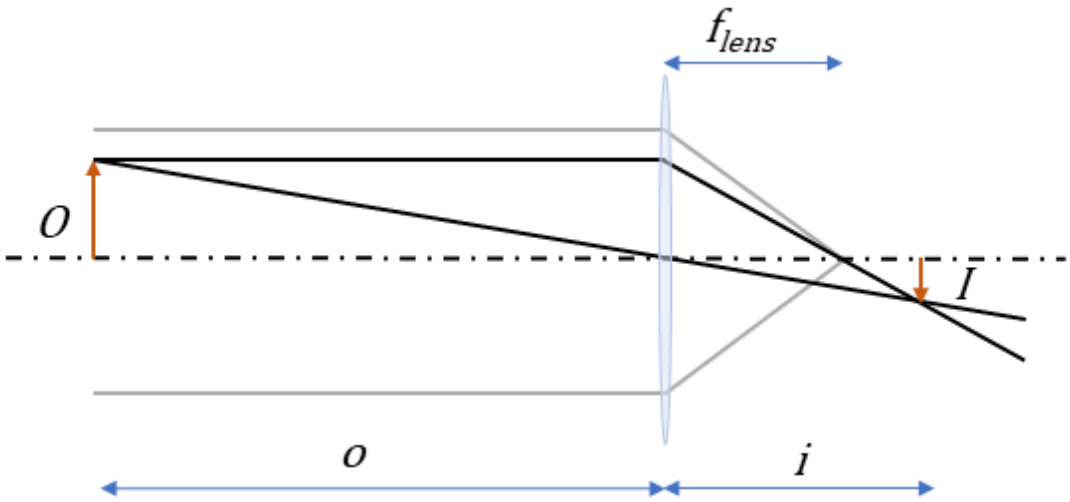

Fig. 8 Lens forming an image I of an object O fulfilling the thin lens equation.

Put simply, this is what happens in imaging systems such as camera lenses, microscope objectives, etc. However, modern imaging lenses are typically much more complex. The reason for this is that they are designed to minimize "aberrations", which can be understood as deviations from the first-order small-angle paraxial approximation for monochromatic light.

Aberrations occur due to various effects. Chromatic aberrations for example occur due to the dependence of the refractive index on the wavelength of light. Additionally, there are monochromatic aberrations (Seidel aberrations) that influence imaging quality in different ways [33]. Fig. 9 shows two lenses focusing a collimated beam of light. One focuses the light ideally and the other displays spherical aberration. Spherical aberration is caused when light is refracted by spherical interfaces. It is a shift of the focus of rays depending on at what distance from the optical axis they hit the lens. Spherical aberration is the only Seidel

aberration that appears on the optical axis and is therefore especially important for laser focusing. Other aberrations that appear off-axis are more important for wide-field imaging and are described in detail in [33].

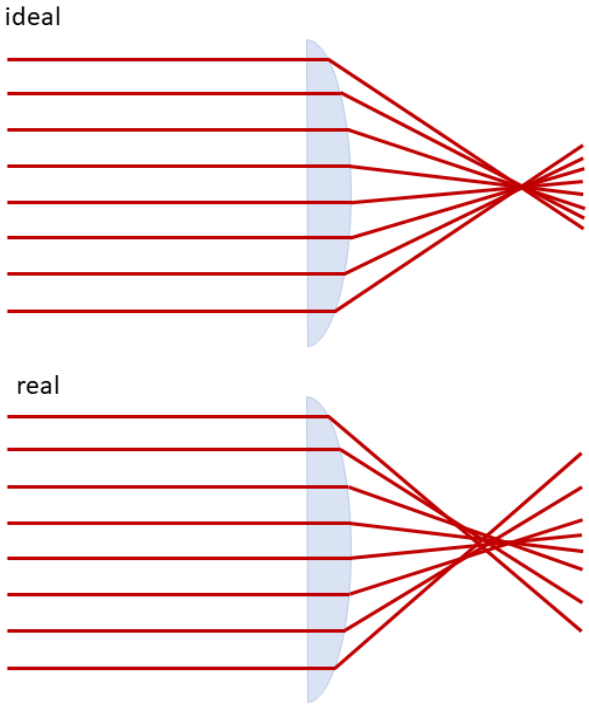

Fig. 9 Focus of two lenses one showing ideal focus and the other spherical aberration.

Apart from refraction and reflection, geometric optics neglects the interaction of light and matter. However, light and matter can interact in several ways – absorption, emission, reflection, transmission/refraction, and scattering are some possible interactions. Some of them are important for the laser-induced bubble-generation, the imaging of the bubble, and the caused damage. A more detailed explanation is provided by [31, 32].

2.2.1 Solid-state Laser

The term 'laser' is an acronym for 'light amplification by stimulated emission of radiation', which describes the process used to create monochromatic, coherent high-power light “beams”. Fig. 10a shows a typical arrangement of essential laser components. In solid-state lasers, an ion-doped glass or crystal is optically pumped by a flash lamp. The laser-active material is placed between mirrors where light oscillates during the amplification. The amplification is possible due to a specific state structure of the electrons in the optically active dopant, shown schematically

in Fig. 10b. The pumping process excites electrons from the ground state E_0 to the state E_P. This state quickly relaxes to the state E_L without emitting radiation. Sufficiently high pumping rates cause population inversion, in which there are more electrons in the state E_L than in the ground state E_0. By relaxation to E_M, this state emits the laser wavelength. However, due to the population inversion, the dominant relaxation mechanism is by stimulated emission which causes the amplification of coherent radiation during the oscillation of the light in the laser [34].

The laser used in this work is a pulsed Nd:YAG laser in which the laser medium is an yttrium aluminum garnet (YAG) crystal doped with neodymium (Nd). The Q-switch is an optical element that abruptly opens or closes laser activity. It is closed until the maximum population inversion is reached by the optical pumping, then opens to allow sudden emission of a high-power pulse that releases the accumulated pump energy. The emission wavelength of this laser is 1064 nm.

In a laser cavity, light can oscillate in different resonant modes. Most relevant here are the transverse electromagnetic (TEM) modes. In which modes the light oscillates depends in particular on the geometry (distance and type of mirrors) of the resonator as well as the fine adjustment of the laser, but is also influenced by the laser temperature, for example [34]. The spatial combination of the TEM modes generates the transverse “beam profile” of the laser. Fig. 10c shows modes that can occur in a laser with round mirrors. The lowest order mode is Gaussian, while higher order modes are more complex. In particular, their diameter also increases, and the beam intensity is unevenly distributed. The beam profile can be a combination of multiple modes and in pulsed lasers, the beam profile can fluctuate from pulse to pulse, which must be taken into account in experiments.

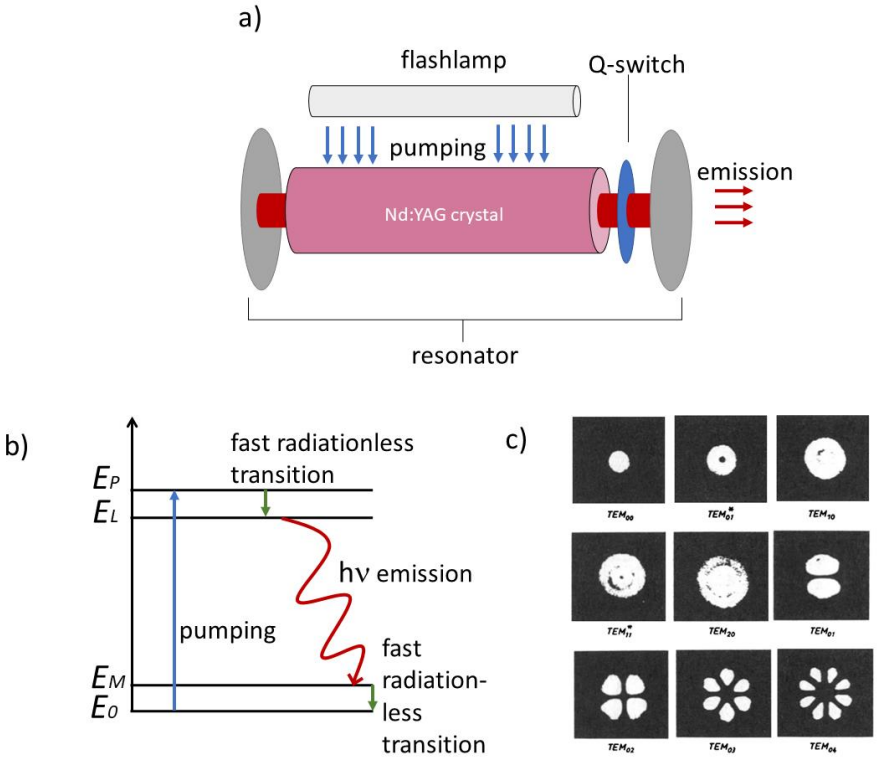

Fig. 10 a) Arrangement of laser components b) Schematic of states of a four-level laser c) TEM modes of a laser with round mirrors (adapted form [34]).

2.2.2 Light Emitting Diodes (LED)

Light Emitting Diodes (LED) are semiconductor devices that emit light when a current is passed through them. In a LED, a p-n junction is a boundary between two doped semiconductors. While the "p" side contains an excess of “positive” electron holes, the "n" side contains more (negative) electrons. When a voltage is applied across the junction, electrons recombine with holes. The energy released is then emitted in the form of light.

LEDs have several advantages over other light sources. First, they can be quickly and easily controlled by switching the current. In particular, high-power LEDs can achieve very short pulse durations and high repetition rates that are only surpassed by lasers, which are much more expensive and produce coherent light. Second, there is now a wide variety of LEDs with different spectral properties to choose from. Changing the LED to change the wavelength of illumination in an experiment is often very easy.

2.2.3 Microscopy and Köhler Illumination

A microscope is a tool for visualizing objects at magnified scales. Magnifications from 2x to many thousand times are possible, depending on the type of microscope. Most of the microscope images shown in this work are light microscope images at magnifications from 3x to 10x.

In addition to the magnification, the resolution d that can be achieved with a microscope is an important parameter. The resolution may be defined as the minimum distance between two lines at which they can still be distinguished. While advanced microscopy methods achieve even higher resolutions, the theoretical resolution of a light microscope is given by

$$d = \frac{\lambda}{\mathrm{n}\,\sin(\alpha)} = \frac{\lambda}{2\,\mathrm{NA}} \tag{6}$$

with the wavelength of the light λ, the maximum angular aperture α, numerical aperture NA and the refractive index of the imaging medium n.

Given that the design of a custom light microscope was an essential part of the work, the general arrangement of the optical elements is briefly explained. Part of the microscope is also the illumination which has to fulfill requirements such as a very small illuminated field and a high numerical aperture (matching the collection optics). To achieve this, a configuration called Köhler illumination was chosen.

Fig. 11 shows a schematic view of the beam path of light in a microscope including the Köhler illumination (dotted lines). It consists of a collimation and an auxiliary lens. The general idea is that the image of the light source is not visible in neither the sample nor consequently on the sensor, while a strong and homogeneous illumination with large numerical aperture of the sample is enabled at the same time. The light source is imaged on the illumination aperture, which is in the back focal plane of the objective lens. Therefore, the light source is completely defocused at the sample [35].

From the sample, light rays emitted from two exemplary points are shown that go first through the objective lens. The objective lens is “infinity corrected”, meaning light from the focus plain exits the objective lens in parallel beams. This is standard for state-of-the-art objective lenses and useful when the light is transmitted through elements like filters or beam splitters in this “infinity space”. Finally, the tube lens

focuses the light on the sensor. The magnification of the system is $m = \frac{a_2}{a_1}$. It the ratio of the focal length of the objective lens and the tube lens, $m = f_{tube}/f_{objetiv}$ [36].

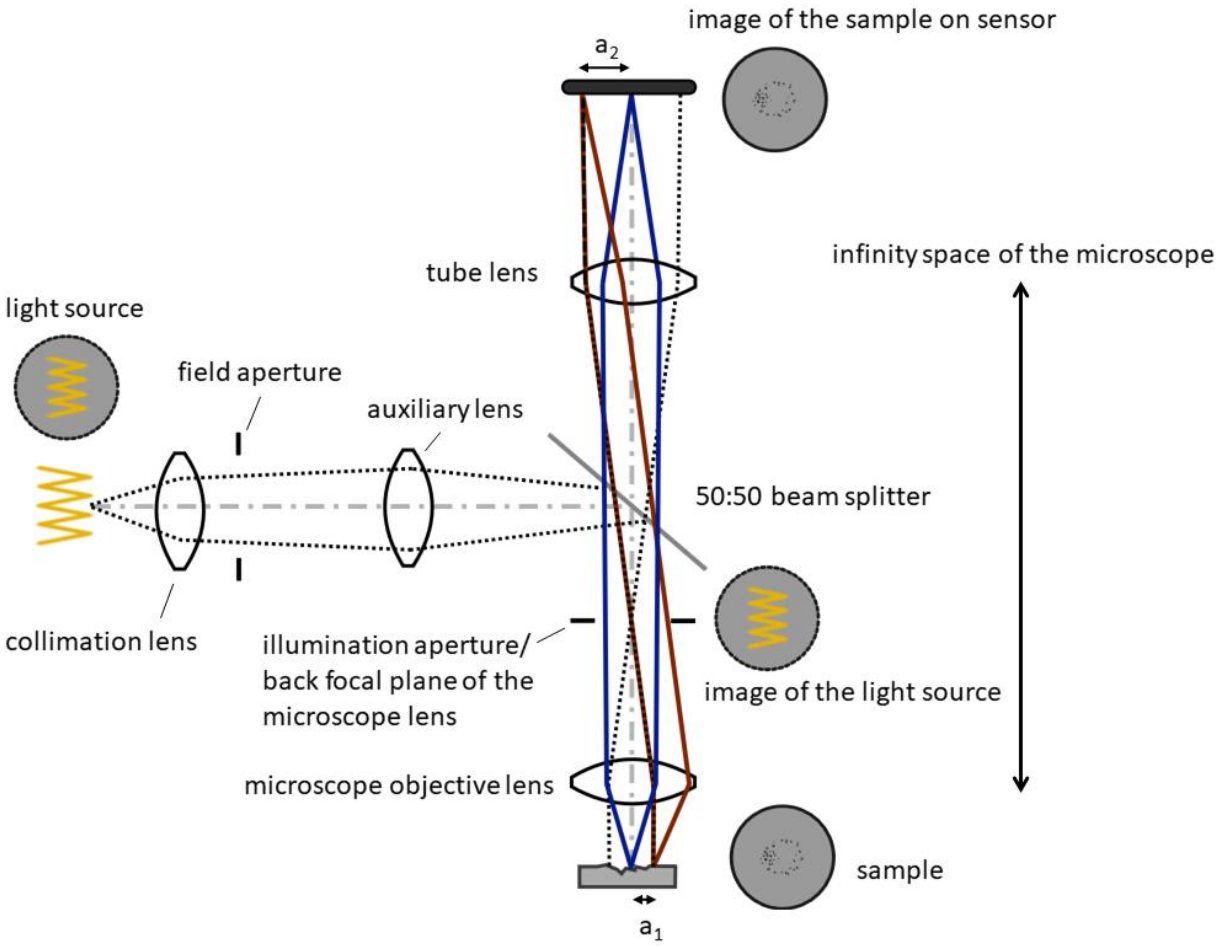

Fig. 11 Schematic beam path in an incident-light microscope. The circles indicate where the light source and the sample are imaged in the microscope.

2.3 Materials

This work focuses on the investigation of technical alloys that are used in applications. All materials used in this work are ductile metals but with different hardness and microstructure. This section gives a short introduction to material properties as well as to the testing procedure of characteristic quantities used to describe the properties of materials.

2.3.1 Metals

Atoms that form structures such as molecules or crystals do so, because these states are energetically favorable. This energy difference between a structure and the single atoms is typically due to a different electron configuration. Fig. 12a shows a simple model of a positive nucleus that is surrounded by electrons on atomic shells. In general, it is energetically favorable that all occupied shells are entirely filled. The way in which the electron configuration changes depends a lot on which atoms are bonded. Metals have one, two or a maximum of three electrons in their outer shells which are called valence electrons. When metals bond, these electrons are no longer bound to specific atoms. The electrons of the atom that were no valence electrons form together with the core positively charged ions. These ions form a structure like the one in Fig. 12b with the free electrons act as a glue to hold them together [37].

Again, it is an energetically superior configuration when the structures shown in Fig. 12b occur repeatedly in larger formations. Fig. 12c shows such a formation that is called a crystal. Materials in which only one crystal exists, meaning all atoms go along with the configuration in Fig. 12b (excluding minor defects in the material), are called single crystals. A formation of atoms that is a basis of the larger crystal structure is called a unit cell. However, crystals can spread out in different directions in a material. Fig. 12d shows a schematic of the structure of a material with multiple crystals. The individual crystals are called grains; interfaces between them are called grain boundaries, which are two-dimensional defects in the structure [37]. Their occurrence and size can affect the material properties discussed in the next section [38, 39].

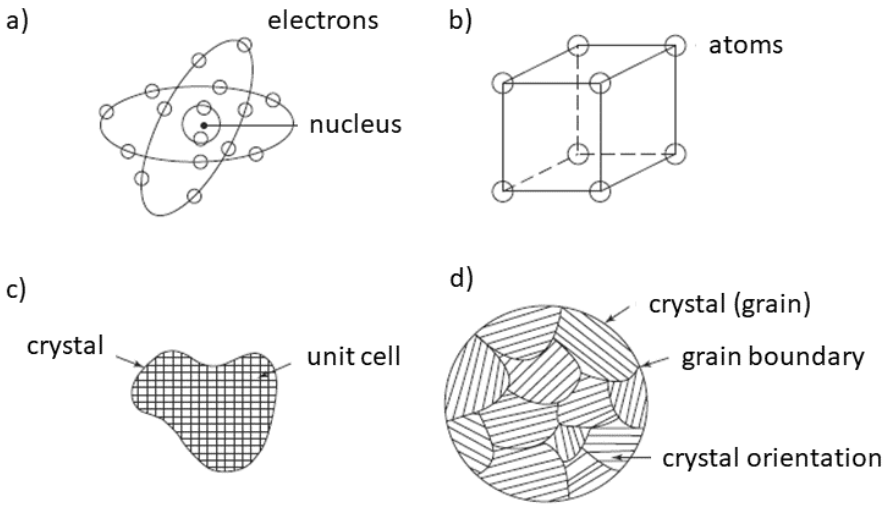

Fig. 12 Structure of metals from a) atoms over b) a unit cells to c) crystal and d) multiple grains (adapted from [37]).

Alloys, which are our sample materials, contain more than one chemical element. These elements are added to a base metal and can significantly change the material properties [37]. The combination of elements can occur in different proportions and thus in different atomic configurations. A particular configuration is called a phase. The mixture of elements can occur in a single phase as shown in Fig. 12d. However, depending on the concentration of the elements and the temperature during mixing or subsequent heat treatment, more than one phase may occur [40]. This means that the concentration and orientation of atoms in unit cells can vary throughout the material. Apart from the fact that different phases are likely to have different material properties, this means that phase boundaries are present in the material as well as different microstructures which are, again, important for material properties [37]. Fig. 13 shows an example of how the same elements can form two materials with very different microstructure depending on the phase in which the combined atoms occur.

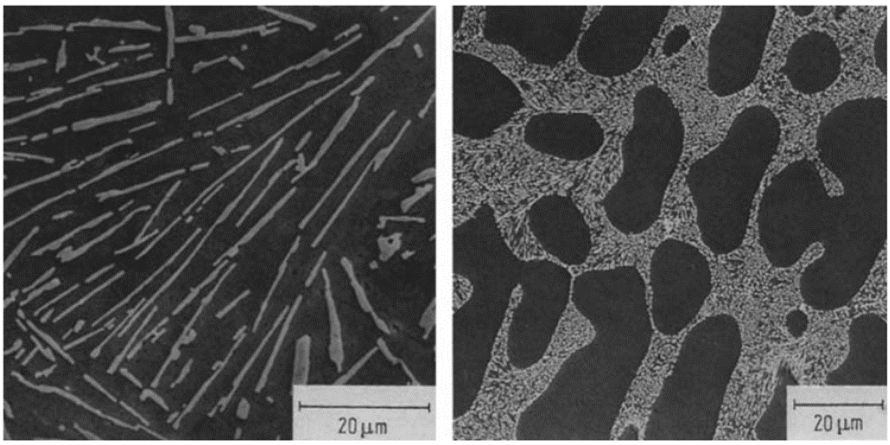

Fig. 13 Electron microscopy images of an Al-Si alloy with different microstructure [40].

2.3.2 Mechanical Properties and Material Testing

Mechanical properties are typically characterized with values like hardness, strength, and ductility. These are the reference values for material development and often used to describe material behavior due to a specific load. The tests of these values are standardized in some way and typically macroscopic in comparison to e.g., microstructure. This section serves as a short overview to give the reader an impression of how materials are commonly tested.

Many material-property analyses are based on the tension test [37, 40]. In this relatively easy-to-perform test, a sample of a given diameter is pulled apart and the deformation of the material is analyzed. The shape of the specimen, the temperature, and the strain rate, among other things, affect these tests [37]. Fig. 14 shows the tension curve of a ductile material. Definitions of strain and stress are given in the figure. The curve shows a linear relationship between strain and stress at low strain. Here, the material deforms elastically. If the strain rises further, plastic deformation occurs. From the point of ultimate strength, both strain and stress decrease due to the flow of the material until the fracture of the sample takes place [40].

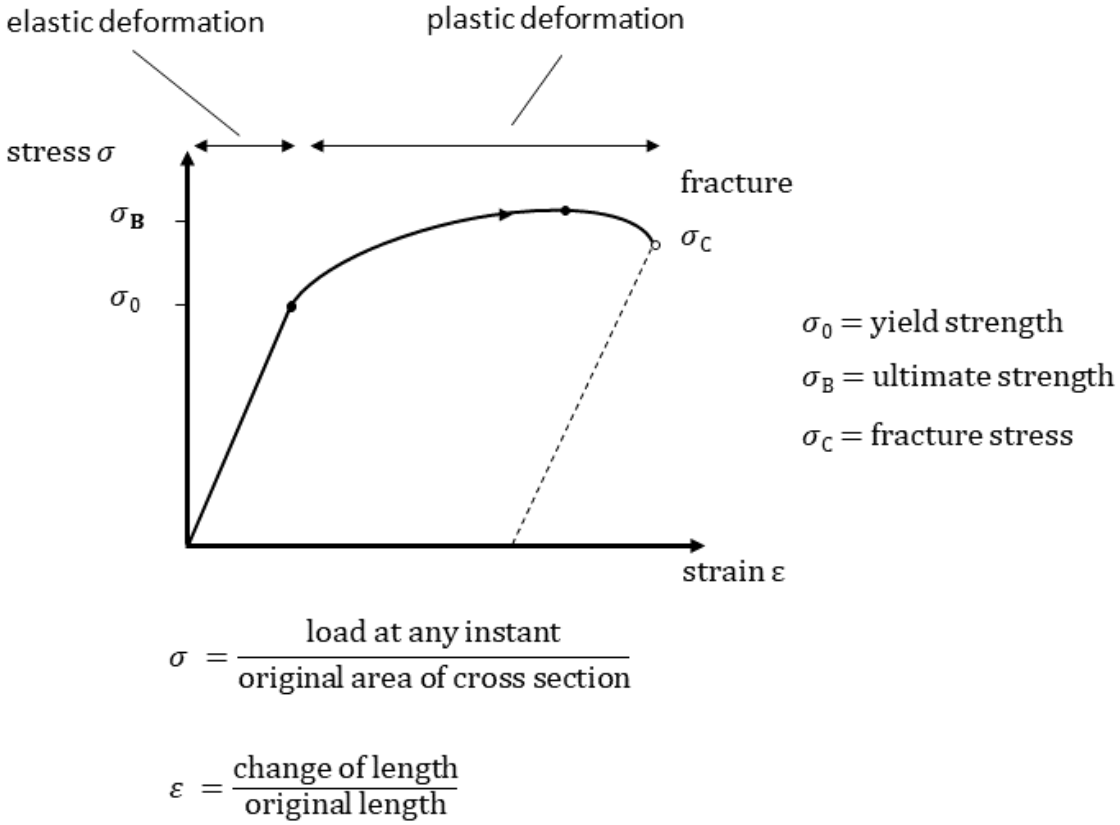

Fig. 14 Tension curve of a ductile material (adapted from [37]).

Another important material property is hardness. Hardness is a measure of a material's resistance to local plastic deformation. The test of this property is often done by a small dent or a scratch [37]. The test method referred to in this work is the measurement of Vicker's hardness. In this test, a pyramidal-shaped diamond indenter is pressed onto the surface at a given load. The hardness HV is given by the load divided by the surface area of indentation [37]. However, both the standard tension test and the test of the hardness are performed at slow strain rates compared to the strain rates that are most likely to occur due to a cavitation collapse. It is not clear to what extent they are only an inaccurate characterization for very fast strain rates [41].

3. Literature Review: Single-Bubble Cavitation Near Solid Boundaries

3.1 Experiments

Two ways to generate single bubbles in a spatio-temporally precise and reproducible way are focused laser pulses [8, 28, 29, 42–44] and high-voltage discharges between electrodes [45–47]. In the latter method, however, it is likely that the electrodes influence the bubble dynamics. For this reason, in the presented work, bubbles were generated with a focused laser pulse. The focused light causes a plasma breakdown in the liquid from which a bubble of water vapor and other gases is formed [48, 49].

Many studies investigated the fluid dynamics of collapsing bubbles [28, 42, 50–53]. Other works studied the effect of such individual bubbles on a nearby solid surfaces [9–12, 44, 54, 55]. The experiments investigating effects on the surface are discussed in detail in Section 3.3. When the collapse of a single bubble occurs close to the solid boundary, the dynamics of the bubble dramatically deviate from the spherical oscillation described in Section 2.1.3. The overall shape of the collapse that occurs depends mainly on the stand-off distance γ, which is defined as the distance D of the bubble center from the solid boundary divided by maximum bubble radius r_{max} (Fig. 15).

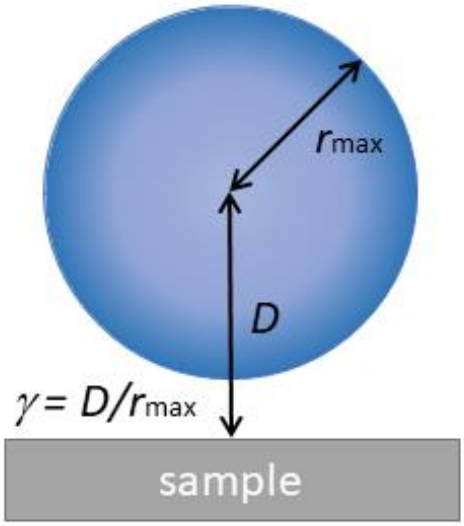

Fig. 15 Stand-off distance γ.

Fig. 16 shows three examples of bubble collapses at different stand-off distances. As the bubble shrinks, it is attracted to the solid surface. The reason for this is the pressure in the surrounding liquid during the shrinking process and can be descripted by the Kelvin Impulse [56, 57]. A liquid jet pierces the bubble in the direction of the solid surface, leaving the bubble in a toroidal shape, which then collapses again [52, 58]. Some of these phenomena are marked in Fig. 16. In addition to the change in shape of the bubble over the collapse process, an important difference between different γ is also location in relation to the solid surface when the first and the second collapse take place. For example, depending on γ, the first collapse may occur only a few µm from the sample to over 1 cm away from the surface. A detailed study on thickness of the liquid layer between the sample and the bubble during the first collapse was conducted by Reuter and Kaiser [59]. This is particularly important, due to a shock wave which is emitted during the plasma breakthrough, as well as during the first and second collapse [11, 28, 49] – however, the shock wave is not visualized in the recordings of Fig. 16. More examples of bubble collapses from additional angles and at different γ are shown when relevant in following sections and can also be found in [11].

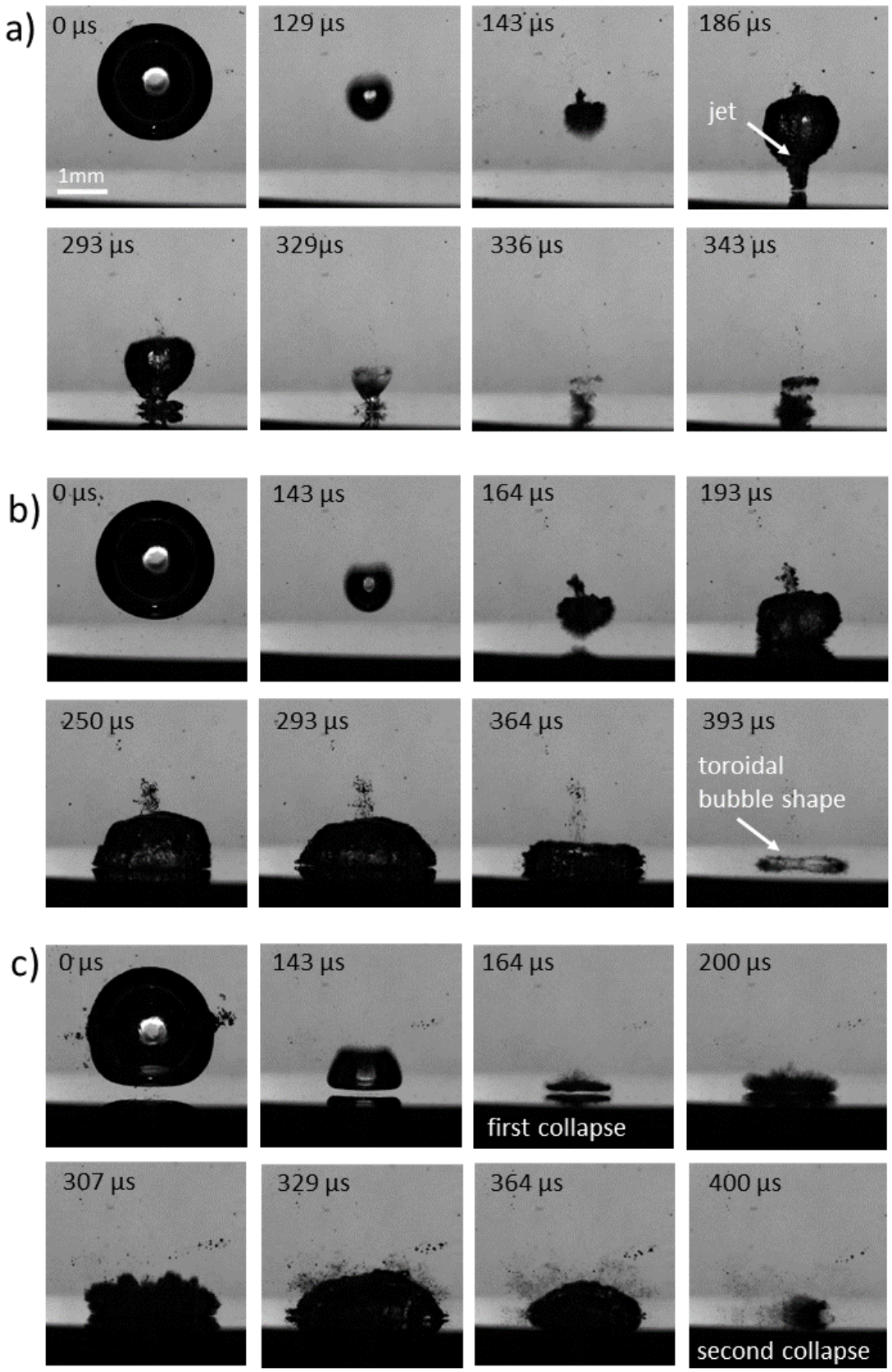

Fig. 16 Cavitation bubble collapse seen from the side at a) $\gamma = 1.8$, b) $\gamma = 1.4$, c) $\gamma = 0.96$ (adapted from [60]).

3.2 Simulations

Simulations are an important tool for understanding cavitation. They can give access to information that is not or only very difficult to access in experiments like gas mixture [61] or temperature [62]. Especially in complex applications where experiments can only hardly be conducted simulations help understanding the formation of cavitation [63] and damage due to its collapse [64]. Typically, these simulations are based on CFD (Computational Fluid Dynamics) methods and often use a underlaying simplified model (e.g., for bubble dynamics). However, despite the importance of such simulations, since this work is about single bubbles, the focus of this chapter is also on the simulation of single bubbles.

As in the examples given in Section 2.1.3 the problem of a bubble in the vicinity of a solid surface is often solved in two-dimensional simulations. Early work on this was done by Plesset and Chapman 1971 predicting the liquid jet during the collapse [65] and by Mitchell and Hammitt 1973 [66]. While early work like this mostly focused on the bubble wall velocity, current studies are capable of giving much more detailed information about the fluid due to the immense increase of computing power over the last decades. For example, current work gives information about shock wave emission [67, 68] and detailed information on pressure fields [69, 70]. Fig. 17 shows two examples of images of simulated bubble collapses. The left side of Fig. 17a shows a “schlieren image” which is computed from the normalized density of fluid in the simulation. The color on the right of shows the normalized fluid velocity. In Fig. 17b, the color shows pressure in bar and the flow is implied with grey arrows. Both of these examples show high-resolution details of bubble collapse and shock wave emission that are difficult to visualize and to identify in the experiment. In general, the collapse of bubbles in simulations fits well with what can be found in experiments (e.g. [71, 72]).

Even though considerable progress has been made in recent years in the field of single-bubble simulation, three-dimensional simulations are quite rare, especially when it comes to bubbles near boundaries. A three-dimensional simulation of Sagar and el Moctar [72] shows a non-axisymmetric collapse of a spherical bubble.

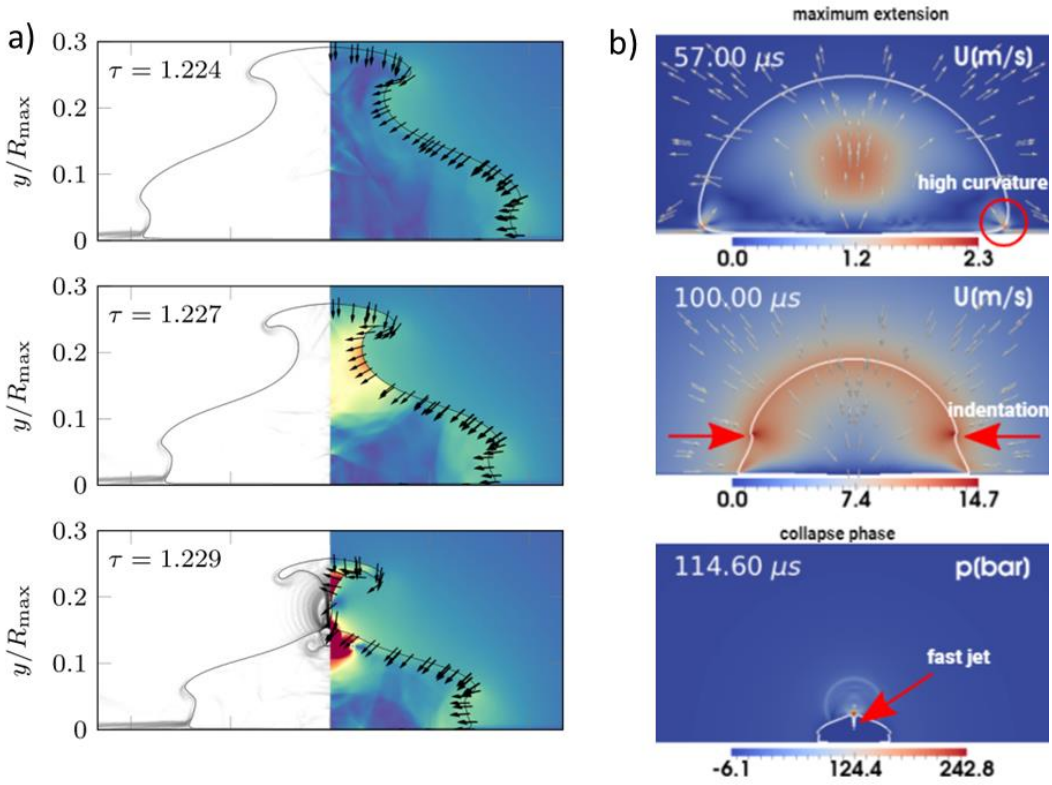

Fig. 17 Selected pictures from current single-bubble simulations near boundaries at different stages of the bubble collapse a) The right side of the image showing scaled numerical schlieren image and the right side the normalized velocity amplitude (adapted from [68]) b) Images show details of the flow (grey arrows) and color gives the pressure in bar (adapted from [70]).

3.3 Cavitation Damage

Even if cavitation can also be *useful*, e.g., in the medical context [73, 74], particle synthesis [75], and surface cleaning [76, 77], this work mainly focuses on the investigation of what is understood here as material *damage*. There is some previous work on cavitation damage due to single bubbles. However, most of that work focused on soft materials where either one single bubble collapse or low numbers of bubbles (typically under 100 bubbles) were investigated [10–12]. Soft materials have the advantage that they show surface damage that is easy to detect after just a few bubbles.

3.3.1 Damage Patterns

Fig. 18 shows the surface damage caused by 100 cavitation bubbles on pure aluminum at different γ from the seminal work of Philipp and Lauterborn [11]. It can be seen that a variation of γ causes quite different damage patterns. The upper

boundary above which no damage was induced was found to be around $\gamma = 2$. For all $\gamma < 2$, Fig. 18 shows some form of surface damage. The damage formed mainly out of smaller indentations – from here called pits – which are defined more in detail in Chapter 4. Only for $\gamma = 0.69$ and $\gamma = 0.31$ damage is seen that is most likely a larger-scale plastic deformation that is not correlated with the occurrence of pits. Unfortunately, no quantitative images of the overall damage were taken as a part of this work. Philipp and Lauterborn found that the area where damage formed on aluminum is spatially correlated with the region where the bubble collapses the second time [11].

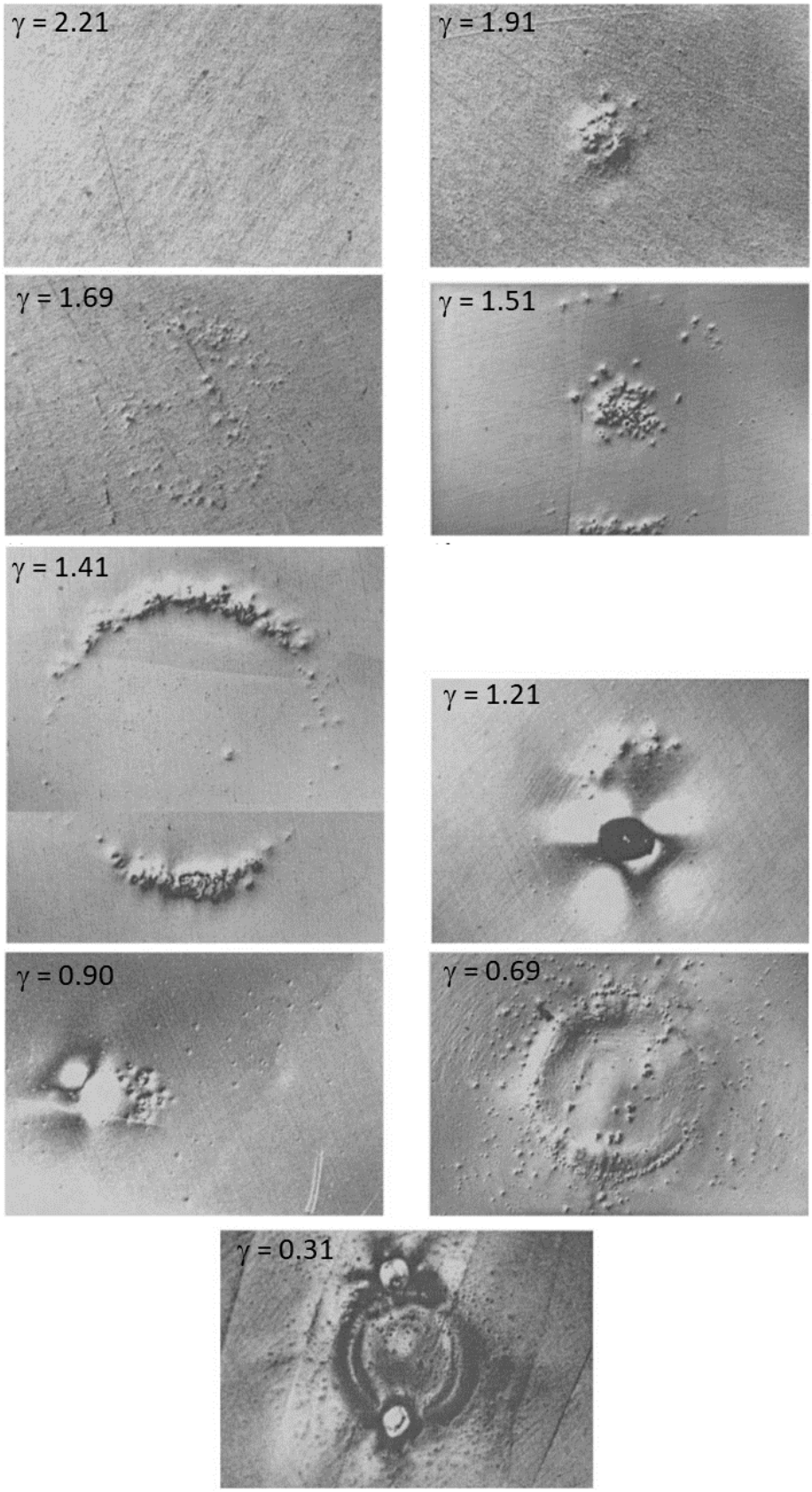

Fig. 18 Cavitation damage of 100 bubbles on aluminum at r = 1.45 mm. The direction of the laser beam is from below to the top of the images (adapted from [11]).

Beyond the work on aluminum, the work from Philipp and Lauterborn is one of the few that at least partially looked into the cause of damage on technical alloys. Fig. 19 shows cavitation damage from 5000 single bubbles on brass. A ring shape damage pattern forms with an area of more damage towards the direction of incoming laser light. Again, many smaller pits form this larger shape. The stand-off distance of γ = 1.29 is between the ones on aluminum that are shown in Fig. 18. However, the damage pattern is a reasonable transition between the damage found at γ = 1.21 and γ = 1.41.

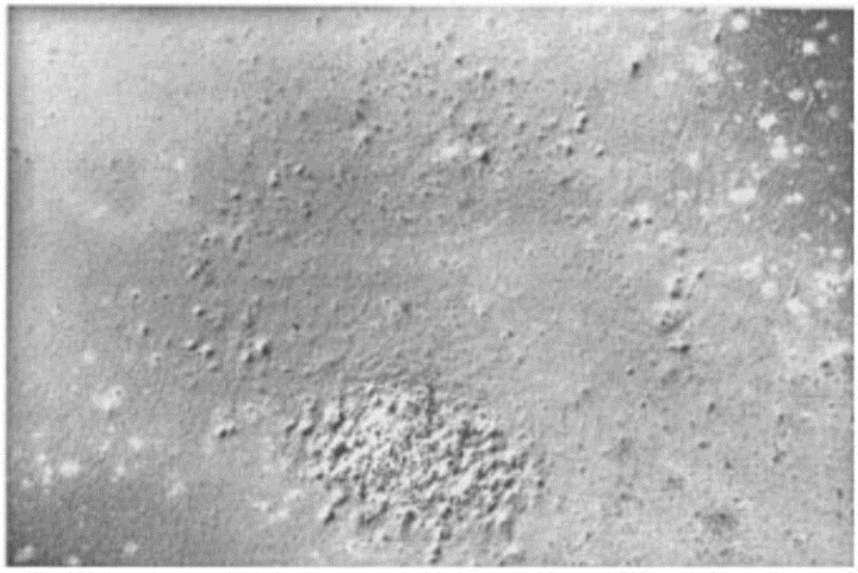

Fig. 19 5000 cavitation bubble on brass at γ = 1.28 and r = 1.45 mm. The laser enters from the direction of bottom of the image (adapted from [11]).

3.3.2 Material Microstructure

Hanke and Kaiser investigated the damage on technical alloys due to multiple single bubbles [3]. The damage caused by s series of single laser-induced bubbles was compared to the damage from acoustic cavitation. They found that on the microstructure level the damage looked similar in both acoustic and single-bubble cavitation [3]. The work of Lopez et al. showed quite similar results [78]. In this work the effects of repeated single bubbles were studied in more detail. The focus of the work was on the progress of surface changes from the early stage of cavitation damage to the first erosion detected via SEM (scanning electron microscopy). The

materials investigated were identical with those in this work, i.e., all ductile metals. It was found that the accumulation of small pits causes plastic deformation leading to plastic flow. Where erosion first starts, however, depended on the microstructure of the tested material. For 316L stainless steel the damage first occurred at grain boundaries, while the first damage for nickel-aluminum bronze was found at intermetallic particles and phase boundaries [78]. This also means that there was similarity across the materials in that the material removal always occurred where the plastic flow in the material was hindered.

3.3.3 Damage Mechanisms

The damage mechanisms – here, the causes of damage on the fluid-dynamic side of the interface – are a long-debated topic in cavitation.

Fig. 20 shows a scheme of a collapsing cavitation bubble with some of the potential causes of surface damage (jet, shock-wave emission). However, the bubble collapse can occur in very different ways depending on γ (as described in Section 3.1) and Fig. 20 is just one possible example shown.

In 1986 Tomita and Shima suggested the jet from single-bubble collapses responsible for the damage [54]. However, in their work, they amplified the collapse with external shock waves. In their work Philipp and Lauterborn 1998 assumed a more direct connection of the damage with shock waves that occur very close to the surface [11].

Over the last years some publications addressed damage mechanism especially on aluminum [10, 12]. On this soft material, a direct link between the jet and the resulting damage was suggested to be the cause of at least some of the damage, because the liquid jet can hit the surface with up to 1000 m/s [71, 79] (though usually much slower [11]), depending on the stand-off distance. However, there was doubt because of the damage in relation to the area of the jet impact [12]. Experiments on an aluminum foil of Dular et al. showed both jet and shockwave could damage their samples [80]. However, it is not clear how their findings translate from foil to bulk materials.

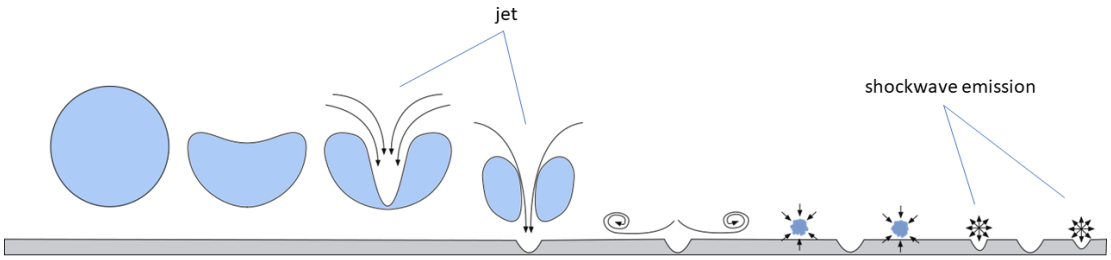

Fig. 20 Schematic overview over the collapse of a cavitation bubble. Potential damage mechanisms like the jet or the shockwave are drawn into the scheme. Adapted from [80].

A recent publication of Reuter et al. focused especially on small $\gamma < 0.3$ [81]. For this small γ, shockwave focusing was observed that leads to extreme strong collapses of the last part of the cavity [81]. Fig. 21 shows the schematic of the shockwave emission from a bubble ring. The collapse of a part of that ring leads to the further collapse of the ring in the vicinity of the collapsing area due to its shockwave emission. The shockwave-induced collapse itself then leads to further amplification of the shock front. They observed a similar, but weaker, effect at subsonic speed around $\gamma = 1.4$ [81].

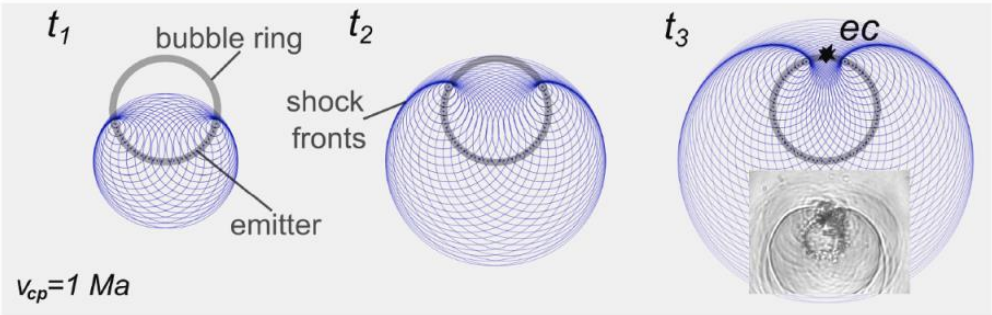

Fig. 21 Shock wave self-focusing (adapted from [81]).

4. In-situ Investigation of the Onset of Cavitation Damage from Single Bubbles on Technical Alloys

For clarity, some definitions are provided first: During the life of the bubble, several collapses and rebounds take place [11, 50]. This work examines both the initial collapse of the bubble, as well as the second collapse that occurs after the bubble rebound. A **collapse** is defined here as the shrinking of the spatial extent of the gas phase in the fluid towards a local minimum. However, in the literature this local minimum itself is often called the “collapse”. In keeping with this, if it is not explicitly stated which of the individual spatio-temporal minima is meant (first, second), “collapse” may also refer to the overall process. During this process, the sample surface becomes subject of **load** due to different phenomena like liquid jets or shockwaves. A **pit** is defined here as a permanent depression (plastic deformation) in the surface caused by a single event in the bubble collapse that is short compared to the overall time of the bubble collapses and rebounds. As will be seen, the radius of pits is always more than one order of magnitude smaller than the maximum bubble radius. More generally, (cavitation) **damage** is defined as any permanent change in the surface. Such a change does not necessarily mean **erosion**, which is the removal of material, but may simply be due to plastic deformation. Two kinds of **mechanisms** appear in our discussion: On the one hand, the way the fluid dynamics lead to a presumed load on the material (jet, shock waves), on the other, how that load leads to damage in the material.

4.1 Chapter Introduction

This chapter presents the initial experiments conducted to investigate the damage caused by single bubbles on technical alloys. The aim was to identify similarities and differences between this damage and that observed in aluminum.

To address this, we developed an optical arrangement that enables observing the surface of the sample during a running experiment. Near a sample immersed in water, series of single bubbles are created by focused laser pulses, and their effects are observed with an in-situ microscope. This method not only provides insight into the course of cavitation damage of technical materials but also can be used to evaluate the cavitation erosion resistance from the rate of single-bubble

damage accumulation. Most of this Chapter has been published in Kühlmann et al. [82].

4.2 Methods and Materials

The formation of cavitation damage was investigated on a stainless steel (316L, X2CrNiMo18-15-3, 1.4441), a nickel aluminum bronze (NAB, CuAl10Ni5Fe5), and pure aluminum (Al 99,999%), the latter to make the connection with the more numerous experiments on softer materials. A more detailed description of the material properties can be found in [3, 10], and micrographs are shown in the Appendix. The samples were cylindrical with a diameter of 12 mm and a thickness of 8 mm and their surface was polished. The cavitation bubbles were created approximately above the center of the flat face of the cylindrical sample.

Fig. 22 Schematic views of the experiment. a) top view of single-bubble generation and detection, b) side view of the in-situ microscope, c) trigger sequence shows the optical arrangement. The experiment consists of three orthogonal optical trains at different wavelengths, one for pulsed-laser generation of a bubble, one for imaging the bubble dynamics, and a microscope viewing the sample surface in-situ. To generate bubbles, a 1064 nm nanosecond-pulsed Nd:YAG laser was focused into a cuvette filled with deionized water. First, the beam was expanded and passed an adjustable aperture. Two axicons then shaped the round transverse laser beam profile into a ring. This way the plasma breakdown is more likely to occur near to the beam waist [83–85]. Finally, the beam was focused into the water with an auxiliary lens and an aspheric lens, the former compensating for the refractive index of water that the latter was not designed for. The bubble dynamics were recorded orthogonal to the direction of laser incidence. To that end, a Phantom VEO 710 high-speed camera imaged the shadow of the bubble backlit with an LED with a center wavelength of 505 nm. At 90 000 frames per second (fps), 320x180 pixels were read with an exposure time of 10 µs. Series of 100 frames (about 1 ms) captured the relevant part of each bubble’s dynamics.

The microscope is shown in Fig. 22b. The sample surface, submersed about 20 mm below the water surface, was illuminated with an LED centered at 632 nm. A Mitutoyo Plan Apo 10x microscope objective lens and a Raynox DRC-250 tube lens provided a long working distance at a magnification of about six. To reduce aberrations caused by the water [43], a 6 mm aperture located just above the

objective lens limited the numerical aperture of the objective to 0.14. This also increased the depth of field, advantageous for observing deep damage. The laser was triggered at a repetition rate of 1 Hz for experiments targeting the early damage formation and with 15 Hz for experiments with many successive cavitation bubbles. Schott KG3 filters protected the sensor of the microscope camera and that of the high-speed camera from elastically scattered laser light. In the microscope, a round region with a diameter of about 2300 camera pixels was illuminated, corresponding to about 2.5 mm on the sample surface. The images were taken 5 ms before each laser pulse (i.e., bubble), as shown in the trigger scheme in Fig. 22c. Alternatively, with the delay set to zero, the microscope recorded the plasma breakdown in the liquid, which was used for optimization of the beam formatting optics.

In addition to this reflected-light in-situ microscopy, which may be limited in resolution and contrast and is not quantitative, selected samples were also examined with two other microscopic techniques *ex situ* after the experiment. Differential interference contrast (DIC) in an Olympus BX 41 microscope qualitatively visualized the surface texture, while a quantitative measurement of surface elevation was obtained with a NanoFocus µSurf confocal scanning microscope.

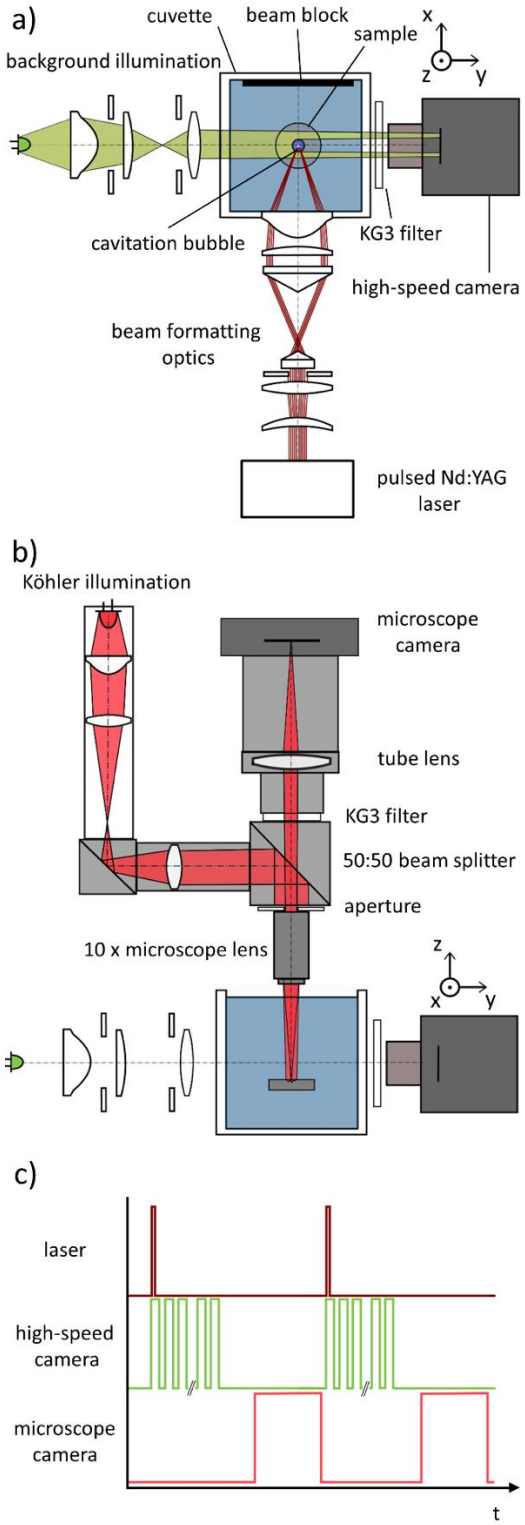

Fig. 22 Schematic views of the experiment. a) top view of single-bubble generation and detection, b) side view of the in-situ microscope, c) trigger sequence.

4.3 Results and Discussion

It is well-known that the dynamics of a bubble collapsing near a surface are strongly influenced by the stand-off distance γ [42, 56]. Most of the current experiments were performed at γ = 1.3 to 1.4, a range for which a relatively complex damage pattern occurs, as will be seen below. An exemplary bubble collapse for γ = 1.4 is shown in Fig. 23. As in all images in this paper, the laser is incident from the left. The first frame at t = - 98 µs shows the plasma (whereas the central bright spot at later times is from the LED back-illumination) and the start of the formation of the bubble. After 98 µs the bubble reaches its maximum diameter. It collapses towards the surface and is pierced by a downward liquid jet [56]. The rebound and the second collapse in Fig. 23 at 272 µs and 380 µs, respectively, occur in a toroidal shape very close to the solid surface. Note that the reflection of the bubble shadow on the polished sample surface helps locate the sample surface with respect to the bubble. The small dark spots throughout the image are attributed to bubbles of dissolved gases that may not only stem from the air, but also possibly from the laser-induced breakdown plasma for the preceding bubbles.

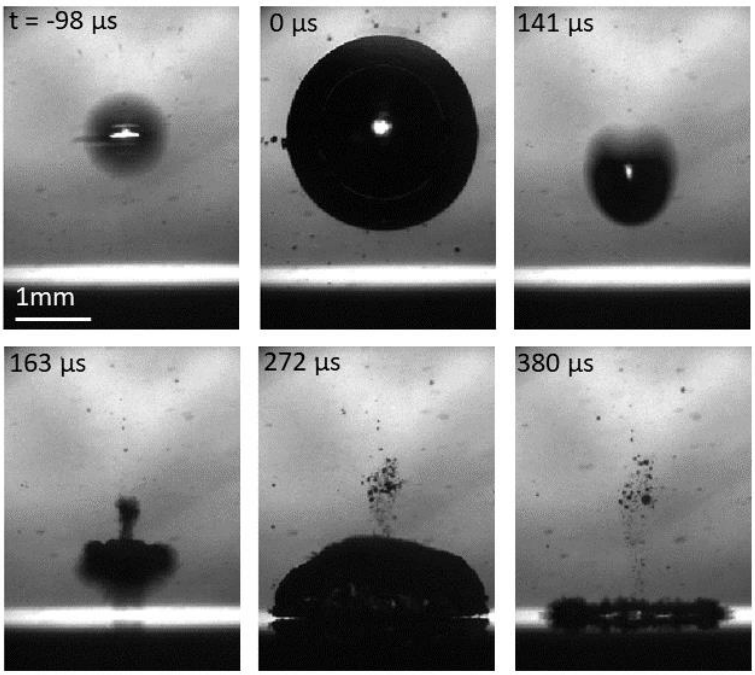

Fig. 23 Selected frames from an example recording of the dynamics of a 2.5 mm diameter bubble at γ = 1.4. Time zero is defined here as the time of maximum bubble diameter. The laser incident is from the left.

The number of bubbles impacting on the surface is another important parameter. Previous works indicated that it may take tens of thousands of bubbles to induce substantial damage in technical alloys [3, 8]. In order to obtain an overview of the damage evolution, such experiments were also carried out. However, the current work focusses on the beginning of the damage evolution, and therefore most samples were exposed to less than 1000 cavitation bubbles.

Fig. 24 shows three different microscope images of the cavitation damage on a 316L sample impacted by a series of 30 000 bubbles with a maximum diameter of 2.5 mm at γ = 1.4. The image taken by the in-situ microscope is shown in Fig. 24a. The other two, ex-situ images of the same damage, from confocal scanning microscopy (Fig. 24b) and a commercial light microscope with DIC (Fig. 24c), serve as a reference for the quality and informative value of the in-situ microscope images. The circular shape of the damaged region seen here is consistent with other works [11, 12]. There are both less damaged regions where individual pits can still be discerned, and a more severely damaged region. Thus, the quality of the images can be assessed in both of these damage scenarios, which may also be representative of earlier and later stages of local damage evolution.

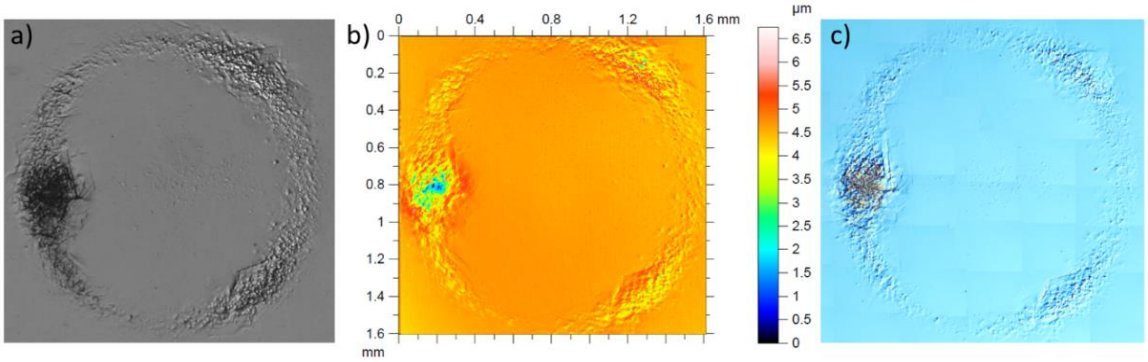

Fig. 24 Comparison of an in-situ microscope image on 316L after 30 000 individual bubble impacts compared with the ex-situ imaging of the same damage. a) in-situ image, b) surface elevation from confocal scanning, c) DIC image, assembled from about 60 frames acquired with a 20x objective.

Comparing Fig. 24a and Fig. 24c, the effects of aberrations caused by the 20 mm of water above the sample are visible as a slight blur in the in-situ image. But as far as the overview figure allows, all major features that can be seen in *ex situ* can also be found *in situ*. A more detailed ex-situ analysis can then complement that with quantitative measurements. For example, the confocal image in Fig. 24b shows that the depth of the most damaged region is 4 µm and that of a typical

single pit is about 0.25 µm, consistent with our previous work with the same material [3]. This then can be linked to the corresponding contrast in the in-situ image.

Series of measurements were performed with selected stand-off distances. The in-situ images in Fig. 25 give a first overview of the stages of the damage processes for aluminum, 316L, and NAB. The experiments on aluminum were performed to link to the literature results on soft materials. The samples were successively exposed to 30 000 single cavitation bubbles for 316L and 50 000 for NAB. Images at 1 500, 3 000, and 14 400 bubbles are also shown in Fig. 25. Aluminum was exposed to a number of bubbles that induced similar cavitation damage as on the technical alloys, with images at 11, 24, 48, and 150 bubbles shown here. For all three materials, with an increasing number of bubbles an increase in the damage becomes visible. At all stages, most of the damage is in a ringed-shaped area, best seen in the last images, and this is again consistent with the literature [11, 12]. The ring consists of smaller individual pits. For aluminum, after 11 bubbles already more than 25 individual pits can be detected. This means that one bubble can cause more than two pits on aluminum. The damage evolution on the soft aluminum shows some differences to that on the harder two materials. Besides progressing much faster, the pits are bigger, and the area surrounding each pit appears more deformed.

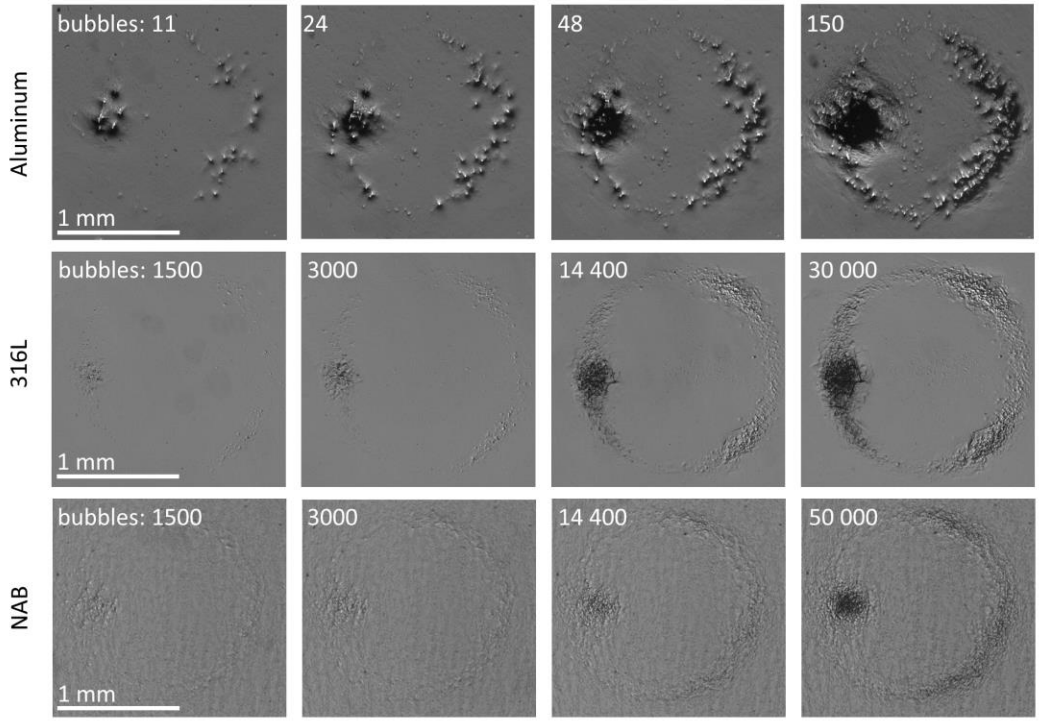

Fig. 25 Damage evolution on aluminum (top), 316L (middle), and NAB (bottom) at $\gamma = 1.4$ and r = 2.6 mm bubble radius.

Our findings are consistent with those of Philipp and Lauterborn [11] and Isslin et al. [12] in that they show an asymmetry in the otherwise ring-shaped damage patterns, with an area of more severe damage towards the direction of incoming laser light. This is most likely due to an asymmetry in the plasma breakdown [11], which is not spherical, but rather elongated and conical [29], as Fig. 23 at t = - 98 µs indicates. Among all stand-off distances, $\gamma = 1.4$ creates the laterally most extended damage area, which may make the damage more prone to such asymmetries (see [11] for damage patterns with other stand-off distances). In fact, experiments with this γ-value can be used to detect plasma asymmetries that otherwise are difficult to visualize.

Among the two technical alloys, in good agreement with our previous work, NAB shows greater resistance to cavitation exposure than 316L in that the optically detected damage appears less severe after the same number of cavitation bubbles [3]. Also, the change in surface-damage appearance differs between 316L and NAB. The difference increases with the number of bubbles. For 316L, after 30 000 bubbles almost the full circumference of the ring-shaped damage displays pits. The

damage concentration towards the incident beam appears very dark, indicative of its great depth. On the opposite half of the ring, two regions with less pronounced damage accumulation are recognizable (at approximately 1 and 5 o'clock). On NAB all these features appear less pronounced, and regions adjacent to the most damaged region on the side of the incident beam display almost no damage in these images. Furthermore, the surface of the NAB sample in general appears less smooth, showing small-scale grey variations in brightness in the image. This is caused by the complex microstructure in NAB, which contains both areas of high density of hard intermetallic phases, and others consisting mainly of softer Cu-rich solid-solution phase. A small difference in surface height between these different regions after polishing the sample surface causes the diffuse grey shading of the surface. The hard phases improve NAB's resistance to cavitation exposure by hindering plastic deformation and limiting pit dimensions. 316L on the other hand is a single-phase material, in which only grain boundaries and strain hardening limit pit formation by plastic deformation, which may act in NAB as well. Therefore, damage appears less pronounced in NAB, consistent with previous findings [3]. While the collapsing bubbles clearly change the surface topology, it is not clear if conversely these changes in the surface influence the bubble dynamics and thus potentially the further damage progression. Recent studies show that purposeful texturing of the surface can lead to reduced cavitation erosion [86, 87]. It was suggested that a change in topology may affect the primary dynamics of the bubble [87] as well as secondary phenomena during the collapse [86].

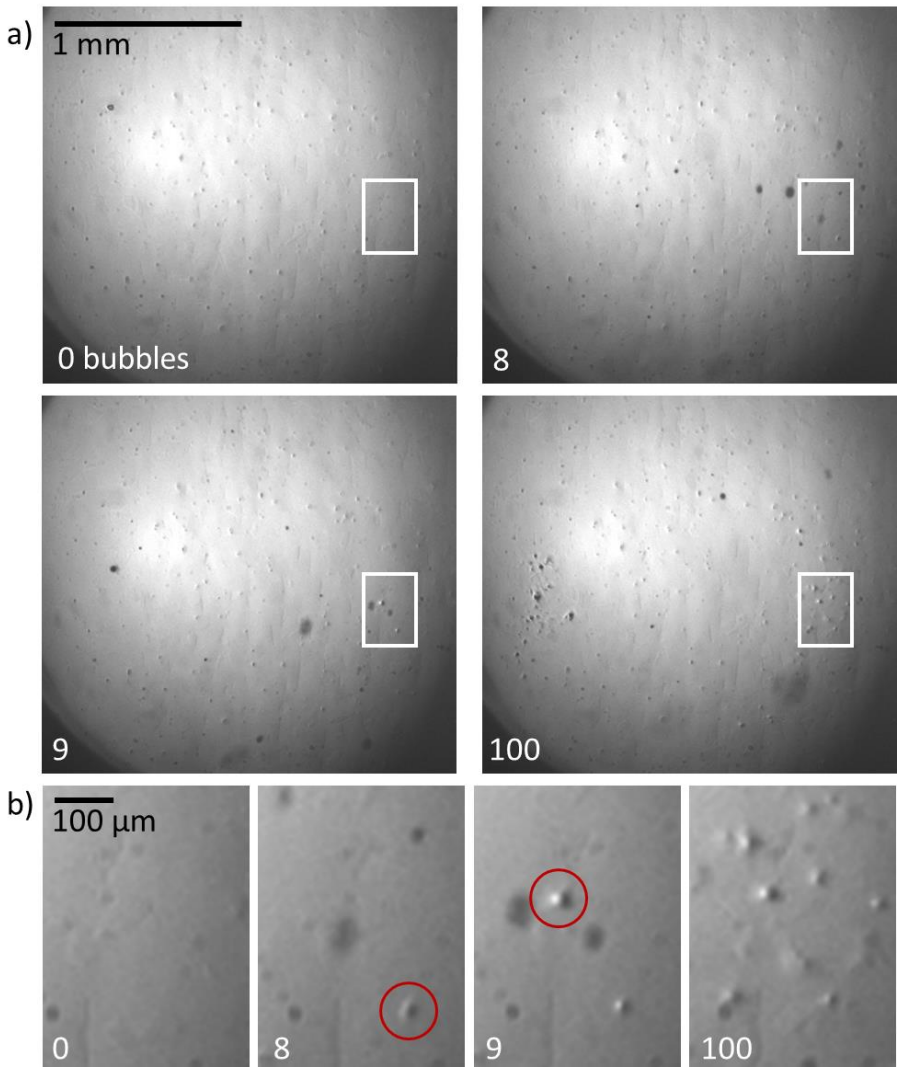

Fig. 26 Damage formation on 316L at γ = 1.4 and r = 1.25 mm bubble radius. a) full field of view, b) magnified region corresponding to the white rectangle in (a). The red circles mark features discussed in the text.

Fig. 26 shows four microscope images from a 316L sample, taken after 0, 8, 9, and 100 bubble collapses, as well as a magnified region within each of these images. As discussed with Fig. 24, the dark, more or less diffuse spots that change position between images are shadows of small bubbles remaining after the preceding bubble collapse. After the 8th bubble, the first pit appears, as marked in Fig. 26b. The next pit occurs already with the next (the 9th) bubble. This pit is then due to exactly the single preceding bubble. After 100 bubble collapses these two pits can still be identified. Note that the visual appearance of a given pit may change slightly between images. This is due to the fact that the water surface through which the images are taken is not perfectly still. The small pits that are the result of the bubble

collapses later accumulate to form the larger ring structure as discussed above. As for the individual pits that now can be assigned to specific bubbles, we have not yet identified any feature in those particular bubble collapses that produce the pit in that particular spot. Nevertheless, the small size of the pit indicates that this damage might not have been caused by the first bubble collapse (for example, by the jet [8, 80]) but a smaller-scale event in the second toroidal-shaped collapse, as already suggested by other works [8, 80, 88].

Indeed, Fig. 27. shows that the damage ring is located under the second, toroidal bubble collapse. Still, it remains unclear what exactly caused a pit in a given spot. It may have been a particular, local feature of the bubble. An asymmetry in the torus of the second collapse can clearly be seen in Fig. 27 a) to c). Regions on the ring displaying damage accumulation as described above (see Fig. 25) appear darker in the high-speed camera images, indicating the presence of more and possibly larger bubble structures. The shockwave emitted from the initial bubble might be a central part of the bubble dynamics as it has the potential to grow cavitation nuclei in the vicinity of the solid boundary [80, 88].

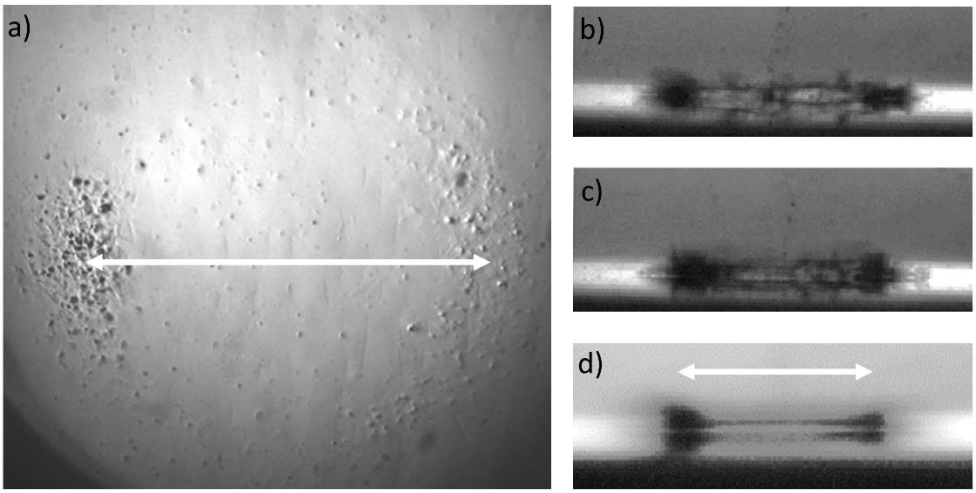

Fig. 27 Relation of (a) the damaged region as seen by the in-situ microscope after 1000 bubbles and b-c) the second collapse visualized with the high-speed camera. b) and c) are single shots of the second collapse in selected bubbles, while d) shows the mean of 200 collapses. The arrows in both images correspond to 1.55 mm. The images are from the same sample as those in Fig. 26.

In Fig. 28 the damage progression is shown for $\gamma = 1.7$ on NAB. For this stand-off distance less damage was observed than for $\gamma = 1.4$, as can be seen by comparison with Fig. 25 (NAB 14 400 bubbles). The first pit appeared after the 6th

bubble, and two pits were caused by the 16th bubble collapse. Thus, even on technical materials, it is possible for one bubble collapse to create more than one pit. For γ = 1.7 the damage pattern after many bubbles is not a ring but a smaller, central area that is again formed by smaller pits. The damage shape is consistent with measurements with this γ by Philipp and Lauterborn on a soft sample [11]. The last image in Fig. 28 shows that the first three pits are not clearly recognizable anymore at a count of 17 500 bubbles, because they are covered by further pits.

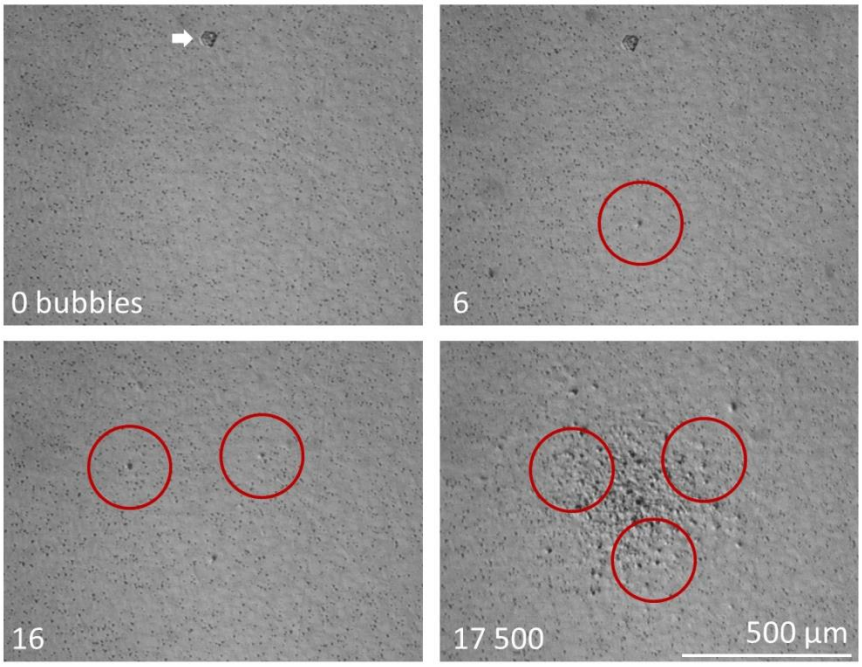

Fig. 28 Early damage formation after 6 and 16 bubbles, and accumulated damage after 17 500 bubbles on NAB with γ = 1.7. The circles mark features discussed in the text. The white arrow in image 0 marks a feature that is an adhering particle of dirt that detached from the sample surface between the 6th and the 16th bubble.

We see that for both technical alloys the initial surface damage begins after only a few bubbles – in fact, so few, that it seems likely that for a given sample already the first bubble may cause a pit. The cause of the pits seems to have a stochastic component, as neither their time of appearance nor their exact locations currently seem to be predictable, apart from the general location that is dependent on the stand-off distance γ.

To obtain a quantitative measure of early damage progression, we counted the pits after each bubble within a series. Pit counting was done by visual inspection, and the size and shape of the pit was disregarded. Fig. 29 shows the result for series

of 100 successive bubbles for the three materials, with two samples for NAB. Between zero and six additional pits are found after a single collapse. The slope of this pit-count graph, approximated here as a linear fit through the origin to each data series, is then the series-mean pitting rate. The parameters of these experiments and the pitting rate are listed in Tab. 1. About 50 pits could be counted on a single sample before it became hard to distinguish overlapping pits. Beginning pit overlap may also be the reason why the slope of all traces decreases towards higher pit counts. The pitting rates have the same order among the materials as the corresponding material hardness, as does the maximum number of pits after a single bubble collapse. After one collapse, 0-2 pits occurred on NAB, 0-3 on 316L, and 0-6 on aluminum. It is also remarkable that on one hand, even a soft material like aluminum did not show damage after every collapsing bubble. On the other hand, sample B8 from the hard NAB had a pit after the very first bubble. The two NAB samples differ slightly in their bubble parameters and in the pit count progression, but in this initial demonstration it is not clear if the difference is significant.

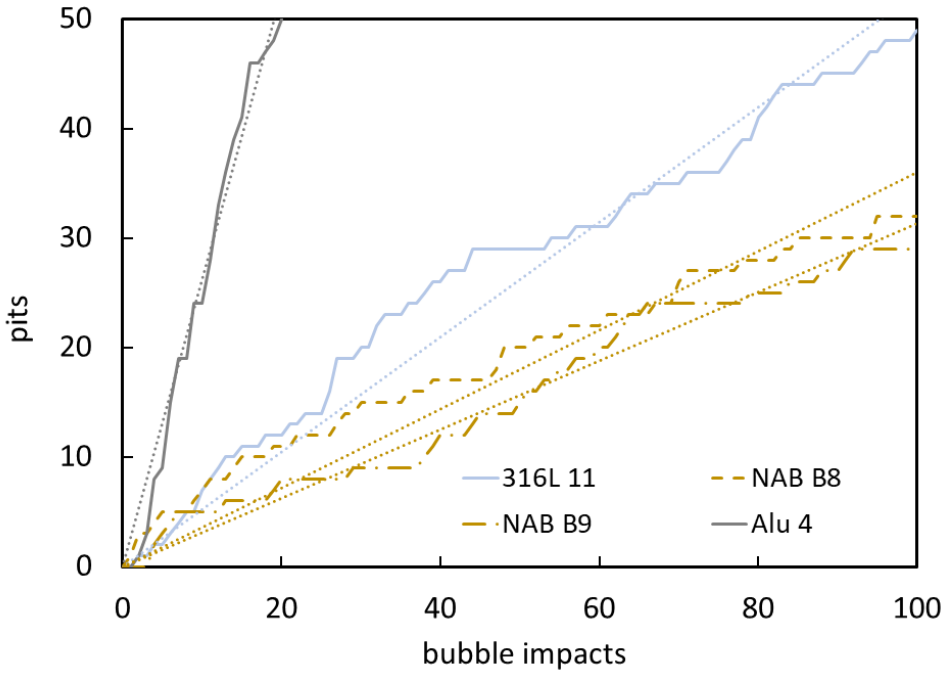

Fig. 29 Pit count per bubble and linear fit of the pit count. For NAB, two samples were considered, as indicated in the legend after the material designation.

	NAB sample B8	NAB sample B9	316L sample 11	Aluminum sample 4
Hardness [HV 0.05]	201 ± 6		168 ± 6	22 ± 1
γ	1.36	1.28	1.36	1.30
Radius [mm]	1.23	1.3	1.36	1.25
Mean no. of pits/bubble	0.36	0.31	0.51	2.6
Min - max no. of pits/bubble	0 – 2	0 – 2	0 – 3	0 – 6

Tab. 1 Parameters of the experiments and results of the pit counting presented in Fig. 29. The hardness was not measured on the samples used here, but on other samples from the same material and with the same processing.

4.4 Chapter Conclusions

In-situ microscopy was established as a method for studying single-bubble induced cavitation damage. The basic idea is to generate successive single bubbles with a focused laser, and then take an in-situ microscope image of the surface after each bubble. The technique was tested for three different materials – pure aluminum, a stainless steel, and a nickel-aluminum bronze – and was validated against established ex-situ microscopy techniques. The images from the in-situ microscope showed good general agreement with the ex-situ analysis. The damage patterns observed on the samples for the stand-off distances considered here are consistent with the much earlier work of Philipp and Lauterborn [11] as well as with more recent studies [3, 11]. For all three materials this pattern is formed out of an accumulation of smaller pits, each of which may be caused by events in the second collapse of the cavitation bubble. However, as expected the rate of the damage progression greatly differed between the soft aluminum and the two harder

technical alloys. The in-situ imaging shows that the response of the material surrounding the pits was different for the steel and the bronze.

The first onset of visible cavitation damage was investigated in more detail. With the in-situ surface microscopy it was possible to identify the appearance of individual pits and attribute them to a specific bubble. Somewhat surprisingly we found that even on the hardest material, the bronze, the very first bubble can cause damage, and some bubbles even create two pits. Conversely, on the soft aluminum not every bubble causes a visible pit, even though most yield more than one. This bubble-by-bubble damage progression was quantified as a pitting rate by counting the pits over series of bubbles until they started to overlap often, which was the case at about 50 bubbles. Pit counting was done by visual inspection here, but should be amendable to automation, and could then be used for a systematic and statistically sound investigation of the onset of single-bubble cavitation damage. For prevention of cavitation damage, it might be significant that there are bubble collapses that do not cause visible damage. From the current experiment, even though for each pit the corresponding bubble was recorded (in a side view) on a high-speed camera, we could not find an obvious connection between bubble dynamics and occurrence or exact location of a pit. If we could prevent whatever stochastic part of the bubble dynamics is responsible for the pits, that might prevent damage.

5. Correlation of Laser-Induced Single Bubbles with Cavitation Damage via In-Situ Imaging

5.1 Chapter Introduction

The primary damage by single collapsing cavitation bubbles for $2 > \gamma > 1$ is the formation of small pits [11, 12, 80]. A key result of previous chapter was that even on high strength materials, pits can appear after just a few bubble collapses [82]. Less surprisingly, pits are more likely to appear on soft than on technical materials. The exact location of the pits seems stochastic, apart from the fact that it is where the collapsing bubble is in (or nearly in [59]) contact with the solid surface. Successive impacts of single cavitation bubbles lead to a growing number of pits. In acoustic cavitation experiments, pitting can then activate different wear mechanisms that are dependent on the material [3, 89]. Hence, in order to understand the course of early cavitation damage, we here investigated how the pitting is caused and what the differences in the pitting of different materials are. Furthermore, it is not clear what leads to the seemingly stochastic spatial location of the pits. The question remains to what extent the bubble dynamics and the material properties are responsible for a specific location of a single pit.

To address this question, experiments with series of laser-induced single bubbles were carried out on Al-, Cu- and Fe-base alloys. The bubble dynamics were recorded by two high-speed cameras, while the resulting surface damage was investigated by a microscope *in situ*. The resulting pits were analyzed and the different alloys were compared in their pitting behavior.

The work was mostly published in Kühlmann et al. [90] and was presented at the 24th International Conference on Wear of Materials in April 2023.

5.2 Methods and Materials

We investigated samples made out of stainless steel (316LVM, X2CrNiMo18-15-3, 1.4441), nickel aluminum bronze (NAB, CuAl10Ni5Fe5), as well as pure aluminum (Al 99.999%) - the latter to relate to the experiments on softer materials. The microstructure of the aluminum can be seen in Fig. 30a. 316LVM was used in its solution-annealed state, meaning it has a homogeneous single-phase

microstructure (Fig. 30). The NiAl-bronze has a complex microstructure, consisting of a copper-rich matrix and hard intermetallic precipitates containing Fe, Ni, and Al (Fig. 30c).) All samples were polished using standard metallographic methods, so a change of the surface due to cavitation collapses should be well visible. The samples were cylindrical with 12 mm diameter and a thickness of 7 mm. The bubble was induced approximately above the sample center.

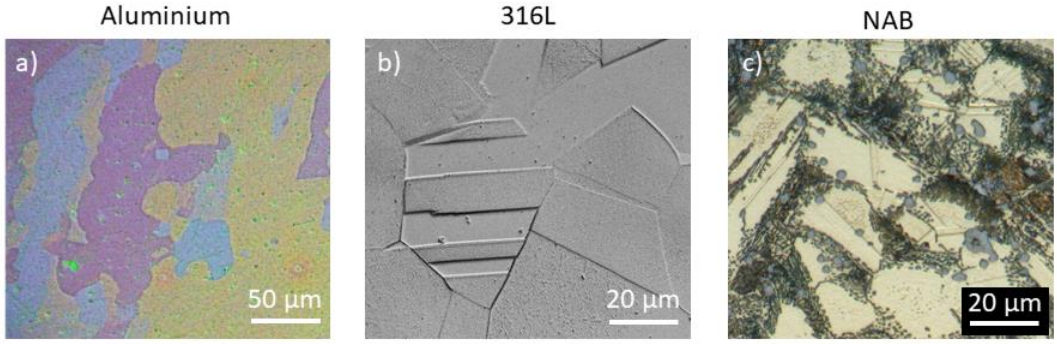

Fig. 30 Microstructure of the tested materials. a) Aluminum color etching according to Barker [91] b) 316LVM stainless steel, electrolytically etched with 10% oxalic acid c) Nickel aluminum bronze, 2-step wet etched: 1-2 s in 40 ml H_2O, 40ml NH_4OH, and 2 ml H_2O_2; 1-2 s in 60 ml H_2O, 30 ml H_3PO_4, and 10 ml H_2O_2.

Most of the experiment is described in detail in the Section 4.2. Key parts are summarized here for completeness. Fig. 31. shows the optical setup from the side (a) and top (b). Three orthogonal optical trains were arranged, each at a different wavelength: pulsed-laser generation of a bubble, imaging the bubble dynamics from the side, and imaging the sample surface in-situ and the bubble dynamics from the top. To induce bubbles, a 1064 nm nanosecond pulsed Nd:YAG laser beam was focused into a cuvette filled with deionized water. A more detailed explanation of the beam shaping is given in appendix Section 10.3. The laser was triggered with 3 Hz. Orthogonal to the direction of laser incidence, the bubble dynamics were recorded from top and from the side. The lateral view is particularly important to determine γ. To that end, a Phantom VEO 710 high-speed (HS) camera imaged the shadow of the bubble backlit with an LED with a center wavelength of 505 nm (Fig. 31a). At 86 000 frames per second (fps), 320x180 pixels were read with an exposure time of 10 µs. Series of 100 frames (i.e., about 1 ms) captured each bubble's dynamics.

The in-situ microscope is shown in Fig. 31a. The sample surface, submersed about 20 mm below the water surface, was illuminated with an LED centered at 632 nm. A Mitutoyo Plan Apo 7.5x microscope objective lens and a Raynox DRC-250 tube lens provided a long working distance at a magnification of about 5. To reduce aberrations caused by the water [82], a 6 mm aperture located just above the objective lens limited the numerical aperture of the objective to 0.14. This also increased the depth of field - advantageous for observing deep damage and the bubble dynamics above the surface.

For the experiments presented in this and the following chapter, we added a second HS camera (a Phantom v1612 at 60 000 fps) to the experiment (Fig. 31b), sharing the view of a higher-resolution (HR) camera through a microscope onto the sample surface. A 10:90 beam splitter directed 90% of the light to the HS camera whose exposure time was much shorter than that of the HR camera. While HS camera was used to visualize the dynamics of the bubble, the HR camera imaged the sample surface with more detail. A circular region of about 3 mm diameter (corresponding to about 2200 camera pixels) of the sample surface was illuminated and imaged on the sensor of that camera. Schott KG3 filters protected the various camera sensors from elastically scattered laser light.

The samples were exposed to 100 – 500 successive cavitation bubbles at a stand-off distance of γ = 1.35 +/- 0.05. For this γ, a torus-shaped second collapse occurs [11, 52]. The extensive region of this collapse gives the best optical access to features in the collapse.

After the experiment selected samples were examined *ex situ* in a quantitative measurement of surface elevation, obtained with a NanoFocus µSurf confocal scanning microscope. A comparison of the images obtained via the in-situ microscope and the ex-situ recorded images is given in [82]. We found that despite imaging through 20 mm layer of water good image quality can be achieved.

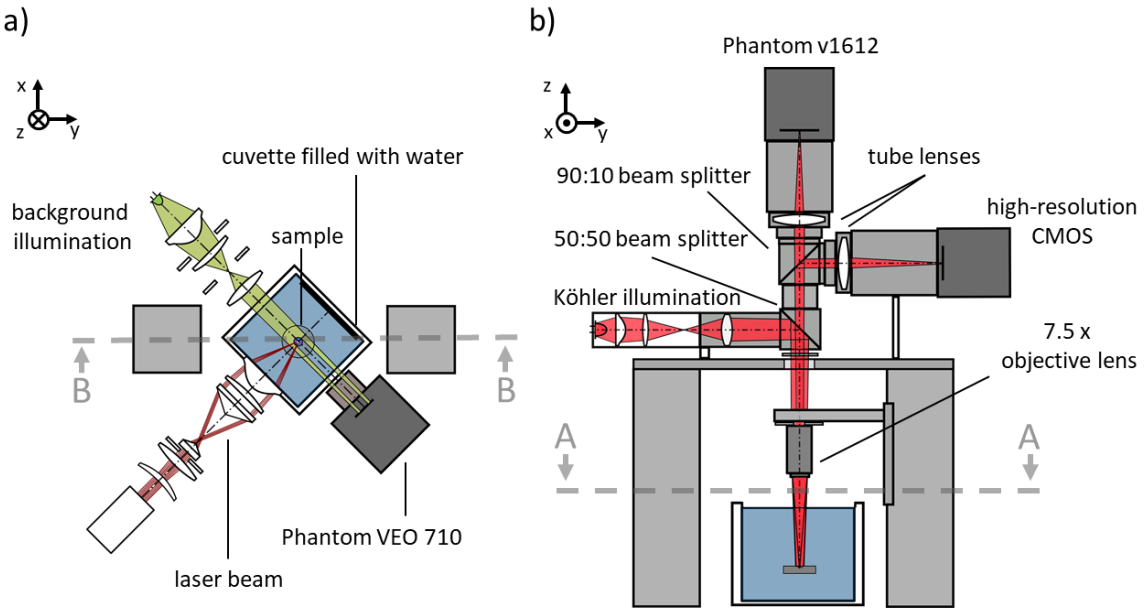

Fig. 31 Schematic views of the experiment. (a) is the view as seen from the cut plane A, and (b) is the view as seen from the cut plane B. In (b), the optics appearing in (a) have been omitted for clarity.

5.3 Results and Discussion

5.3.1 Bubble Dynamics and Damage Detection

Fig. 32 shows selected frames from a typical bubble collapse from both the side and the top views. The two views give optical access to different, specific features in the collapse. The example shown here is for a bubble with r = 1.2 mm and γ = 1.4. The time at which the bubble reaches its maximum radius is set as t = 0 µs. During the then following collapse (100 and 130 µs, side view) the bubble moves towards the solid surface. The bubble is pierced by a downward liquid jet that cannot be seen here directly [28, 55]. The bubble's minimum extent in first collapse is reached before the bubble reaches the surface, and after contact with the surface the bubble grows again (165 µs, 232 µs). The second bubble collapse takes place in a toroidal shape (300 µs and 315 µs, top). This toroidal shape is due to outward momentum left from the centrally impinging jet before. This collapse process is consistent with what was found in many other works, e.g. [11, 52].

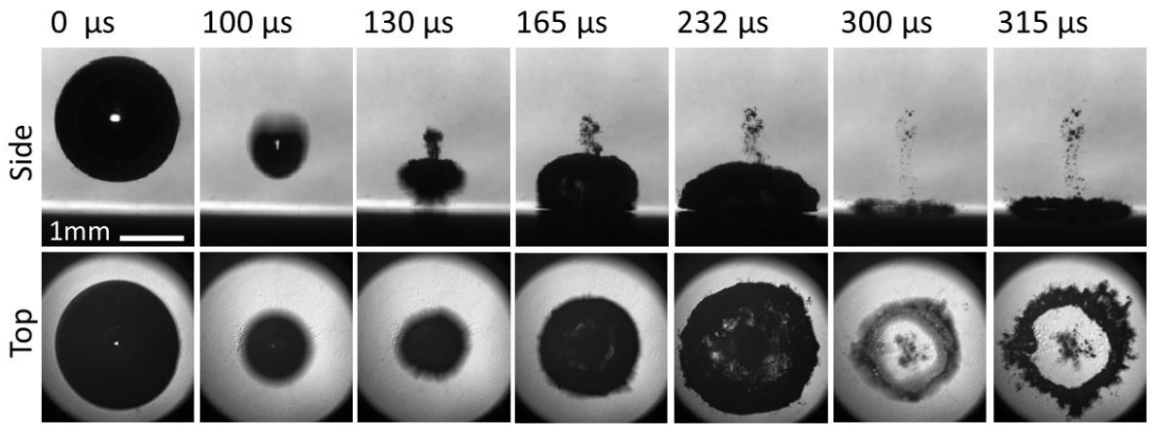

Fig. 32 Selected frames from an example recording of the dynamics of a 1.2 mm radius bubble at γ = 1.4 from top and side perspective. Time zero is defined here as the time of maximum bubble diameter. The laser is incident from the left.

An example image of the resulting damage is shown in Fig. *33*. This 316LVM sample was exposed to 500 cavitation bubbles. Many small pits form a larger damage pattern. Further examples of the damage that forms from single bubble cavitation are given in [11, 82]. The shape of the damage pattern that forms out of the many individual pits has previously been found to mainly depend on the shape of the bubble collapse in the vicinity to the solid surface [11], which is a toroid for γ = 1.3, the distance examined in this work [11, 82].

The asymmetry of the damage is discussed in [11] and is probably caused by the asymmetric plasma which is further discussed in Section 10.3. Parts of the asymmetry of the initial conditions appears in the later stages of the bubble collapse, even though the initial bubble that forms is nearly spherical. As a result of this asymmetry, pits are more likely to occur on specific parts of the ring, here to the left and the right in the image. Thus, the accumulated damage pattern becomes asymmetric as well.

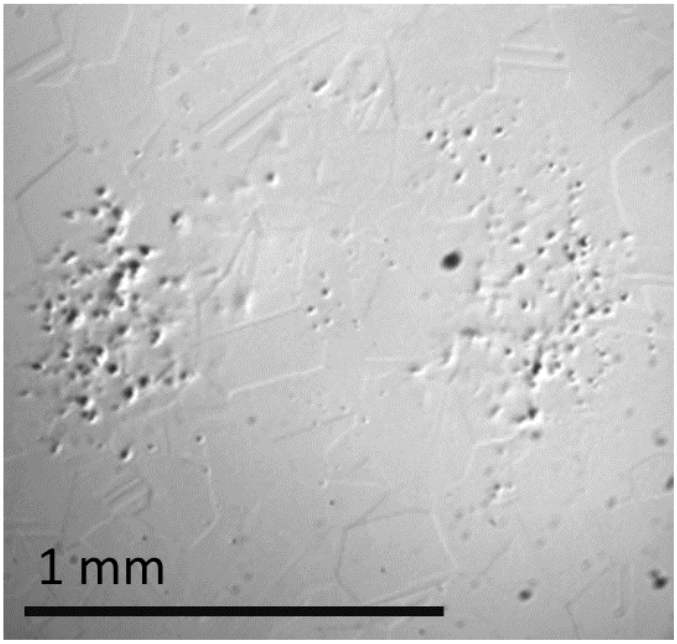

Fig. 33 Cavitation damage on 316LVM after 500 successive cavitation bubbles.

5.3.2 Correlation of Pits and Bubble Dynamics

Fig. *34* shows three different cavitation bubbles on NAB at the maximum radius (t = 0 µs), two images near the second collapse (315 µs, 333 µs), and the surface after the collapse (0.6 s) recoded by the HS camera. Additionally, the figure shows an HR image of the surface region with higher magnification. This image was recorded just before the next bubble. Shown are the first three bubbles that produced pitting on the surface, which in this particular experiment were the second, third, and fifth bubble. The first and the fourth bubbles did not produce detectable damage. The pits in the HR images are marked with a red circle, whereas the arrows in the HS images connect the pits with the corresponding spot in the images of each second collapse. Despite the very similar initial conditions of the three bubbles (γ = 1.3, r = 1.25 cm) we can see differences between the collapses. In particular, there are some areas along the toroidal second collapse where shortly after the collapse (333 µs) the shadow of the gas/liquid interface appears larger and with “jagged” edges. The former indicates that there is locally more gas, the latter is likely to stem from motion blur over the 10 µs exposure time, indicating locally high interface velocities. For lack of a more physically motivated term we will call these spots “strong collapse area” (SCA). Such an SCA is found for the second bubble in the upper left of the collapse toroid (“11 o´clock”), at 9

o'clock for the third, and at 3 and 9 o'clock for the fifth bubble. Often, as is the case here for the 5th bubble, if one bubble caused two pits, both the pits and the corresponding SCAs were on opposite sides of the toroid. Fig. *34* (333 µs and 0.6 s) shows that the regions of SCAs in the second collapse are where then after the bubble the pits are found. The small dark spots in the images are probably from dissolved-gas bubbles. Their contrast and shape may vary depending on their distance from the focal plane.

On the NAB, for all pits a preceding SCA in the same area can be found. However, the converse does not hold true: not every SCA in a second collapse led to a pit on the surface. One explanation for this could be the microstructure of this particular material. In the NAB there are hard intermetallic phases in a softer matrix material and thus spatial variation in local material response. The 316LVM examined next does not have these different areas in its microstructure.

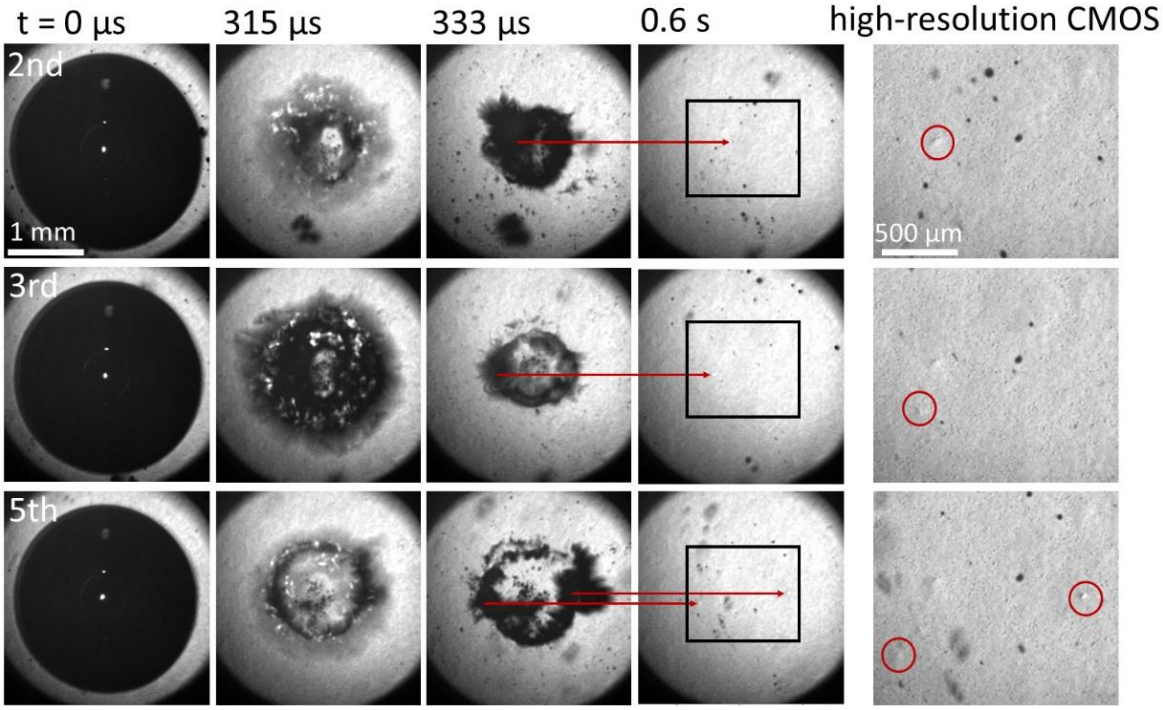

Fig. 34 Top view of the three first bubbles that produced a visible surface change on NAB and the HR images of the surface after the respective bubbles. The arrows connect corresponding areas in two images. Red circles mark pits in the HR image. The small dark spots in the images are probably from dissolved-gas bubbles.

Fig. 35 shows a series of three bubbles on the 316LVM (5th- 7th bubble) with radius r = 1.25 mm and γ of about 1.35. The structure of this figure is the same as that of

Fig. 34. Again, SCAs where found in the HS images of the second collapse, as well as pits that are marked with red circles in the HR images. The pit marked with a blue circle had been produced by a previous bubble. For the seventh bubble a HR image of the relevant region is given before and after the collapse.

Each bubble produced at least one pit. Interestingly, while these pits are each linked to a preceding SCA, the damage-producing SCAs in the fifth and sixth bubble are neither the only nor the largest ones. In 316LVM the surface properties do not vary much spatially. We conclude that the SCAs are a key factor in the creation of a pit, but there still are other contributing factors. One such phenomenon that might play a role is described in the last part of the results and discussion section. For the 7th bubble again two pits appeared that could be linked to the larges SCAs (9 and 2 o'clock). The region of one of these pits is shown in Fig. 35 in two HR images before and after the collapse.

From acoustic cavitation experiments Niederhofer et al. suggested the microstructure to be a critical part when it comes to the effect of several successive pits [92]. The 7th collapse in Fig. 35 is a case in point for a pit on or very close to grain boundaries or a twin boundary. These boundaries could act a s a barrier for displacement moment [89]. Here, one single pit did not cause a change of the boundary structure. In general, it could not be observed that an individual pit caused a change in the boundaries. However, several studies showed that a summation of individual pits may lead to a shear of the grains that permanently weakens the integrity of the material [3, 89, 92].

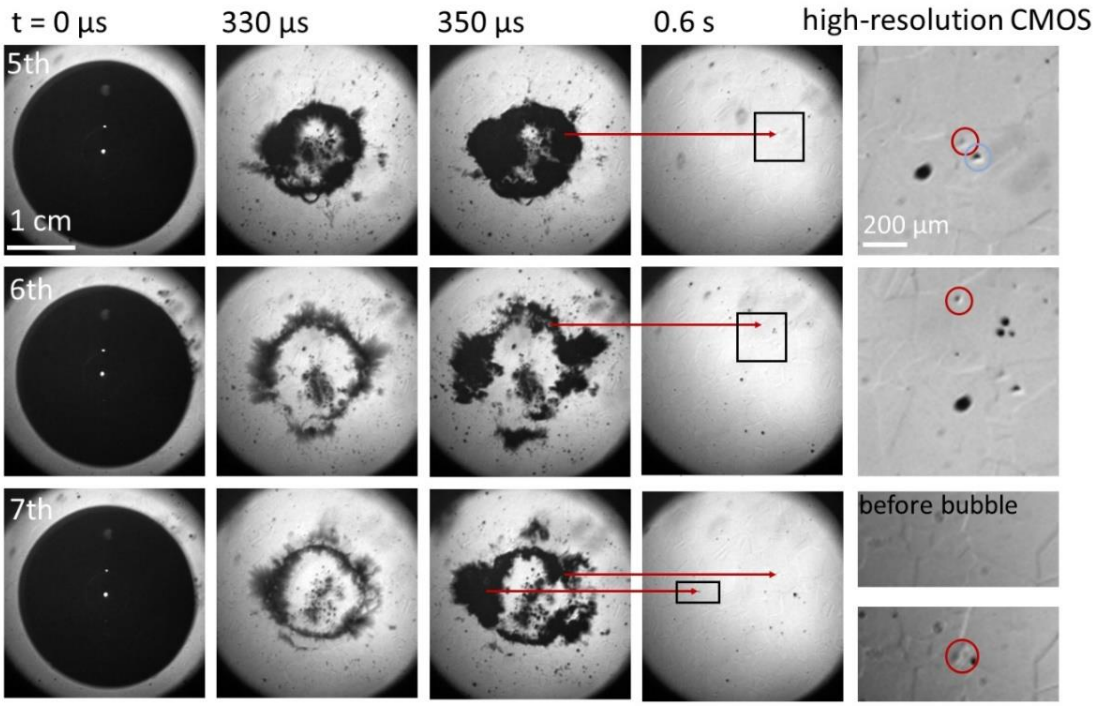

Fig. 35 Top view of the three first bubble collapses that produced visible surface change on 316LVM and the HR recordings of the surface after each bubble. The arrows connect corresponding areas in two images. Red circles mark pits in the HR image. The blue circle marks a pit from an earlier bubble in this series

Fig. 36 shows the first three bubbles on aluminum (γ = 1.4 and r = 1.3 cm). In all three examples, the torus-shaped collapses have a larger diameter than those in Fig. *34* and Fig. 35. The reason for this is the slightly greater γ here. A change in torus diameter depending on γ is consistent with other work [11]. In general, a bubble collapse on a soft sample is expected to cause more pits than on a high-strength material [82]. A good example for this is the first two bubbles that both produced five pits. A link between SCAs in the second collapse can again be found in the areas corresponding to the pitting for the first and the second bubble (corresponding areas marked by the red arrows). However, this correlation seems to be weaker for the soft sample. As we saw for 316L, SCAs could be identified in the two bubbles on aluminum that do not correspond to a pit (e.g., for the first bubble at 350 µs from 12 to 2 o'clock).

The third bubble collapse shows a very interesting phenomenon – this bubble did not cause a pit on the aluminum sample, even though this is a very soft material. This is consistent with the findings described in the previous chapter. Of specific

interest is the collapse at 350 µs. This third bubble did not show an SCA but instead a very symmetric second-collapse toroid. In this series of 100 bubbles, a second instance of such a symmetric toroid without damage was found (images not shown). The occurrence of these events supports the conclusion that there is a link between damage pits and SCAs. This seems to be more important for technical materials than for the soft aluminum. We assume the dynamics of the bubble are unaffected by the differences between the materials, indicating that there are phenomena during the second collapse which might have an effect on soft materials but not on harder material. This could be the reason for different pitting rates found in Section 4.3.

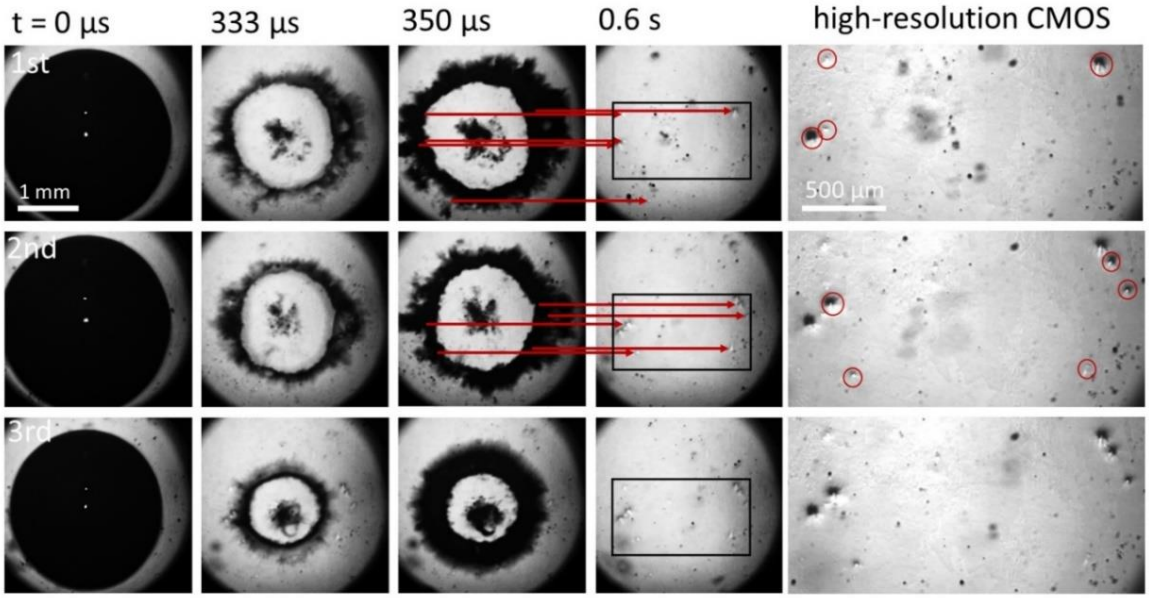

Fig. 36 Top view of the first three bubbles on aluminum and the HR recordings of the surface after the respective collapses. The arrows mark corresponding areas in the images.

While in axisymmetric simulations [2, 93], by definition such asymmetries are not produced, fully three-dimensional simulations that do not enforce symmetry have recently been performed [72]. However, while these simulations in fact do capture that the second collapse is asymmetric, the do not show features particularly similar to the SCAs described here. This may indicate that in the experiment there is some form of local physical trigger that is not present in the simulation.

5.3.3 Material Influence on Pit Shape

In the previous chapter we introduced the pitting rate (the average number of pits per bubble) to quantify one aspect of damage accumulation in single-bubble experiments. The pitting rate depends on the stand-off distance. For instance, in Section 4.3, a change of γ from 1.36 to 1.28 led to a decrease of the pitting rate by 14%. For the three samples discussed in the previous section, the pitting rate at γ of 1.35 +/- 0.05 was 3.2 pits/bubble for aluminum, 0.59 pits/bubble for 316LVM and 0.39 pits/bubble for NAB. Also, the minimum and maximum number of pits after one single bubble varied. For aluminum we found 0 to 6 pits, for 316LVM 0 to 3, and for the NAB 0 to 2 pits after one bubble, consistent with what was presented in the previous chapter [82]. One limitation in this evaluation is that no distinction is made between different kinds of pits. Since the size of the pits might have an important role in the wear process, further analysis is needed. To this end, Fig. 37 shows confocal microscope images of representative pits for γ = 1.4 on the three tested materials. The regions were selected such that individual pits are still clearly distinguishable. Fig. 37 shows significant differences in depth and size of the pits. Also, the pits on one single sample varied. This difference in size and depth of pits on one material is the greatest for aluminum and the least for the NAB. Here, the maximum depth was taken as a reference value. The aluminum surface had a maximum pit depth of 6 µm, whereas 316LVM showed a depth of 200 nm and the NAB 125 nm. These values are ordered inversely to the respective hardness of the materials (expressed in HV 0.05: aluminum, 22 ± 1, 361LVM, 168 ± 6, NAB, 201 ± 6 [82]).

Differences in the effect of the pit-surrounding microstructure are visible in Fig. 37. Grain boundaries emerged on the aluminum (Fig. 37a, black box). Surface changes are seen around the pits on the 316LVM (Fig. 37b, black box) that may be light slip lines which are a typical feature of the later damage stages of the 316LVM [78]. Surface changes that go beyond single pits did not become visible on the NAB. Other cavitation erosion experiments with higher bubble numbers [78, 82] show that the pits, which probably did not lead to material loss, caused a lateral shift of the material. Grain and twin boundaries are a key factor in material removal [78, 89]. Hence, while the formation of cavitation damage is dependent on the hardness of the tested material, the microstructure has also a significant impact.

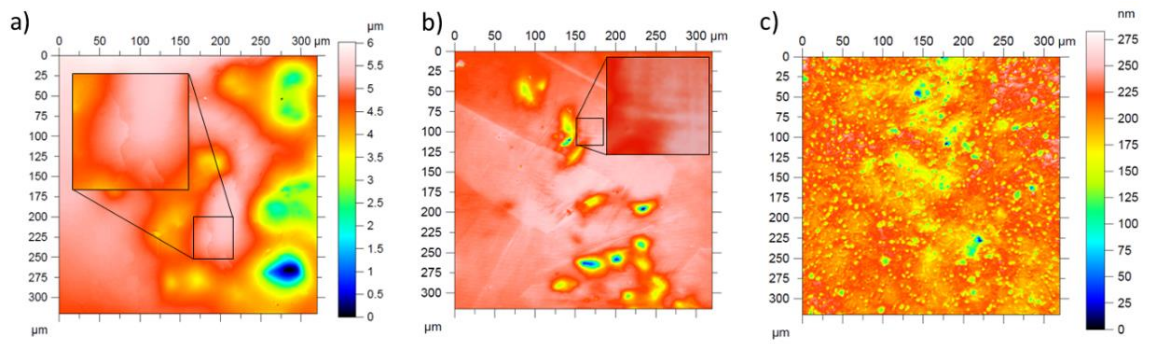

Fig. 37 Confocal surface topography images of pits on a) aluminum (100 bubbles), b) 316LVM (500 bubbles), c) NAB (500 bubbles). Note that b) and c) are on the same depth scale, while a) is on a different, coarser one.

5.3.4 Small Dissolved-Gas Bubbles and Shockwave-Induced Bubble Collapse

Further indications of how the damage may occur were found in a different experiment with a bubble with γ of 0.8. This was the first bubble of a series, impacting on a freshly polished surface, free of pits. Fig. 38 shows selected images from the side view of the growth and the collapse of this cavitation bubble. Additionally, two top-view images are shown – one image of the surface before the plasma breakdown and one image of the surface just before the first bubble collapse. The top view image at 216 µs shows a pit (red circle). The small arrows mark the same position in the side view image and the large arrow connects corresponding areas in both top view images. In this experiment a small pre-existing bubble of about 90 µm diameter happened to be attached to the surface below the induced cavitation bubble. A collapse of the small bubble is captured at t = - 150 µm. The small bubble grew to twice of its initial diameter during the following growth of the main, laser-induced bubble (-100 µs, 0 µs). Both bubbles do not merge in this process. Just before the first collapse of the main cavitation bubble, in the top view at 216 µs a pit becomes visible at the initial position of the small bubble. Plasma breakdowns produce a shockwave [29, 94]. We think that due to this pressure wave the small bubble was induced to collapse on the surface. There is no phenomenon other than the plasma shock wave that could induce the collapse of the small bubble at this stage, before the first collapse of the laser-induced bubble. Therefore, the pit appears to be induced by the interaction of the

small bubble and the shockwave of the laser breakdown. Typically, this phenomenon would not occur due to the fact that bubbles of this size did not attach to the surface. Also, in the experiments with γ = 1.35 the plasma breakdown is further away from the surface.

Nevertheless, apparently pressure fluctuation can induce bubble collapses close to the solid surface that can produce pits. Shock and pressure waves are produced at several stages during the bubble collapses [11, 95]. Their effect on small bubbles is thought to be less at greater distance. Therefore, especially the collapse of cavitation bubbles close to the solid surface may induce breakdowns of small bubbles. The SCAs in the bubble dynamics (Fig. 34, Fig. 35 and Fig. 36) might be the regions with the highest-pressure fluctuations and may preferentially induce such collapses.

The second phenomenon that might be important for pitting is the effect of the bubble growth of the laser-induced bubble on the small one. In real applications, water always contains non-condensable gases dissolved in the fluid [96, 97]. The rebound of the main bubble on the sample surface (Fig. 32 at 232 µs) could grow small bubbles that in the following second collapse (Fig. 32 at 300 µs) might be induced to collapse. Philipp and Lauterborn [11] as well as Supponen et al. [95] showed that several shockwaves could be produced during the second, torus-shaped collapse of cavitation bubbles.

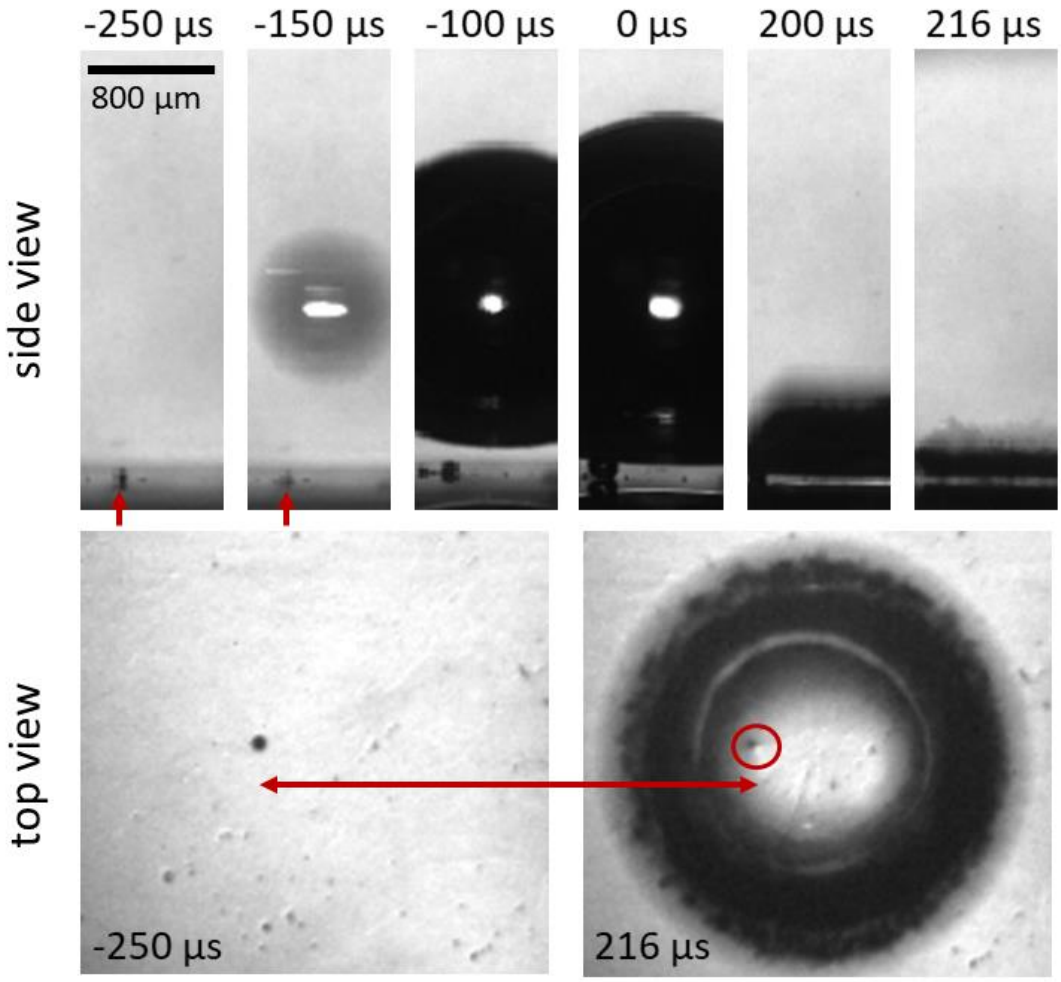

Fig. 38 Growth and collapse of a cavitation bubble with $\gamma = 0.8$ inducing a secondary bubble collapse on the surface.

5.4 Chapter Conclusion

Pure aluminum, a stainless steel, and a nickel-aluminum bronze were exposed to successive single bubbles induced by a focused laser pulse. We used a three-camera arrangement to obtain more a detailed picture of the cavitation bubble dynamics that then was correlated to an in-situ image of the surface damage taken just after each bubble collapse.

The time course of the damage formation was consistent with the findings of Chapter 4. In particular, it was again found that the first pits form very early, even on high-strength materials. Many, eventually overlapping pits then form a characteristic damage pattern that has the shape of a ring for the non-dimensional stand-off distance γ = 1.35 examined here. The pitting on the different materials

was examined in detail. The question is to what extent the material properties and the bubble dynamics influence the pitting of the surface.

We identified sub-processes in the collapse that appear to play a role in pitting, especially on technical alloys. Strong collapse areas (SCAs) are locally enlarged parts of the second bubble collapse close to the solid surface. The locations of the SCAs showed a high correlation with those of pits. However, not every one of these SCAs led to a pit, leaving the question if there is a further sub-process beside the SCAs. An example was given of a shockwave-induced collapse of a small dissolved-gas bubble attached to the sample surface. This collapse produced a pit similar to the damage found after the second collapse. The poor visual access to the surface sample directly in or under the collapse region hinders conclusive insights. However, in the vicinity of the main bubble collapse, small bubbles may grow during the bubble rebound and may then be induced to collapse by a pressure wave in the second collapse.

For material damage, the number and size of pits that can be caused by a bubble are relevant. Here, the pitting rate was found consistent with the findings in the previous chapter. Additionally, the pits were analyzed with a confocal microscope and the material dependence of pitting was investigated. An important factor is the material response to the sum of the pits, which mainly depended on the microstructure. The microstructure and its influence on the later damage stages are discussed more in detail by Lopez et al. [78].

6. Single-Bubble Cavitation Induced Pitting on Technical Alloys

6.1 Chapter Introduction

Since most of the experiments from the two previous chapters were for $\gamma = 1.4$ but the bubble dynamics are very different for different stand-off distances [11], the question arises how generic the findings are. Therefore, we investigated the correlation of bubble dynamics with pit occurrence for the entire range of stand-off distances that our experiment can usefully produce, $\gamma = 0.3$ to $\gamma = 2.15$. In the course of the investigation a few other aspects were seen to be relevant and are thus covered here, namely, local and global collapse asymmetry, a visualization of shockwaves, and an initial investigation into the scaling of the initial damage evolution with the absolute bubble diameter. As before, the experiments were performed mainly on 316L, but differences and similarities compared to NAB and aluminum were also investigated.

Most of this chapter has been published in Kühlmann and Kaiser [60].

6.2 Methods and Materials

The experiment has been described in detail in previous chapters (Section 4.2 and 5.2). Here, a brief summary is given, and new features are described. Fig. 39 shows a simplified view of the illumination and image detection. The cavitation bubbles were generated by a focused 10-nanosecond laser pulse (1064 nm) above the center of the polished cylindrical samples. The repetition rate of the laser pulses, and thus the bubbles, were varied between 15 Hz and 0.5 Hz. For both the pit-bubble correlation experiments and the pitting-rate experiments, a low repetition rate was preferred because longer intervals between bubbles mean less residual gas from the previous collapse that complicates imaging the surface. For experiments with many cavitation bubbles (more than 1000), the maximum repetition rate was chosen to reduce the duration of the experiment.

The bubble dynamics are recorded simultaneously with two high-speed cameras. In addition, the surface of the sample was recorded before and after each bubble. The high-speed cameras (Phantom Veo 710L, Phantom v1216, and/or Photron SA-Z) were operated at repetition rates adapted to the relevant part of the bubble

dynamics (between 60 kHz and 160 kHz). A camera with low framerate but higher resolution allowed examining the surface *in situ* via reflected-light microscopy. Two beam splitters are utilized in the optical train of the light microscope. A 50:50 splitter directs the illuminating LED light towards the sample, while a second 90:10 splitter projects the image onto two cameras. The majority of the light (90%) is directed towards the high-speed camera. The exposure time of the high-speed camera for the side view was set to 5 µs. For most of the experiments, the camera for the top view was operated at about 10 µs. For some experiments (e.g., Fig. 48a) it was 5 µs. The high-resolution camera was exposed for 3000 µs. The circular field of view varied between 3 mm and 1 mm in diameter, depending on the radius and stand-off distance of the bubble. For most experiments, the LED illumination was continuous, but to visualize shock waves, the LED was pulsed with 200 ns pulse duration.

The cylindrical specimens, 12 mm in diameter and 7 mm in height, were first ground, and in the final preparation step the sample was lightly etched to visualize grains [78, 82]. Most of the experiments were performed on the stainless steel 316L, but differences and similarities compared to a nickel-aluminum bronze (NAB) and pure aluminum were also investigated. In typical ultrasonic cavitation *erosion* testing, aluminum shows very little cavitation resistance, 316L much more, and the NAB is most resistant. More detailed material specifications and material properties can be found in [3, 78, 82].

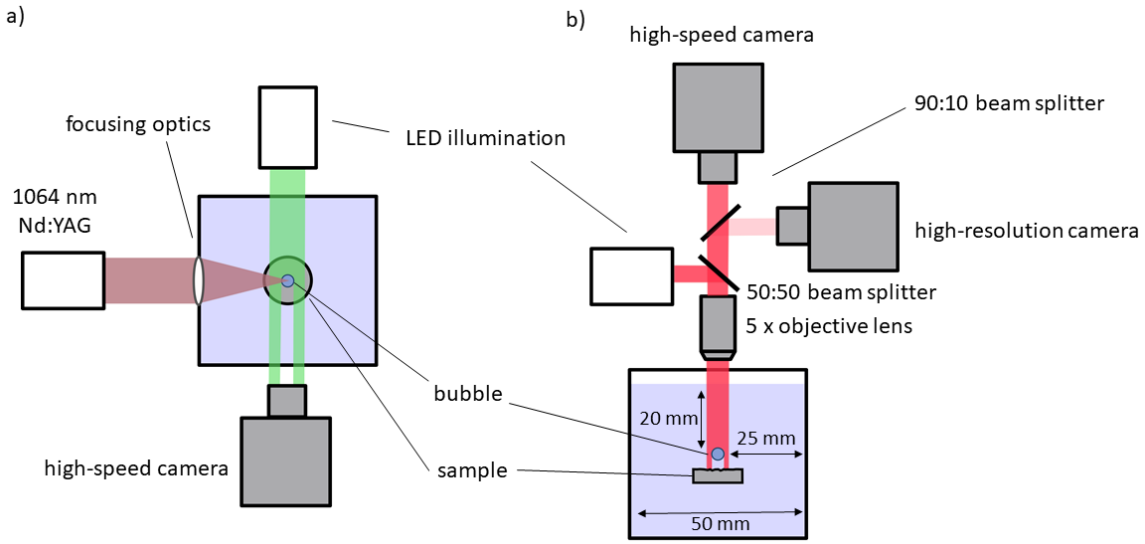

Fig. 39 Experimental setup a) from the top and b) from the side.

6.3 Results and Discussion

6.3.1 Pitting Damage Patterns

Fig. 40 shows the regions in which successive bubble collapses caused damage in form of pits at stand-off distances from 0.25 – 1.90. The in-situ images were selected so that the damaged region and individual pits are clearly visible. For $\gamma = 0.25$ (Fig. 40a), the pits form a ring with two regions along the laser beam propagation axis where the damage is significantly increased. The damage in these regions is composed of multiple pits. For $\gamma = 0.9$, two regions away from the laser axis contain the majority of the pits. For a stand-off distance of 1.0, pits occur in a much smaller region that is elliptical with the long axis perpendicular to the laser direction. For $\gamma = 1.2$, a circular damage pattern can be seen with more damage along the laser axis, although the damage is more pronounced towards the laser incidence. A similar damage pattern is observed for $\gamma = 1.36$, except that the circle is significantly larger. At $\gamma = 1.55$, the pits occur in a ring similar to $\gamma = 1.36$, but an additional circle of pits formed around the center of this ring. At a stand-off distance of 1.78, only one circle of pits is seen directly below the center of the bubble. Finally, Fig. 40a shows damage at the upper end of the stand-off distances that cause pits. Here, at $\gamma = 1.9$, pitting occurred only in a relatively limited area, again directly below the bubble center.

The number of bubbles that must collapse on the surface to produce significant damage patterns varied widely, i.e., from 100 ($\gamma = 0.25$) to 200 000 ($\gamma = 0.9$). The damage patterns in Fig. 40 are consistent with recordings of equivalent experiments on aluminum by P&L1998 [11] and Issilin et al. [12]. This is also true for the asymmetries typical of laser-induced single bubbles [29, 49, 85]. These asymmetries in the likelihood of a pit occurring in a particular spot are probably caused by the asymmetry of the plasma. However, the ring-shaped patterns (e.g., at $\gamma = 1.36$) show that this asymmetry seen in damage patterns is not universal and pits can occur everywhere along the ring.

Fig. 40b shows sub-regions of the damage shown in Fig. 40a with all images on the same spatial scale. This type of presentation facilitates a comparison of the lateral dimensions of pits. For all $\gamma > 0.3$ the pits are quite similar in size. This is

true for both pits at a fixed distance as well as for pits across different stand-off distances. This may imply that the surface loading by the fluid dynamics is not so different across these cases, which in turn points towards the mechanism in the flow being similar. For $\gamma = 0.25$, however, the pits look distinctly different. The special nature of very small stand-off distances with $\gamma < 0.3$ has recently been highlighted by Reuter et al. [81] who identified a self-focusing mechanism of the shockwaves that leads to strong deformation of the material. This might be the cause of the more pronounced damage region on the laser axis in Fig. 40b. This region is also composed of multiple pits that occurred in a small area. Note that the images shown in Fig. 40 for $\gamma = 0.25$ are at a lower number of bubbles than the other images.

Up to bubble counts of several 10 000 (depending on γ), pitting is the only damage observed on 316L. As shown in a previous study, before material is lost in cavitation erosion, plastic deformation leads to material elevation and a rise of the grain boundaries [78]. Therefore, if these phenomena have not yet occurred, there cannot be material loss, as shown in Fig. 40 where none of the sample shows significant change of the material structure at the grain boundaries. How the accumulation of pits finally leads to erosion depends on the material [78], and the pitting rate was also found to be material-dependent [82]. For 316L and aluminum after many pits plastic flow occurs. Grain boundaries stop this flow and this is where the first material removal (erosion) was observed [78]. For NAB, plastic flow on a large scale was hindered by the disperse intermetallic particles. Nevertheless, the first material removal occurred at grain boundaries [78]. In the current work, pits were found for every material and stand-off distance investigated up to an upper boundary discussed in the Section 6.3.7. Thus, any damage due to multiple bubbles at a given stand-off distance for which pits occur has the potential to eventually lead to material loss due to the plastic flow as summarized above [78].

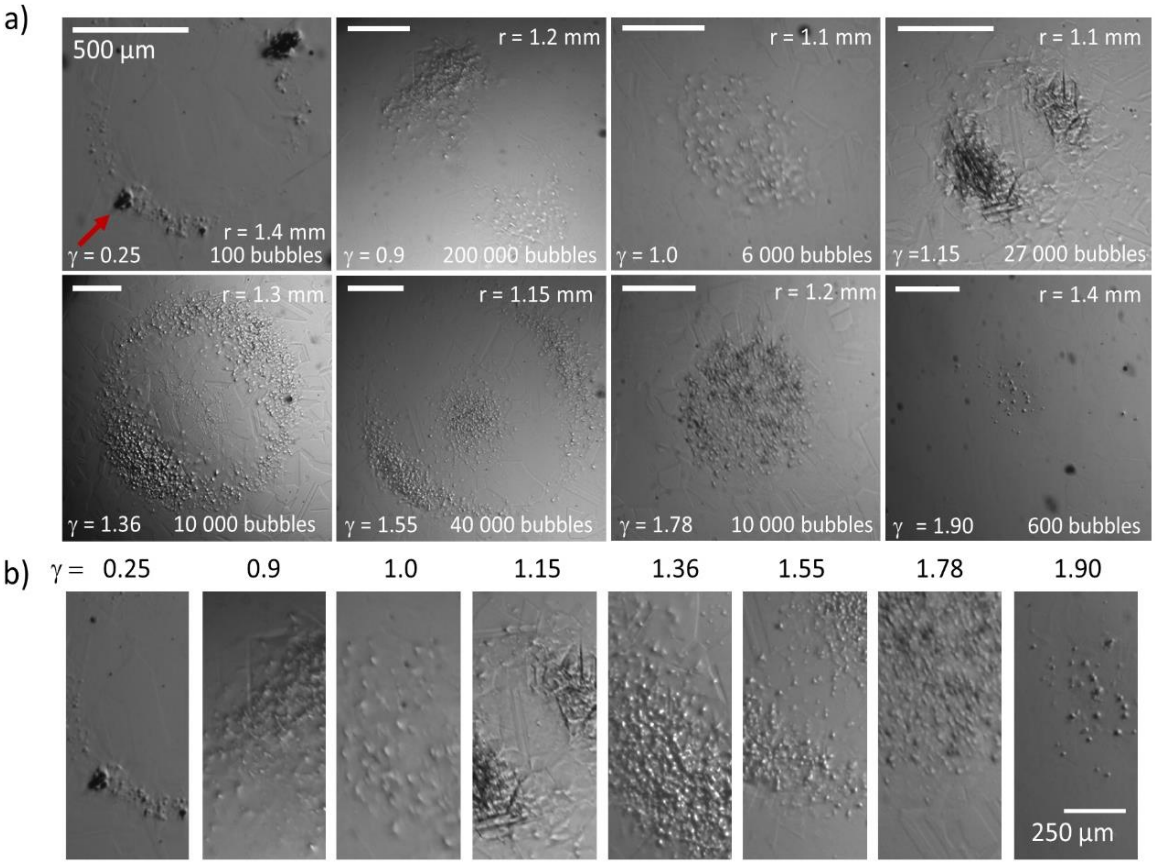

Fig. 40 In-situ images of pits at various stand-off distances for a bubble radius of about 1.2 mm. The stand-off distance, number of bubbles, and the exact radius are given in each image. The laser is incident from the bottom left corner (red arrow). a) Overview images showing the entire damaged area. The images are shown at different magnifications. Each scale bar corresponds to 500 µm b) Sub-regions of the images in (a) at higher magnification. Here, each image has the same magnification, represented by the 250 µm bar.

6.3.2 Correlation of Damage and Bubble Dynamics

The surface changes are now correlated with the corresponding bubble collapse. The method for that was presented in detail in our previous chapter and is summarized in Fig. 41. For this evaluation images from the beginning of a bubble series when only a few pits have formed, were used (unlike the examples in Fig. 40 where pits overlap, making counting impossible). First, a pit was searched for in the high-resolution images before and after the bubble collapse. If a pit was found, its location was identified in the high-speed data and these were examined in more detail. Fig. 41a and Fig. 41b show the surface before and after the collapse. The pit is marked with a red circle. Fig. 41c and 3d show selected images from the second collapse of the bubble. The position of the pit is marked with a red x in

these high-speed images. Here, the pit is located where an SCA was found in the collapse. Previous chapters examined how the phenomena in the second collapse of bubbles with $\gamma = 1.35 \pm 0.05$ are related to the pitting. The same procedure is now applied to stand-off distances from 0.3 to 1.9. The findings are first discussed for $\gamma > 1$, where only the second collapse occurs close to the sample surface, and $\gamma < 1$, where both the first and second collapse occur in direct vicinity of the sample surface.

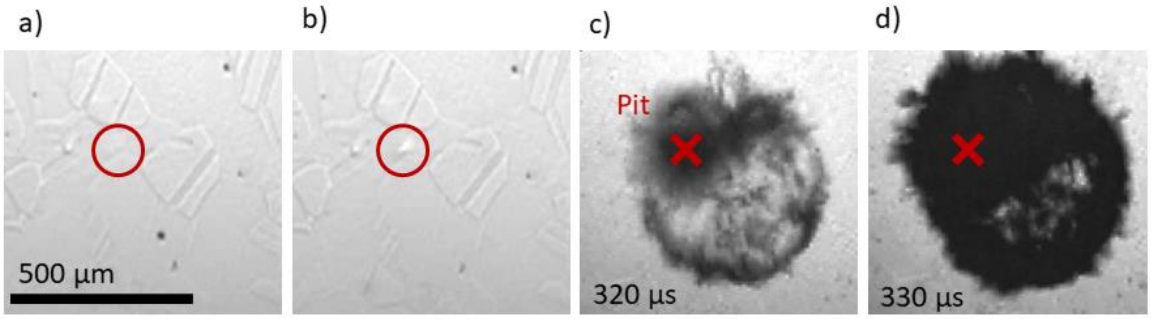

Fig. 41 316L surface a) before and b) after the bubble collapse. c) and d) show the bubble ($\gamma = 1.15$, $r = 1$ mm) around the second collapse on the surface.

6.3.3 $\gamma > 1$

Fig. 42 shows the side view of selected bubble dynamics from $\gamma = 1.1$ to $\gamma = 1.8$ of bubbles at $r = 1.4$ mm. The dynamics of the bubble collapse processes were described in detail in other work [11] and are used here just as a reference for the reader. As can be seen in Fig. 42a-e, at none of these stand-off distances does the first collapse occurs close to the sample surface. Therefore, the second collapse is considered relevant for pitting.

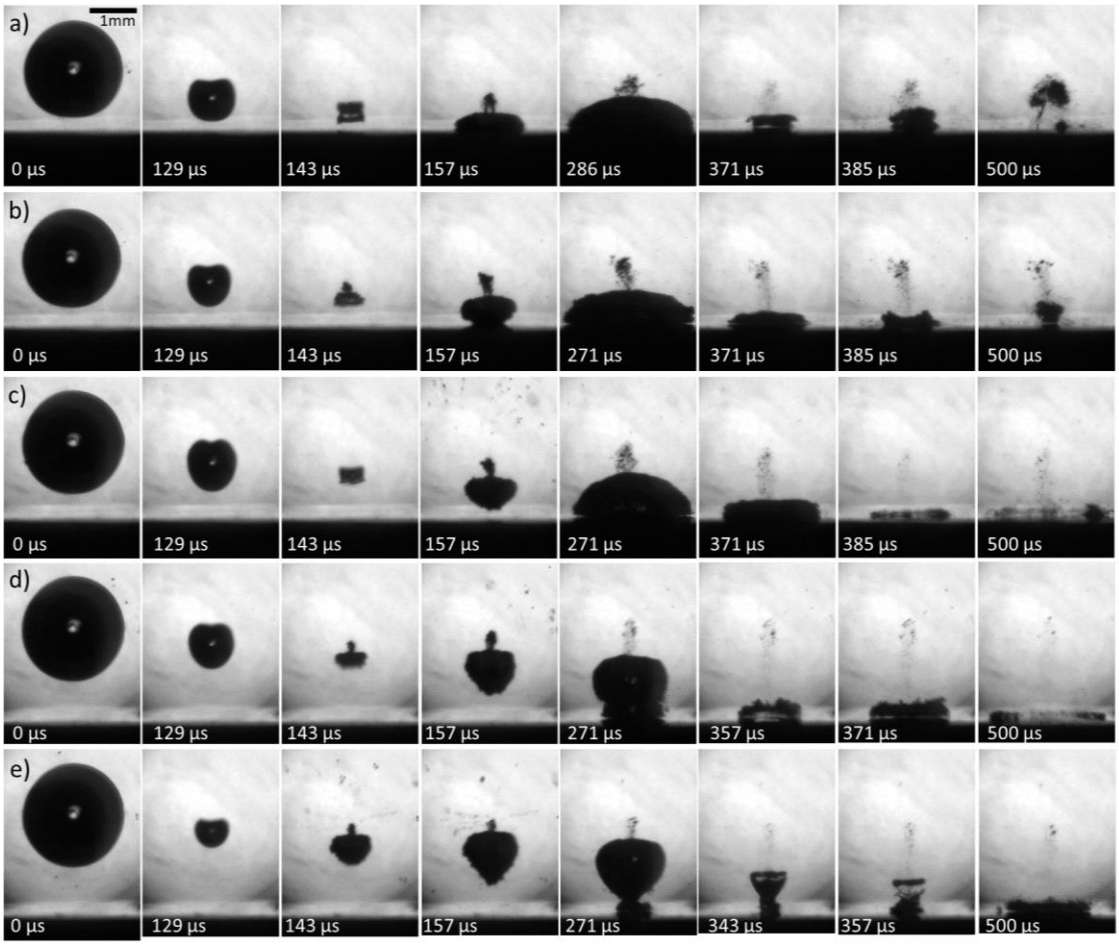

Fig. 42 Selected images from the side view of bubble collapses (r = 1.4 mm) at a) $\gamma = 1.1$, b) $\gamma = 1.25$, c) $\gamma = 1.35$, d $\gamma = 1.6$), e) $\gamma = 1.8$.

Fig. 43 shows the dynamics around the second collapse of the same bubbles as shown in Fig. 42, now in top view. All bubbles shown here caused at least one pit. The position of the pits is marked with a red x. A collapse ring with different radii for different γ can be seen for all stand-off distances. The collapses at γ = 1.25 to 1.8 (Fig. 43c – e) also have a “spot” of gas phase in the center of the ring. A more complete view of the dynamics from the top view can be found in Fig. 52 in Appendix A.1.

In each of the examples shown in Fig. 43, a pit could be assigned to an SCA in the second collapse. In fact, from γ = 1.1 to γ = 1.8 this was the case for thousands of image series we visually examined. Pits usually occur in the center of the SCA. As in the example in Fig. 43b, when two pits occurred, two SCAs are seen. It is not true that each SCA necessarily leads to a pit, but each pit can be attributed to an

SCA. SCAs that did not cause pitting can for example be seen in Fig. 43c and d on the torus opposite of the pitted region (white arrows). In Fig. 43e inward motion blur indicates an SCA that is not on the torus ring but closer to the center. The overall damage patterns in Fig. 40a indeed show that for γ = 1.55 – 1.9 damage occurs more centrally.

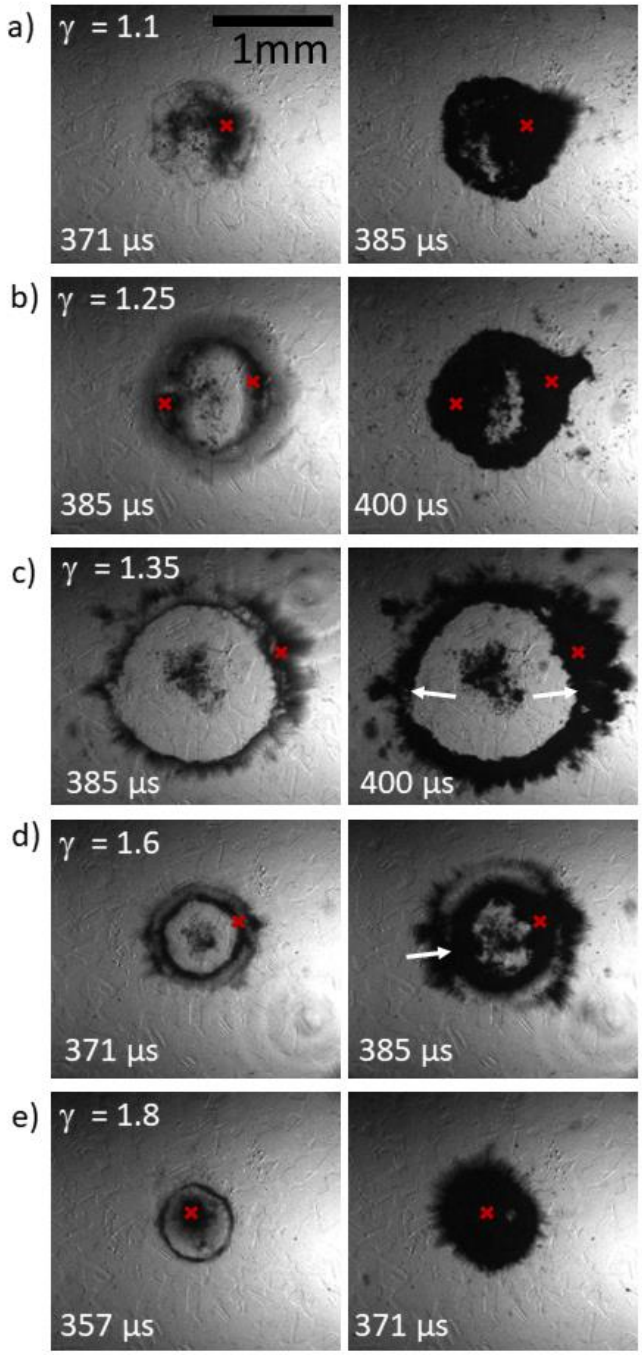

Fig. 43 Two selected images from the top view of the dynamics around the second collapse of the bubbles shown in Fig. 42. Pits are marked with a red x and SCA-like structures that did not cause pits are marked with white arrows.

SCAs can occur in any part of the second collapse. However, the as described in the previous section, the accumulated damage is not axisymmetric. It appears that the asymmetry that is inherent in the experiment caused an asymmetric lateral distribution of the probability of SCA occurrence on the area of the second collapse. We observed that an SCA occurred more often in certain areas, consistent with the asymmetry in the accumulated damage.

6.3.4 $\gamma < 1$

For stand-off distances from 0.25 to 1 both the first and the second collapse occur in the immediate vicinity of the surface. Since from above a pit becomes visible only after the disappearance of the gas phase and thus after the final collapse of the bubble, pits could not be easily as attributed to the second collapse as for $\gamma > 1$. Thus, we need to examine the bubble dynamics in more detail here.

Fig. 44 shows the first and second collapse of bubbles with $\gamma < 1$. Each of these bubbles caused at least one pit whose location is marked with a red x. The first collapse is always toroidal with a high degree of symmetry, whereas the second collapse is strongly asymmetric, with SCAs so pronounced that only a faintly toroidal shape can be seen. For $\gamma = 0.25$, the first-collapse toroid is elliptical and has two SCAs, and the second collapse occurs entirely in two distinct SCAs away from the laser axis. In all cases, the pits are found where SCAs appeared. For $\gamma = 0.66$ to 0.95 (Fig. 44 a - d), the pits are located in the center of the SCAs in the second collapse - just as for the larger distances discussed in the previous section. For $\gamma = 0.4$ this is approximately so, but for $\gamma = 0.25$ (Fig. 44e, f), one of the two pits is adjacent to the SCA. From all these observations, and considering that for $\gamma > 0.5$ Reuter and Kaiser showed that during the first collapse there is always a water layer of at least 5 µm thickness between bubble and solid [59], we conclude that for our millimeter-sized bubbles the second collapse is responsible for pitting for $\gamma > 0.4$. For $\gamma = 0.4$ and 0.25 the first collapse may already cause damage. As discussed in the Section 6.3.1, this is consistent with the recent work of Reuter et al. in which for $\gamma = 0.3$ and less a very damaging shock wave self-focusing mechanism occurred during the first collapse [81].

In other works, the liquid jet associated with the first collapse was seen as at least partly responsible for the pitting, especially at small stand-off distances [11, 80]. However, these findings came from soft materials. On 316L, even at small stand-off distances and high bubble counts (Fig. 40, γ = 0.9, 200 000 bubbles), no surface changes were observed that could be attributed to the central jet, consistent with Reuter et al. [30]. Such damage should be seen in the area that is below the center of the first ring collapse in Fig. 44. The most likely explanation is that the load on the surface caused by the jet is not sufficient for pitting in technical alloys. Instead, here, SCAs in the second or first collapse are responsible for pitting.

Results for the other technical alloy tested here, NAB, can be found in the Appendix in Fig. 53 and Fig. 54. The findings are similar, which confirms that the fluid dynamics of the bubble is decisive for damage in the form of pits on the surface where SCAs occur in the second collapse. In the Sections 6.3.7and 6.3.8, we will compare 316L and NAB in in terms of the pitting rate and the accumulated damage of many pits.

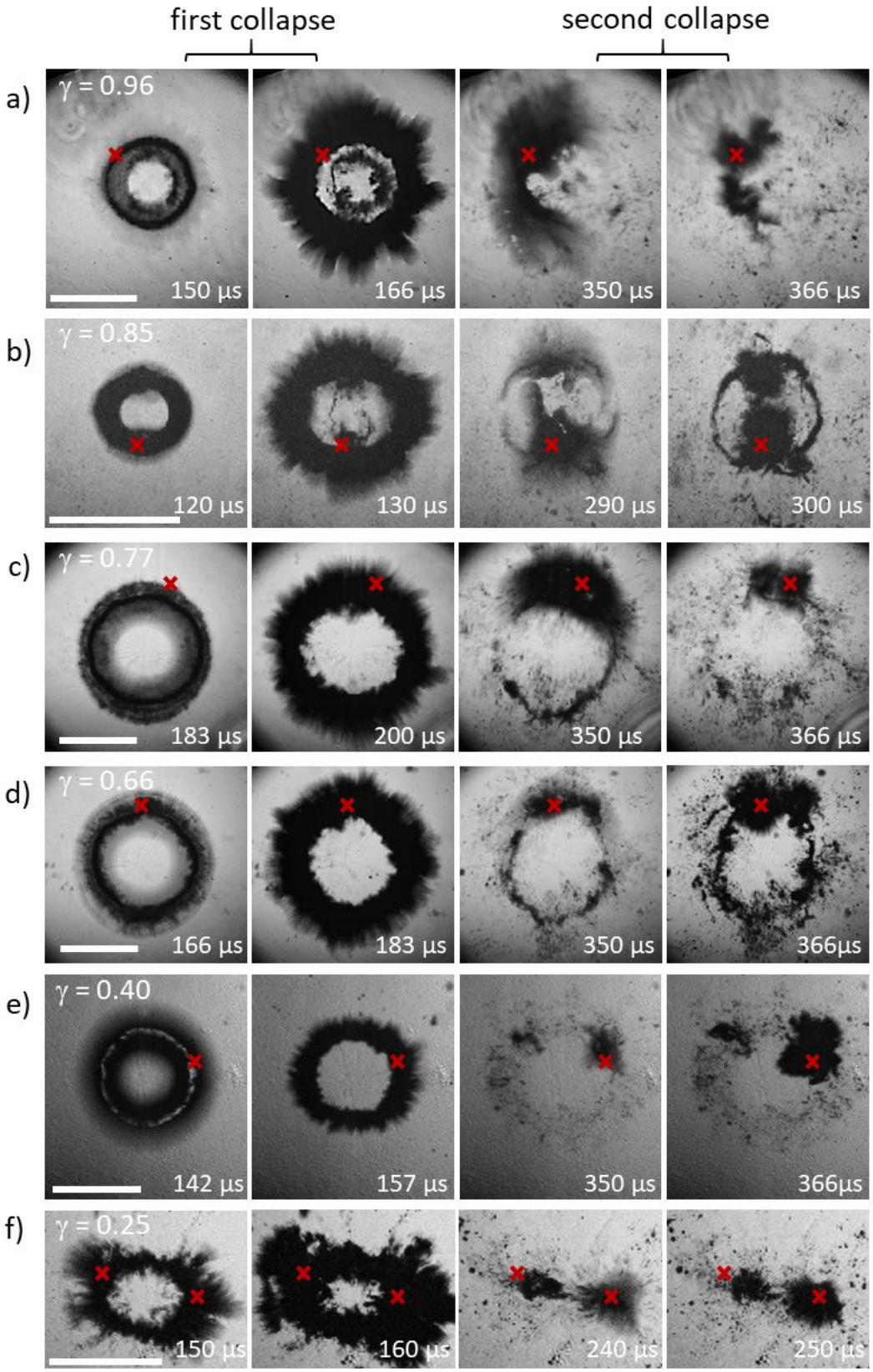

Fig. 44 Selected frames at the first and the second collaps. The ringed-shaped features on the upper left of a) and bottom right on c) are waves on the free top surface of the water in the cuvette that do not influence the bubble.

6.3.5 SCA and Shock Wave

It is known that during the several rebounds of the bubble shock waves are emitted at the minimum presence of gas in liquid, i.e., at each collapse [11, 29, 54, 95]. Based on the results presented in the previous section, shock waves in the second collapse are of particular interest. Our experiment with its limited frame rate is not as suitable for visualizing shock waves as the more purpose-built experiments with ultra-high frame rates, e.g. [11, 81]. Nevertheless, by reducing the illumination duration of each frame to 200 ns, we did indeed capture shock waves.

Fig. 45 shows the second collapse from the side (Fig. 45a) and from the top (Fig. 45b), as well as the sample surface just before and after this collapse. In the side view of the collapse, in addition to the collapse ring itself, two other features can be observed. One is that the bubble torus is detached from the surface (Fig. 45a white arrow. Fig. 55 in the Appendix includes a second example in which this detachment is clearer [but the shockwave is less clear]. The supplementary material includes the two corresponding video sequences). The vertical distance between the gas-phase shadow and its reflection on the sample surface indicates that the distance between gas phase and sample surface is several tens of micrometers. In none of the about 300 bubbles recorded with the shorter, 200-ns illumination did the damage occur in the region exhibiting this vertical detachment. The detachment was also found by Reuter et al. for a similar γ [81]. The second feature is a shock wave with its center at the torus of the second collapse on the side of the laser incidence. There is some spatial uncertainty, but combined the side and top view indicate that this shock wave was apparently emitted by the very SCA that is associated with the pit found after the bubble. Since the energy per unit area of a spherically propagating shock wave decreases with the square of the distance from the origin, only locations on the sample surface close to the origin are affected. The emission of shock waves from such an asymmetric region of the torus was already found by P&L 1998 [11] but now can be associated with the formation of a single, specific pit.

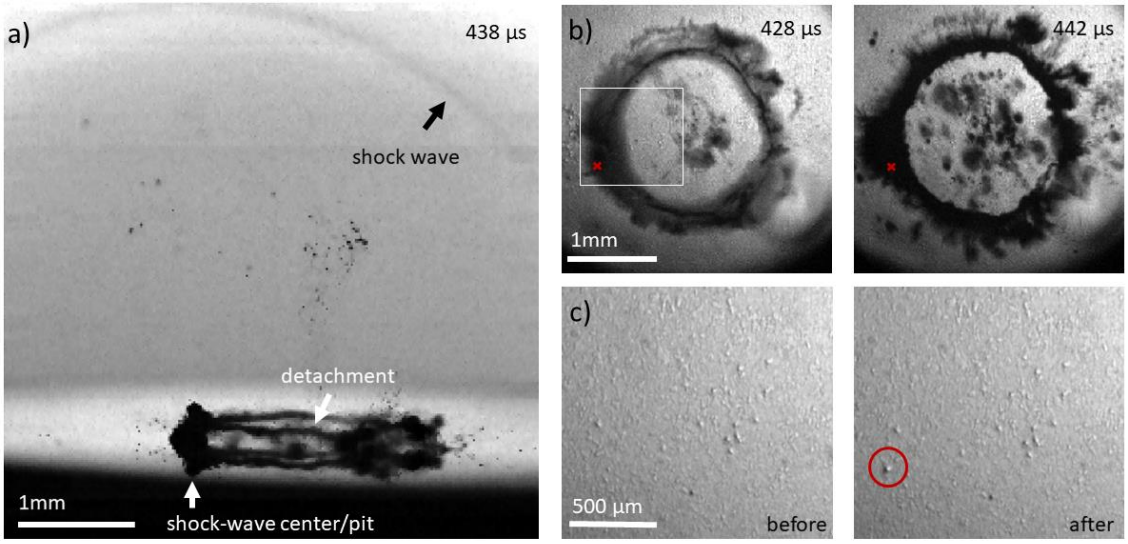

Fig. 45 Second collapse of a bubble with $\gamma = 1.4$. a) side view, b) top view close to and after the collapse, c) detail [corresponding to the white rectangle in sub-figure (b)] of the surface before and after the bubble. The resulting pit is marked with a red circle; the pit location is marked with a red x in the high-speed images in b). Note that the sample shown here had previously been subjected to bubbles of various stand-off distances, which is where we cannot see a simple and regular pit pattern as in, e.g., Fig. 40.

6.3.6 Controlled Asymmetry

The damage of the sample surface is related to asymmetries in the collapse that in turn stem from asymmetry in the experiment, i.e., in the laser-induced plasma. Since we could not eliminate these asymmetries, we instead introduced further, controlled ones. To that end, bubbles were created near the edge of the sample. The presence of the edge has a strong influence on the bubble dynamics that are globally described by the Kelvin impulse [56]. Fig. 46 shows the dynamics of such a bubble from the side. Even before the first collapse (126 µs), the bubble shrinks faster on the side closer to the edge, and it moves away from the edge of the sample. From 308 µs to 364 µs we see that the collapse does not occur simultaneously. Rather, the region closest to the edge collapses first, and that farthest away last. Fig. 47 shows this process again from above. Both the top view and the side view show that the second collapse of the bubble at 364 µs occurs in a limited area and is shifted towards the sample center. In this area an SCA can be observed. This is also the area where this bubble caused damage, as marked

in Fig. 47 at 364 µs. In repeated bubbles as in Fig. 46 and Fig. 47, no pit or SCA occurred in any other location. Thus, it is reasonable to conclude that SCAs are related to the fact that the bubble does not collapse simultaneously everywhere. Although the externally introduced asymmetry clearly had an effect on *where* a pit forms, even this strong asymmetry did *not* cause pits to occur *more frequently* than in comparable experiments in the center of the sample – in both cases the pitting rate (discussed in more detail below) was about 0.085 pits per bubble for the given material, stand-off distance, and bubble radius.

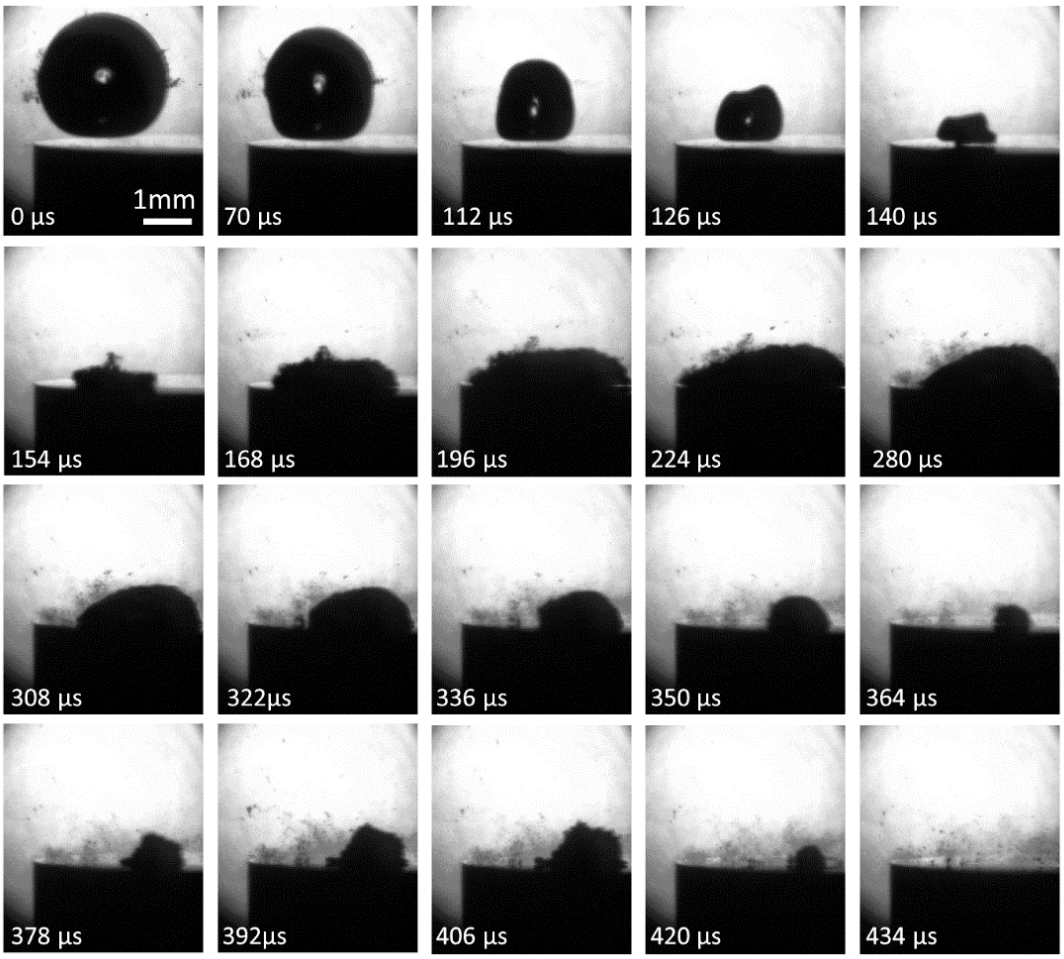

Fig. 46 Side view of a bubble dynamics of a collaps near the edge of the sample

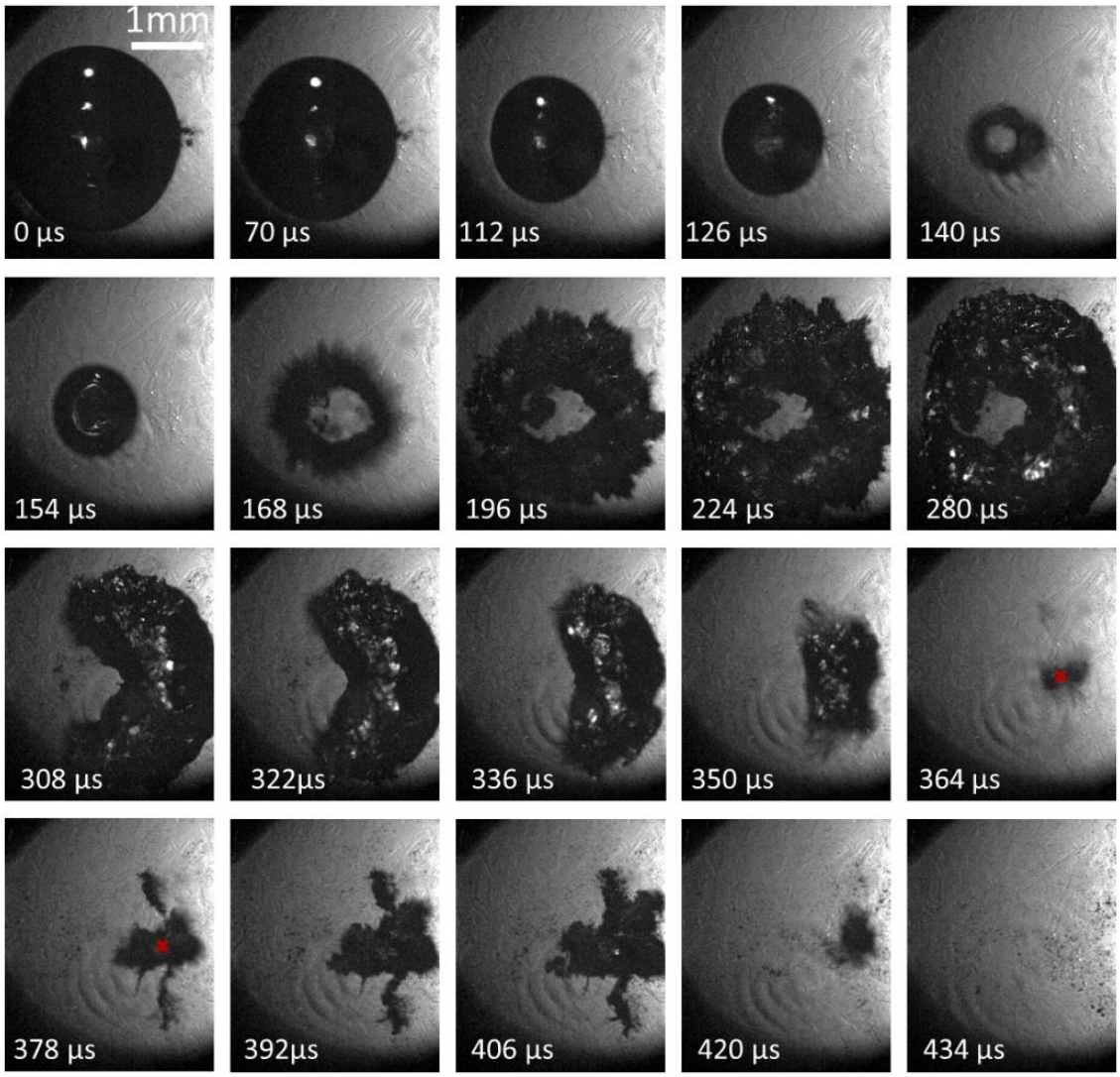

Fig. 47 Top view of the bubble dynamics of the collapse from Fig. 46. The pit is marked with a red x The edge of the sample is on the left.

Fig. 48 shows three bubbles with different stand-off distances shortly before and at the second collapse. These bubbles were induced above the sample center. All bubbles caused a pit that could be linked to an SCA. Fig. 48a shows only a part of the toroidal collapse from the case with γ = 1.4. It can be seen that the ring section does not narrow uniformly (- 13 µs, -6 µs, 0 µs). Instead, shrinkage is slowest in the region where the SCA occurs and the pit is formed. In Fig. 48b and c, two bubble collapses are shown where this phenomenon can be seen even earlier before the second collapse (Fig. 48b: t = - 28 µs, Fig. 48c: t = - 33 µs). The non-simultaneous shrinking process of these bubbles and the coincidence with SCAs indicates that even in bubbles where a strong asymmetry is not intentionally

introduced (as in Fig. 47), SCAs and thus pits, are connected to the temporal non-uniformity of the collapse of the bubble. These findings are consistent with the “energy focusing” seen by Reuter et al. [81] (there, Appendix H). In particular, their subsonic energy focusing in the second collapse is consistent with our findings concerning the likely effect of the second collapse being non-simultaneous [81].

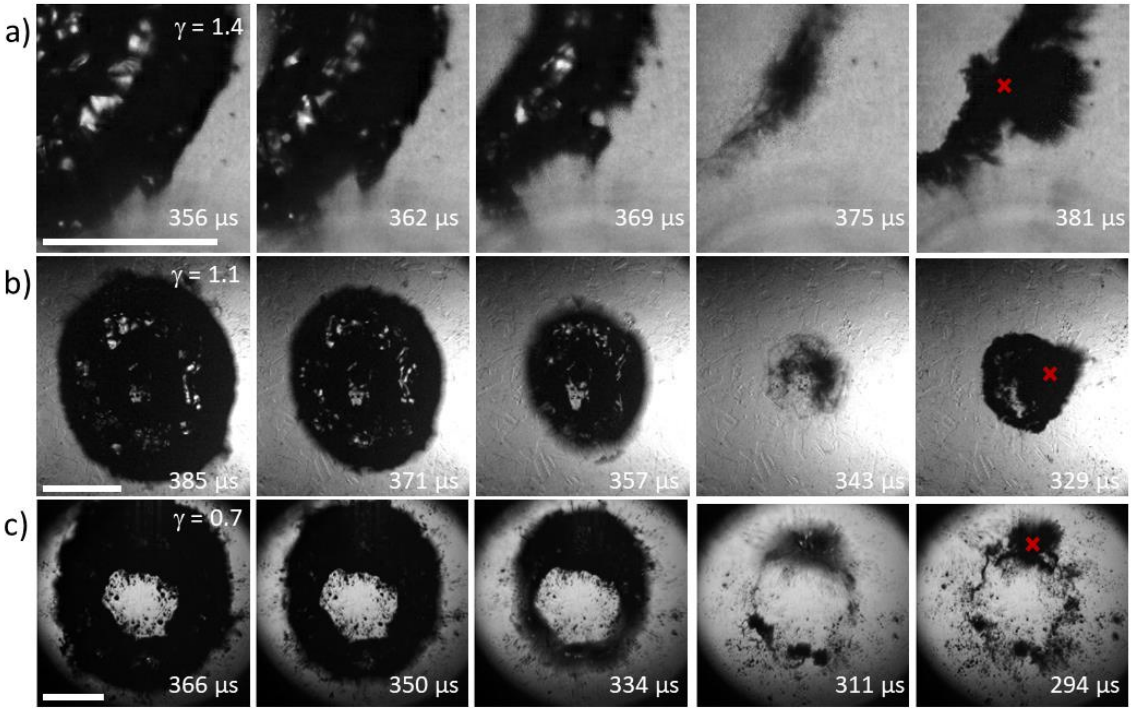

Fig. 48 Three bubble shortly before and at the second collapses a) $\gamma = 1.4$ b) $\gamma = 1.1$ b) $\gamma = 0.7$. Pits are marked with a red x.

6.3.7 Pitting Rate

The pitting rate is a metric of how fast early cavitation damage is developing [82, 98]. In our experiments, in the high-resolution image after each bubble the new pits that stem from that bubble can be identified and counted. Some bubbles do not leave any pits while others create several [82]. This method can be applied until pits start to overlap, which was generally after 50 to 100 bubbles. The pitting rate is then defined as the average number of pits per bubble over this image series [82]. Here, we will discuss the pitting rate on 316L for various stand-off distances and bubble sizes.

Fig. 49a shows the pitting rate at a fixed stand-off distance of $\gamma = 1.40 \pm 0.05$. The maximum range in bubble size usefully attainable with the experiment was from 0.75 mm to 1.5 mm radius. The error bar in radius represents the standard deviation of the maximum radius of each experiment. This variation may stem from the uncertainty in the experimental parameters. Also, since the occurrence of pits is partially stochastic, for a finite number of bubbles the pitting rate determined from two bubble series can differ for the exact same experimental parameters.

Fig. 49a shows that the pitting rate decreases with decreasing radius. The data suggest a linear trend and the corresponding linear fit has a slope of 0.55 pits/(bubble*mm). The fit reaches zero pitting rate at a finite radius of r = 0.4 mm, suggesting that below that lower limit, the maximum load exerted by the bubble collapse is no longer sufficient for plastic deformation of the sample. Accordingly, this limit should be material-dependent. In the previous chapters we performed quantitative surface elevation measurements with a confocal scanning microscope. This showed the pits on the NAB to be smaller than on 316L (about 10 vs 25 μm, respectively), and we still easily see the former in the in-situ images, and they in fact appear smaller. This indicates that we are not systematically underestimating the pitting rate for the smaller of the bubbles in the investigated range. However, we currently have no experimental evidence for what happens with bubbles smaller than 0.75 mm radius. The further regression of the pitting rate towards zero may not be linear.

Isselin et al. found that the shockwave pressure emitted by the *first* collapse increases linearly with the maximum bubble radius [12]. Unfortunately, they did not investigate the *second* collapse, which we have seen to be more relevant for the sample damage. Nevertheless, the consistency of that scaling with Fig. 49a lends some support to the idea that the pits are directly caused by shock wave emission close to the surface.

The influence of γ on the pitting rate is shown in Fig. 49b. The radius of the bubbles was $r = 1.3 \pm 0.2$ mm for 316L. The variation in radius is included in the error, which from Fig. 49a is estimated to be about 10%. At $\gamma = 2.15$, 500 bubbles did not generate a pit, i.e., the pitting rate is less than 0.004 pits per bubble, which we considered essentially zero for current purposes. Towards small stand-off-distances, the pitting rate increases and peaks at about $\gamma = 1.4$, decreasing again

with decreasing stand-off distance to less than 0.1 pits/bubble at $\gamma = 1$. For $0.4 < \gamma < 1$ the pitting rate remains below 0.7 pits/bubble. The steep increase for $\gamma = 0.3$ to over 0.6 pits/bubble again points to a different mechanism at work for these small standoff distances [81]. An obvious outlier in the otherwise relatively smooth relation of pitting rate vs. standoff distance is $\gamma = 1.75$, with 0.425 pits/bubble. This might be explained by the sudden change in area onto which the bubble collapses at $\gamma = 1.75$. As the stand-off distance is increased from 1.55 to 1.75, the area on the sample that the bubble collapses onto significantly changes, its shape being a large ring for the former but a solid circle for the latter (Fig. 40 f and g). For $\gamma > 1.75$ we suggest that with increasing γ less and less energy is reaching the sample surface and an SCA creating a load sufficient for plastic deformation becomes less likely. In addition to the data from 316L, Fig. 49b shows the pitting rate on NAB. The general trend corresponds to that on 316L, with the absolute pitting rate being lower for most γ. For $\gamma = 0.5$ and $\gamma = 0.76$ the pitting rate is slightly higher than on 316L. Most likely this is because the bubble radius was about 10% larger in these two measurements. The upper boundary for pit occurrence was not significantly different on NAB.

P&L 1998 report two series of measurements on aluminum in the range $0.3 < \gamma < 2.15$, examining the depth of the pits [11] (Figures 20 there). The data of this measurement series is also plotted in Fig. 49b. Despite the different material, that metric yields a graph that is similar to our pitting-rate data on 316L and NAB. This similarity may imply that both the depth of the pits and the probability of a pitting event are proportional to the load on the surface. In contrast to the pitting rate that is the average over multiple bubbles on the same sample, the pit depth data, each stemming from a single bubble, scatters more. The upper boundary of detectable pit depth in P&L 1998 on aluminum was similar to the boundary for our pitting rate on 316L and NAB. Recently, also in laser single bubble experiments, Abedini et al. estimated the damage to the oxidic surface layer on an aluminum sample from time integration of the measured transient electric current [99]. Consistent with the trends here, they found that the greatest damage occurred at $\gamma = 0.3$ and $\gamma = 1.4$.

a)

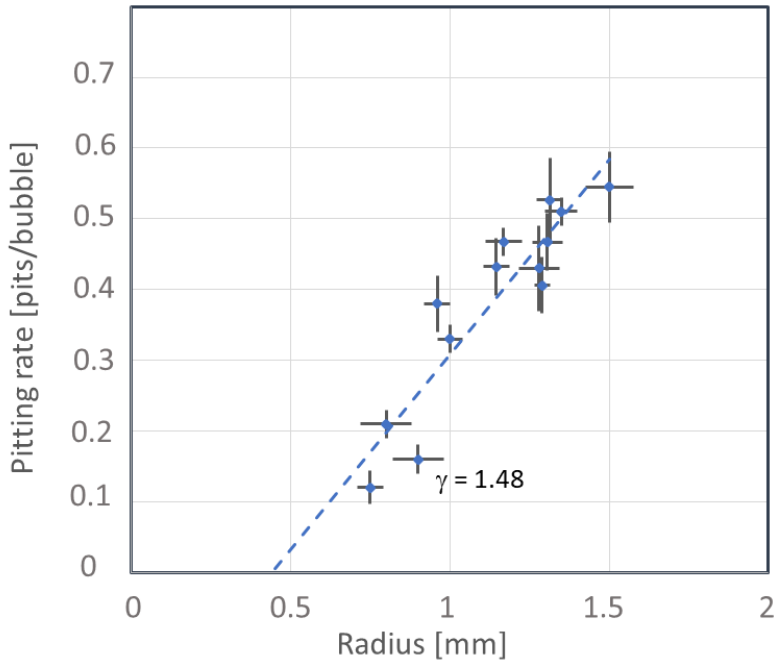

b)

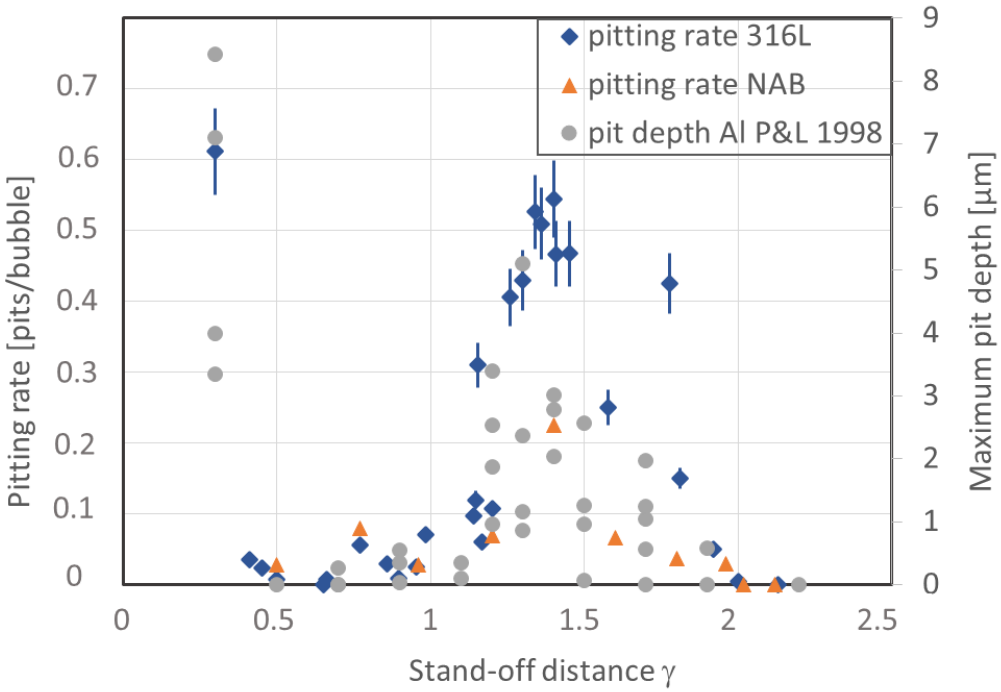

Fig. 49 a) Pitting rate versus radius at $\gamma = 1.40 \pm 0.05$. The data at r = 0.84 mm was taken at a slightly larger stand-off distance, $\gamma = 1.48$, b) pitting rate vs. γ at r = 1.3 ± 0.2 mm on 316L and NAB, pit depth on aluminum from P&L 1998.

6.3.8 Influence of the Material

Fig. 50 shows the damage progression on 316L and NAB at approximately γ = 1.1 up to 170 000 and 80 000 bubbles, respectively. The pits form mainly in two regions on the laser axis. In both samples, a ring corresponding to the region of the second collapse can be seen at this γ (see Fig. 42 and Fig. 43). The larger radius in the NAB damage pattern is due to the slightly larger maximum radius of the bubbles. On 316L, material damage can be seen beyond the pits at the grain boundaries (black arrows). This type of damage was also found in experiments in previous chapters for γ = 1.4. It is a step in the transition from single pits to eventual material loss [78]. Comparable damage does not occur in the bronze due to the different microstructure [78]. In our experiments here, we found that for all investigated stand-off distances the effect of pitting on the material was similar to the damage process described in [78]. Therefore, even if for a given combination of stand-off distance and bubble size the pitting rate is low, the evolution of damage into erosion happens in a similar manner, just more slowly.

From Fig. 50, but also from comparison of the damage patterns shown in Fig. 40 to damage on aluminum in the literature (e.g. [11, 12]) the similarity of damage pattern across ductile materials investigated here is evident.

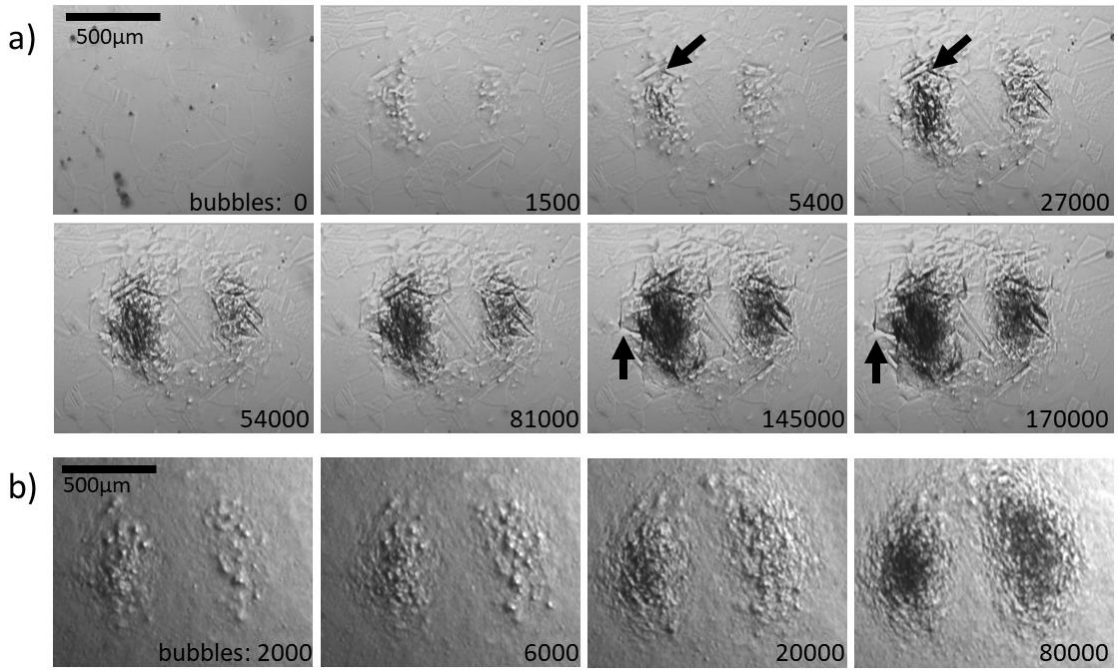

Fig. 50 In-situ images of the damage progression on a) 316L at γ = 1.15 andd r = 1.1 mm, b) NAB at γ = 1.09 and r = 1.3 mm. The laser incidence is from the right. The arrows mark features discussed in the text.

Some experiments were also carried out on aluminum, which we previously had only done at γ = 1.4 [82, 90]. The correlation of SCAs and pits on aluminum can be seen in Fig. 51b. For this particular bubble, two SCAs and two pits occurred. As on steel (Fig. 40a and Fig. 44b-c), the pits occur in two opposite regions away from the laser axis. The images for 50 and 200 bubbles in Fig. 51a show a phenomenon also observed in previous chapters on aluminum: At constant stand-off distance, the pit size varies more than on the technical alloys [82, 90]. Large scatter in pit metrics caused by single bubbles on aluminum was also found by P&L 1998 [11] and Sagar et al. [10]. This is probably caused by the variation in the load exerted by the individual collapse events. Compared to the technical alloys, on aluminum far weaker parts of the collapse are sufficient to cause plastic deformation, and thus there is a greater variation in the load that causes pitting.

In Fig. 51, the center of the bubble projected onto the surface of the sample is marked with a black x in some of the images. This is the point where the liquid jet of the bubble hits the surface [11]. Both the surface quantitative elevation map from confocal microscopy and the qualitative in-situ microscope image show that plastic

deformation of the sample surface did not occur in this area. Apparently, even on a material as soft as pure aluminum, 200 bubble collapses with a stand-off distance well below 1 were not sufficient to lead to deformation by the jet.

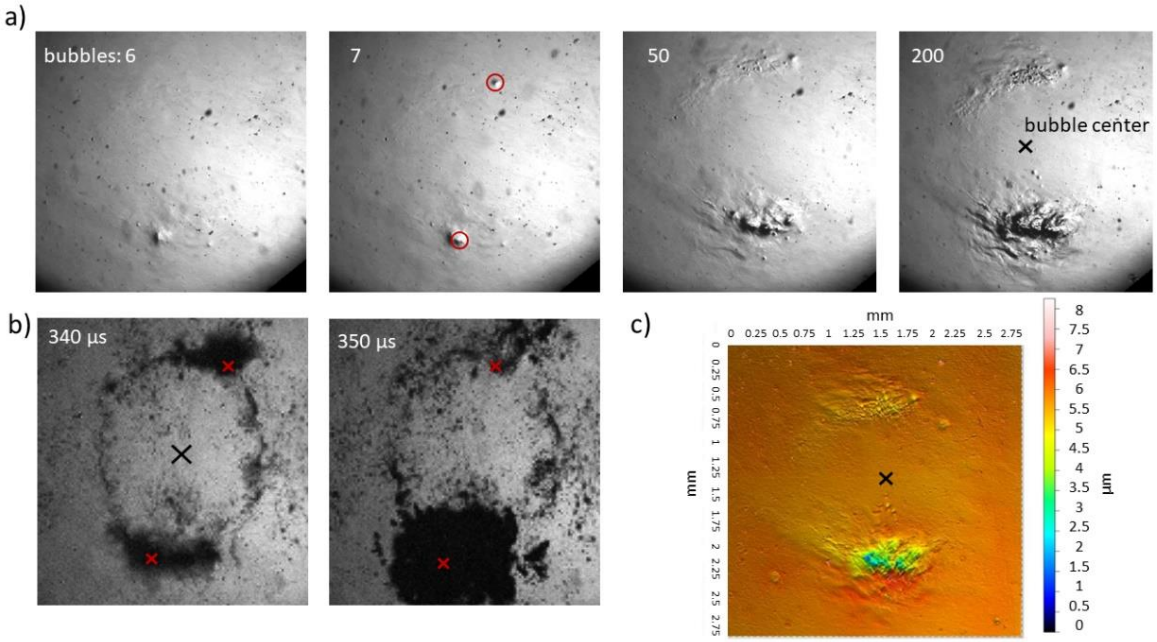

Fig. 51 Aluminum surface after 6, 7 and 50 and 200 bubbles imaged in-situ (a) and surface elevation from ex-situ confocal microscopy after 200 bubbles (c) at $\gamma = 0.74$ and r = 1.4 mm. Additionally, the second collapse of the 7th bubble is shown (b). The red circles mark the pits caused by the 7th bubble. The red x marks the pit location in the images of the second collapse. The projection of the bubble center on the surface is marked with a black x. All images refer to the same spatial scale as (c). The laser incidence is from the right.

6.3.9 Chapter Conclusions

In this chapter we investigated the formation of early cavitation damage on two technical alloys and on pure aluminum for a wide range of stand-off distances and bubble diameters. The experiments focused on 316L, a ductile technical alloy. Some experiments were also performed with a nickel-aluminum bronze (NAB) – a more cavitation-resistant, multi-phase material – and with pure aluminum, a soft metal. The damage caused by cavitation bubbles was correlated with the bubble dynamics, including an example of shockwaves emitted during the second collapse. Pits occur on 316L for stand-off distances less than $\gamma = 2.15$. Over a series of single bubbles, they accumulate in patterns that depend on the stand-off distance and are influenced by asymmetries in the experiment. This is consistent with the literature [10–12].

We showed that for stand-off distances larger than 0.4 in general “stronger” parts (SCAs) in the *second* collapse spatially correlate with pits, while for smaller stand-off distances stronger parts of the *first* collapse correlate with pits. In experiments focusing on the second collapse with $\gamma = 1.4$, these SCAs were also found to be the regions where shock waves are emitted. SCAs appear to be those parts of the bubble that locally collapses last. This became most obvious in experiments where the bubble collapse was forced to be asymmetric but is most likely more generally true. The central jet associated with the first collapse was found irrelevant for damaging of any of the materials investigated here.

For 316L, the pitting rate was investigated for different radii at fixed stand-off distance and for different stand-off distances at fixed radius. The results show that the average number of pits caused by a collapsing bubble is strongly dependent on both parameters. The pitting rate increases linearly with the bubble size in the studied interval from 0.75 to 1.5 mm radius. While our experiment cannot reproducibly create smaller bubbles, linear extrapolation implies a limiting radius of 0.4 mm below which at $\gamma = 1.4$ 316 L is not damaged by pitting. The dependence of pitting rate on stand-off distance is more complex. Pits occurred at all stand-off distances up to $\gamma = 2.15$, and there is a global maximum in the pitting rate at the smallest stand-off distances investigated here, $\gamma = 0.25$, and a local one at $\gamma = 1.4$. This shape of this curve of pitting rate vs. stand-off distance was the same for 316L and NAB, closely resembles that for other damage metrics vs. γ on aluminum [11], and is consistent with the damage on the oxide layer of aluminum recently deduced from transient electric current measurements [99].

In experiments with large numbers of bubbles effect of the summation of pits was found to be similar for 316L and NAB, and the damage progressed in the same way for stand-off distances other than the previously investigated $\gamma = 1.4$. Although different materials experience different pitting rates [82], the pits vary more in size in softer materials, and the process leading to material loss due to pitting can be different [78, 90], all indications are that the fluid dynamic mechanisms responsible for pit creation are the same. Therefore, if single cavitation bubbles cause pitting, a sufficient number of bubbles will eventually cause material loss as described in [78] for the tested materials.

7. Conclusion

This work explored the use of in-situ microscopy to study single-bubble cavitation induced damage on technical alloys. The method involved generating successive single bubbles using focused laser pulses and capturing microscope images of the surface after each bubble. Additionally, up to two high-speed cameras recorded the bubble dynamics. Three different materials - pure aluminum, stainless steel, and nickel-aluminum bronze - were tested, and the results were validated against established ex-situ microscopy techniques. The focus of this work laid in the beginning of cavitation damage before erosion occurs. However, also later stages of damage formation after up to hundred-thousands of bubbles were examined as well. At all stages of damage formation, the occurrence of pits was a fundamental result of the bubble collapses. Therefore, pits were counted, analyzed and correlated with dynamics of cavitation bubbles. Furthermore, the influence of stand-off distances and bubble radii on pitting was investigated.

A somewhat consistent picture of single-bubble damage on flat metal surfaces emerges:

- The first optically detectable change of the solid surface due to collapsing single cavitation bubbles are pits that are much smaller than the bubble diameter (Chapter 4, Chapter 5 and Chapter 6) and [11, 12].
- Already the very first bubble can cause pitting, even on technical alloys (Chapter 4, Chapter 5 and Chapter 6).
- But not every bubble causes pits, even on soft aluminum (Chapter 4 and Chapter 5).
- The spatial patterns in which pits occur are the same for technical alloys as for soft materials and are mainly dependent on the stand-off distance (Chapter 4 and Chapter 6) and [11].
- The central liquid jet that is associated with the first collapse does not play a significant role in causing damage (Chapter 6) and [11, 81]
- For stand-off distances greater than 0.4, pits are primarily associated with “stronger” parts of the second collapse. These are regions where the bubble locally collapses last, consistent with “subsonic energy focusing” (Chapter 6) and [81].

- Shock waves are emitted from these regions into the fluid. It seems reasonable that shock waves also are emitted into the solid and are at least partly responsible for the pits (Chapter 6) and [11, 81].
- For stand-off distances less than 0.4, pits are more closely related to the stronger parts of the first – not the second – collapse (Chapter 6) and [81, 99]
- The pitting rate – an indicator of early damage progression – decreases with decreasing bubble radius (Chapter 6).
- Linear extrapolation indicates that a non-zero minimum bubble diameter is required to cause any pits (Chapter 6).
- The pitting rate varies non-monotonically with γ, peaking at $\gamma = 1.4$ and for $\gamma < 0.4$. This trend is consistent across materials and with other damage metrics (Chapter 6) and [11].
- Over many single bubbles the accumulation of pits triggers material-specific damage mechanisms that finally lead to erosion (Chapter 6) and [78]

In summary, compared to the somewhat better-known single-bubble cavitation damage of aluminum, it is found that on technical alloys the early cavitation damage forms very similarly. Individual pits occur in the same way, correlated to SCAs of bubble collapses, and they accumulate in similar damage patterns depending on the experimental parameters. However, these pits are much smaller and occur much less frequently on technical alloys. The mode of further damage via the accumulation of pits and the onset of erosion then depends on the specific material and in particular its microstructure [78].

8. Future Work

Based on the results of this work there are several avenues of future investigation that promise to advance our understanding of cavitation and cavitation damage.

The manual counting of pits to determine the pitting rate is both time-consuming and susceptible to subjective interpretation by the individual performing the count. A more efficient and potentially more objective alternative lies in employing artificial intelligence (AI) to detect pits across a series of images. Section 10.2 in the appendix provides a concise overview of some results of an implementation of such a system for 316L. AI not only circumvents the drawbacks associated with manual counting but also unlocks additional opportunities for analysis. For instance, the correlation of the pit positions given by the AI evaluation with SCA occurrence presents a promising application. For this evaluation, an AI analysis could also be applied to high-speed data of the bubble dynamics. Moreover, the data acquired with AI hold potential for facilitating modeling or predicting cavitation erosion.

Following up on Section 6.3.7, the minimum bubble radius that still induces detectable pitting should be directly measured in experiments with smaller bubbles. In addition, tests should be carried out on the pitting rate with increased radii. A first step in this direction was taken already and the results validating the linear trend can be found in Section 10.2.

Different materials can be studied with the methods presented in this work. Due to the fact that grain or phase boundaries are regions where erosion starts, the question arises how the damage progresses in a single-crystal material – or at least a material with grains of a size much larger than the damaged area. Section 10.4 of the appendix indicates that it is important to examine the damage in connection with the grain size. This section shows that even a single pit can have an effect on the grain boundaries of very small grains. Similarly, it might be interesting to look at materials that show minimal plastic deformation (hard, brittle materials) and see how erosion occurs there.

Further investigations are needed on the energy transmission from liquid and gas to solid. Even though the shock wave proved to be most likely the cause of pitting in our experiments, it is not clear why plastic deformation occurs at such high strain rates, and the material does not show immediate cracking or material loss. Possible reasons for the plastic response of the solid could be the multiaxiality of the specific

stress state, or potentially locally high temperatures during the collapse. The latter hypothesis could be tested by an optical measurement of temperature.

Simulations could also be helpful to investigate temperature during the collapse. In addition, 3D simulations are needed to better understand the occurrence of SCAs. Here, initial conditions close to the experimental conditions with a plasma breakdown may be essential to for accurately modeling the experiment.

At last, modeling of the material on an atomic level might help understanding the damage formation from early damage to later stages of erosion.

9. References

1. Dular, M., Bachert, B., Stoffel, B., Širok, B.: Relationship between cavitation structures and cavitation damage. Wear (2004). https://doi.org/10.1016/j.wear.2004.08.004
2. Kim, K.-H., Chahine, G., Franc, J.-P., Karimi, A.: Advanced Experimental and Numerical Techniques for Cavitation Erosion Prediction, vol. 106, 1st ed., Springer Netherlands, Dordrecht (2014), pp. 1- 68.
3. Hanke, S., Kaiser, S.A.: Comparison of damage mechanisms: Acoustic cavitation versus series of single laser-induced bubbles. Wear (2021). https://doi.org/10.1016/j.wear.2021.203641
4. Luo, X., Ji, B., Tsujimoto, Y.: A review of cavitation in hydraulic machinery. J Hydrodyn (2016). https://doi.org/10.1016/S1001-6058(16)60638-8
5. Kumar, P., Saini, R.P.: Study of cavitation in hydro turbines—A review. Renewable and Sustainable Energy Reviews (2010). https://doi.org/10.1016/j.rser.2009.07.024
6. Priyadarshi, A., Krzemień, W., Salloum-Abou-Jaoude, G., Broughton, J., Pericleous, K., Eskin, D., Tzanakis, I.: Effect of water temperature and induced acoustic pressure on cavitation erosion behaviour of aluminium alloys. Tribology International (2023). https://doi.org/10.1016/j.triboint.2023.108994
7. Kozmus, G., Zevnik, J., Hočevar, M., Dular, M., Petkovšek, M.: Characterization of cavitation under ultrasonic horn tip - Proposition of an acoustic cavitation parameter. Ultrasonics sonochemistry (2022). https://doi.org/10.1016/j.ultsonch.2022.106159
8. Lauterborn, W.: High‐speed photography of laser‐induced breakdown in liquids. Appl. Phys. Lett. (1972). https://doi.org/10.1063/1.1654204
9. Lindua, O., Lauterborn, W.: Cinematographic observation of the collapse and rebound of a laser-produced cavitation bubble near a wall. J. Fluid Mech. (2003). https://doi.org/10.1017/S0022112002003695
10. Sagar, H.J., Hanke, S., Underberg, M., Feng, C., el Moctar, O., Kaiser, S.A.: Experimental and Numerical Investigation of Damage on an Aluminum Surface by Single-Bubble Cavitation. Matls. Perf. Charact. (2018). https://doi.org/10.1520/MPC20180038
11. Philipp, A., Lauterborn, W.: Cavitation erosion by single laser-produced bubbles. J. Fluid Mech. (1998). https://doi.org/10.1017/S0022112098008738
12. Isselin, J.-C., Alloncle, A.-P., Autric, M.: On laser induced single bubble near a solid boundary: Contribution to the understanding of erosion phenomena. Journal of Applied Physics (1998). https://doi.org/10.1063/1.368841
13. Brennen, C.E.: Cavitation and bubble dynamics. The Oxford engineering science series, vol. 44. Oxford Univ. Press, 1st ed., New York (1995), pp. 1- 58.
14. Wolschin, G.: Hydrodynamik, 2nd ed. Springer Spektrum, Berlin (2022), pp. 13-14.
15. Kuiper, G.: Cavitation Research and Ship Propeller Design. Flow, Turbulence and Combustion (1997). https://doi.org/10.1023/A:1000754928962
16. Silverrad D.: Propeller erosion. Engineering, vol. 33 (1912)

17. Hutli, E., Nedeljkovic, M.S., Radovic, N.A., Bonyár, A.: The relation between the high speed submerged cavitating jet behaviour and the cavitation erosion process. International Journal of Multiphase Flow (2016). https://doi.org/10.1016/j.ijmultiphaseflow.2016.03.005
18. Abbasi, A.A., Viviani, M., Bertetta, D., Delucchi, M., Ricotti, R., Tani, G.: Experimental Analysis of Cavitation Erosion on Blade Root of Controllable Pitch Propeller. In: Rizzuto, E., Ruggiero, V. (eds.) Technology and Science for the Ships of the Future. Progress in Marine Science and Technology. IOS Press (2022)
19. Ibanez, I., Zeqiri, B., Hodnett, M., Frota, M.N.: Cavitation-erosion measurements on engineering materials. Engineering Science and Technology, an International Journal (2020). https://doi.org/10.1016/j.jestch.2020.06.001
20. G02 Committee: Test Method for Cavitation Erosion Using Vibratory Apparatus. ASTM International, West Conshohocken, PA
21. Schreiner, F., Hanke, S., Skoda, R.: Assessment of flow aggressiveness and erosion damage topography for different gap widths in ultrasonic cavitation testing. Wear (2021). https://doi.org/10.1016/j.wear.2021.203989
22. Escaler, X., Farhat, M., Avellan, F., Egusquiza, E.: Cavitation erosion tests on a 2D hydrofoil using surface-mounted obstacles. Wear (2003). https://doi.org/10.1016/S0043-1648(03)00261-8
23. Plesset, M.S.: The Dynamics of Cavitation Bubbles. Journal of Applied Mechanics (1949). https://doi.org/10.1115/1.4009975
24. Franc, J.-P., Michel, J.-M.: Fundamentals of cavitation. Fluid mechanics and its applications, v. 76. Kluwer Academic Publishers, 1st ed., Dordrecht, Boston (2005), pp. 35-55.
25. Yasui, K.: Bubble Dynamics. In: Yasui, K. (ed.) Acoustic Cavitation and Bubble Dynamics. SpringerBriefs in Molecular Science, Springer International Publishing, 1st ed., Cham (2018), pp. 37–97.
26. Zhong, X., Eshraghi, J., Vlachos, P., Dabiri, S., Ardekani, A.M.: A model for a laser-induced cavitation bubble. International Journal of Multiphase Flow (2020). https://doi.org/10.1016/j.ijmultiphaseflow.2020.103433
27. Yasui, K.: Effect of non-equilibrium evaporation and condensation on bubble dynamics near the sonoluminescence threshold. Ultrasonics (1998). https://doi.org/10.1016/S0041-624X(97)00107-8
28. Obreschkow, D., Tinguely, M., Dorsaz, N., Kobel, P., Bosset, A. de, Farhat, M.: The quest for the most spherical bubble: experimental setup and data overview. Exp Fluids (2013). https://doi.org/10.1007/s00348-013-1503-9
29. Vogel, A., Busch, S., Parlitz, U.: Shock wave emission and cavitation bubble generation by picosecond and nanosecond optical breakdown in water. The Journal of the Acoustical Society of America (1996). https://doi.org/10.1121/1.415878
30. Keller, J.B., Miksis, M.: Bubble oscillations of large amplitude. The Journal of the Acoustical Society of America (1980). https://doi.org/10.1121/1.384720
31. Freemann, M., Hull, C., Charman, W.: Optics, 11th ed., Butterworth-Heinemann, Edinburgh, London, New York (2003), pp. 1-84, 304-334.

32. Born, M., Wolf, E.: Principles of optics. Electromagnetic theory of progagation, interference and diffraction of light, 7th ed. Cambridge University Press, Cambridge (US) (2009), pp. 118-281.
33. Hecht, E.: Optics, eBook, Global Edition, 5th ed. Pearson (2016), chs. 5-6.
34. Kneubühl,F. , Sigrist, W.: Laser. Vieweg+Teubner Verlag (1989), pp. 1-46; 70-93.
35. Hammond C., Heath J. P.: Ray Diagrams of the Optical Pathways in Light Microscopes. Microscopy and Analysis (2006)
36. Käthner, R.J., Zölffel, M.: Lichtmikroskopie. Technologie und Anwendung. Die Bibliothek der Technik, Band 380. Verlag Moderne Industrie, München (2016), pp. 4-55.
37. Jindal, U.C.: Material science and metallurgy, 1st ed. Dorling Kindersley, New Delhi (2012), chs. 1-4.
38. Armstrong, R.W.: The influence of polycrystal grain size on several mechanical properties of materials. Metall Trans (1970). https://doi.org/10.1007/BF02900227
39. Morris Jr., J.: The influence of grain size on the mechanical properties of steel. Lawrence Berkeley National Laboratory. (2001)
40. Hornbogen, E., Warlimont, H.: Metalle. Struktur und Eigenschaften der Metalle und Legierungen, 5th ed. Springer, Berlin (2015), pp. 51 - 68, 119 – 149.
41. Armstrong, R.W., Walley, S.M.: High strain rate properties of metals and alloys. International Materials Reviews (2008). https://doi.org/10.1179/174328008X277795
42. Blake, J.R., Gibson, D.C.: Cavitation Bubbles Near Boundaries. Annu. Rev. Fluid Mech. (1987). https://doi.org/10.1146/annurev.fl.19.010187.000531
43. Lauterborn, W., Vogel, A.: Shock Wave Emission by Laser Generated Bubbles. In: Delale, C.F. (ed.) Bubble Dynamics and Shock Waves, Springer Berlin Heidelberg, Berlin, Heidelberg (2013), pp. 67–103.
44. Vogel, A., Lauterborn, W., Timm, R.: Optical and acoustic investigations of the dynamics of laser-produced cavitation bubbles near a solid boundary. J. Fluid Mech. (1989). https://doi.org/10.1017/S0022112089002314
45. Buogo, S., Cannelli, G.B.: Implosion of an underwater spark-generated bubble and acoustic energy evaluation using the Rayleigh model. The Journal of the Acoustical Society of America (2002). https://doi.org/10.1121/1.1476919
46. Huang, Y., Yan, H., Wang, B., Zhang, X., Liu, Z., Yan, K.: The electro-acoustic transition process of pulsed corona discharge in conductive water. J. Phys. D: Appl. Phys. (2014). https://doi.org/10.1088/0022-3727/47/25/255204
47. Cook, J.A., Gleeson, A.M., Roberts, R.M., Rogers, R.L.: A spark-generated bubble model with semi-empirical mass transport. The Journal of the Acoustical Society of America (1997). https://doi.org/10.1121/1.418236
48. Brewer, R.G., Rieckhoff, K.E.: Stimulated Brillouin Scattering in Liquids. Phys. Rev. Lett. (1964). https://doi.org/10.1103/PhysRevLett.13.334
49. Noack, J., Vogel, A.: Laser-induced plasma formation in water at nanosecond to femtosecond time scales: calculation of thresholds, absorption coefficients, and energy density. IEEE J. Quantum Electron. (1999). https://doi.org/10.1109/3.777215

50. Akhatov, I., Lindau, O., Topolnikov, A., Mettin, R., Vakhitova, N., Lauterborn, W.: Collapse and rebound of a laser-induced cavitation bubble. Physics of Fluids (2001). https://doi.org/10.1063/1.1401810
51. Gonzalez-Avila, S.R., Klaseboer, E., Khoo, B.C.O., Ohl, C.-D.: Cavitation bubble dynamics in a liquid gap of variable height. J. Fluid Mech. (2011). https://doi.org/10.1017/jfm.2011.212
52. Reuter, F., Gonzalez-Avila, S.R., Mettin, R., Ohl, C.-D.: Flow fields and vortex dynamics of bubbles collapsing near a solid boundary. Phys. Rev. Fluids (2017). https://doi.org/10.1103/PhysRevFluids.2.064202
53. Brujan, E.A., Keen, G.S., Vogel, A., Blake, J.R.: The final stage of the collapse of a cavitation bubble close to a rigid boundary. Physics of Fluids (2002). https://doi.org/10.1063/1.1421102
54. Tomita, Y., Shima, A.: Mechanisms of impulsive pressure generation and damage pit formation by bubble collapse. J. Fluid Mech. (1986). https://doi.org/10.1017/S0022112086000745
55. Lauterborn, W., Ohl, C.-D.: Cavitation bubble dynamics. Ultrasonics sonochemistry (1997). https://doi.org/10.1016/S1350-4177(97)00009-6
56. Blake, J.R., Leppinen, D.M., Wang, Q.: Cavitation and bubble dynamics: the Kelvin impulse and its applications. Interface focus (2015). https://doi.org/10.1098/rsfs.2015.0017
57. Benjamin, T.B., Ellis, A.T.: A discussion on deformation of solids by the impact of liquids, and its relation to rain damage in aircraft and missiles, to blade erosion in steam turbines, and to cavitation erosion - The collapse of cavitation bubbles and the pressures thereby produced against solid boundaries. Phil. Trans. R. Soc. Lond. A (1966). https://doi.org/10.1098/rsta.1966.0046
58. Supponen, O., Obreschkow, D., Tinguely, M., Kobel, P., Dorsaz, N., Farhat, M.: Scaling laws for jets of single cavitation bubbles. J. Fluid Mech. (2016). https://doi.org/10.1017/jfm.2016.463
59. Reuter, F., Kaiser, S.A.: High-speed film-thickness measurements between a collapsing cavitation bubble and a solid surface with total internal reflection shadowmetry. Physics of Fluids (2019). https://doi.org/10.1063/1.5095148
60. Kühlmann, J., Kaiser, S.A.: Single-Bubble Cavitation-Induced Pitting on Technical Alloys. Tribol Lett (2024). https://doi.org/10.1007/s11249-024-01851-7
61. Schreiner, F., Gianfelice, T., Skoda, R.: Three-dimensional simulation of an orifice flow with cavitation-induced air release. International Journal of Multiphase Flow (2024). https://doi.org/10.1016/j.ijmultiphaseflow.2024.104824
62. Li, Y., Ouyang, J., Peng, Y., Liu, Y.: Numerical Simulation of Cavitation Bubble Collapse inside an Inclined V-Shape Corner by Thermal Lattice Boltzmann Method. Water (2024). https://doi.org/10.3390/w16010161
63. Kadivar, E., Timoshevskiy, M.V., Pervunin, K.S., Moctar, O.e.: Experimental and numerical study of the cavitation surge passive control around a semi-circular leading-edge flat plate. J Mar Sci Technol (2020). https://doi.org/10.1007/s00773-019-00697-2
64. Falsafi, S., Blume, M., Klaua, T., Indrich, M., Wloka, J., Skoda, R.: Numerical simulation of cavitating flow in maritime high-pressure direct fuel injection nozzles and assessment of

cavitation-erosion damage. International Journal of Engine Research (2023). https://doi.org/10.1177/14680874211052138

65. Plesset, M.S., Chapman, R.B.: Collapse of an initially spherical vapour cavity in the neighbourhood of a solid boundary. J. Fluid Mech. (1971). https://doi.org/10.1017/S0022112071001058
66. Mitchell, T.M., Hammitt, F.G.: Asymmetric Cavitation Bubble Collapse. Journal of Fluids Engineering (1973). https://doi.org/10.1115/1.3446954
67. Bempedelis, N., Ventikos, Y.: A simplified approach for simulations of multidimensional compressible multicomponent flows: The grid-aligned ghost fluid method. Journal of Computational Physics (2020). https://doi.org/10.1016/j.jcp.2019.109129
68. Bußmann, A., Riahi, F., Gökce, B., Adami, S., Barcikowski, S., Adams, N.A.: Investigation of cavitation bubble dynamics near a solid wall by high-resolution numerical simulation. Physics of Fluids (2023). https://doi.org/10.1063/5.0135924
69. Yin, J., Zhang, Y., Qi, X., Tian, L., Gong, D., Ma, M.: Numerical investigation of the cavitation bubble near the solid wall with a gas-entrapping hole based on a fully compressible three-phase model. Ultrasonics sonochemistry (2023). https://doi.org/10.1016/j.ultsonch.2023.106531
70. Lechner, C., Koch, M., Lauterborn, W., Mettin, R.: Fast jets from bubbles close to solid objects: examples from pillars in water to infinite planes in different liquids (2023). https://doi.org/10.24352/UB.OVGU-2023-042
71. Koch, M., Rosselló, J.M., Lechner, C., Lauterborn, W., Eisener, J., Mettin, R.: Theory-assisted optical ray tracing to extract cavitation-bubble shapes from experiment. Exp Fluids (2021). https://doi.org/10.1007/s00348-020-03075-6
72. Sagar, H.J., el Moctar, O.: Numerical simulation of a laser-induced cavitation bubble near a solid boundary considering phase change. Ship Technology Research (2018). https://doi.org/10.1080/09377255.2018.1473235
73. Dijkink, R., Le Gac, S., Nijhuis, E., van den Berg, A., Vermes, I., Poot, A., Ohl, C.-D.: Controlled cavitation-cell interaction: trans-membrane transport and viability studies. Physics in medicine and biology (2008). https://doi.org/10.1088/0031-9155/53/2/006
74. Brennen, C.E.: Cavitation in medicine. Interface focus (2015). https://doi.org/10.1098/rsfs.2015.0022
75. Barcikowski, S., Plech, A., Suslick, K.S., Vogel, A.: Materials synthesis in a bubble. MRS Bull. (2019). https://doi.org/10.1557/mrs.2019.107
76. Ohl, C.-D., Arora, M., Dijkink, R., Janve, V., Lohse, D.: Surface cleaning from laser-induced cavitation bubbles. Appl. Phys. Lett. (2006). https://doi.org/10.1063/1.2337506
77. Reuter, F., Lauterborn, S., Mettin, R., Lauterborn, W.: Membrane cleaning with ultrasonically driven bubbles. Ultrasonics sonochemistry (2017). https://doi.org/10.1016/j.ultsonch.2016.12.012
78. Lopez de Arcaute y Lozano, C., Kühlmann, J., Kaiser, S.A., Hanke, S.: Observing early cavitation damage evolution from repeated laser-induced single bubbles on aluminium, austenitic steel and nickel-aluminium bronze. Wear (2023). https://doi.org/10.1016/j.wear.2023.204862

79. Reuter, F., Ohl, C.-D.: Supersonic needle-jet generation with single cavitation bubbles. Appl. Phys. Lett. (2021). https://doi.org/10.1063/5.0045705
80. Dular, M., Požar, T., Zevnik, J., Petkovšek, R.: High speed observation of damage created by a collapse of a single cavitation bubble. Wear (2019). https://doi.org/10.1016/j.wear.2018.11.004
81. Reuter, F., Deiter, C., Ohl, C.-D.: Cavitation erosion by shockwave self-focusing of a single bubble. Ultrasonics sonochemistry (2022). https://doi.org/10.1016/j.ultsonch.2022.106131
82. Kühlmann, J., Lopez de Arcaute y Lozano, Christina, Hanke, S., Kaiser, S.A.: In-situ Investigation of the Onset of Cavitation Damage from Single Bubbles on Technical Alloys. Tribol Lett (2022). https://doi.org/10.1007/s11249-022-01665-5
83. Fuchs, U., Braun, D., Wickenhagen, S.: Beam shaping concepts with aspheric surfaces. In: Forbes, A., Lizotte, T.E. (eds.) Laser Beam Shaping XVI. SPIE Optical Engineering + Applications, San Diego, California, United States, Sunday 9 August 2015, 95810L. SPIE (2015). https://doi.org/10.1117/12.2186524
84. Tian, Y., Xue, B., Song, J., Lu, Y., Zheng, R.: Stabilization of laser-induced plasma in bulk water using large focusing angle. Appl. Phys. Lett. (2016). https://doi.org/10.1063/1.4960711
85. Sinibaldi, G., Occhicone, A., Alves Pereira, F., Caprini, D., Marino, L., Michelotti, F., Casciola, C.M.: Laser induced cavitation: Plasma generation and breakdown shockwave. Physics of Fluids (2019). https://doi.org/10.1063/1.5119794
86. Gonzalez-Parra, J.C., Robles, V., Devia-Cruz, L.F., Rodriguez-Beltran, R.I., Cuando-Espitia, N., Camacho-Lopez, S., Aguilar, G.: Mitigation of cavitation erosion using laser-induced periodic surface structures. Surfaces and Interfaces (2022). https://doi.org/10.1016/j.surfin.2021.101692
87. Kadivar, E., Moctar, O.e., Skoda, R., Löschner, U.: Experimental study of the control of cavitation-induced erosion created by collapse of single bubbles using a micro structured riblet. Wear (2021). https://doi.org/10.1016/j.wear.2021.204087
88. Dular, M., Stoffel, B., Širok, B.: Development of a cavitation erosion model. Wear (2006). https://doi.org/10.1016/j.wear.2006.01.020
89. Gao, G., Zhang, Z.: Cavitation Erosion Behavior of 316L Stainless Steel. Tribol Lett (2019). https://doi.org/10.1007/s11249-019-1225-0
90. Kühlmann, J., Lopez de Arcaute y Lozano, Christina, Hanke, S., Kaiser, S.A.: Correlation of laser-induced single bubbles with cavitation damage via in-situ imaging. Wear (2023). https://doi.org/10.1016/j.wear.2023.204723
91. Petzow, G.: Metallographisches, keramographisches, plastographisches Ätzen. P. 48, 7th ed. Materialkundlich-technische Reihe, vol. 1. Gebrüder Borntraeger, Stuttgart (2015)
92. Niederhofer, P., Pöhl, F., Geenen, K., Huth, S., Theisen, W.: Influence of crystallographic orientation on cavitation erosion resistance of high interstitial CrMnCN austenitic stainless steels. Tribology International (2016). https://doi.org/10.1016/j.triboint.2015.11.002
93. Chahine, G.L., Hsiao, C.-T.: Modelling cavitation erosion using fluid-material interaction simulations. Interface focus (2015). https://doi.org/10.1098/rsfs.2015.0016

94. Schaffer, C., Nishimura, N., Glezer, E., Kim, A., Mazur, E.: Dynamics of femtosecond laser-induced breakdown in water from femtoseconds to microseconds. Optics express (2002). https://doi.org/10.1364/OE.10.000196
95. Supponen, O., Obreschkow, D., Kobel, P., Tinguely, M., Dorsaz, N., Farhat, M.: Shock waves from nonspherical cavitation bubbles. Phys. Rev. Fluids (2017). https://doi.org/10.1103/physRevFluids.2.093601
96. Mørch, K.A.: Cavitation Nuclei: Experiments and Theory. J Hydrodyn (2009). https://doi.org/10.1016/S1001-6058(08)60135-3
97. Kell, G.S.: Effects of isotopic composition, temperature, pressure, and dissolved gases on the density of liquid water. Journal of Physical and Chemical Reference Data (1977). https://doi.org/10.1063/1.555561
98. Franc, J.-P.: Incubation Time and Cavitation Erosion Rate of Work-Hardening Materials. Journal of Fluids Engineering (2009). https://doi.org/10.1115/1.3063646
99. Abedini, M., Hanke, S., Reuter, F.: In situ measurement of cavitation damage from single bubble collapse using high-speed chronoamperometry. Ultrasonics sonochemistry (2023). https://doi.org/10.1016/j.ultsonch.2022.106272
100. Veysel Ersoy: Detection of cavitation-induced pitting on metal samples via neural-network based image processing. Master thesis, University Duisburg-Essen (2024)
101. Luigi Mazzeo, P., Ramakrishnan, S., Spagnolo, P. (eds.): Visual Object Tracking with Deep Neural Networks. IntechOpen (2019)
102. Xia, B., Luo, H., Shi, S.: Improved Faster R-CNN Based Surface Defect Detection Algorithm for Plates. Computational intelligence and neuroscience (2022). https://doi.org/10.1155/2022/3248722
103. Hao, Z., Wang, Z., Bai, D., Tao, B., Tong, X., Chen, B.: Intelligent Detection of Steel Defects Based on Improved Split Attention Networks. Frontiers in bioengineering and biotechnology (2021). https://doi.org/10.3389/fbioe.2021.810876
104. Khan, G., Tariq, Z., Usman Ghani Khan, M.: Multi-Person Tracking Based on Faster R-CNN and Deep Appearance Features. In: Luigi Mazzeo, P., Ramakrishnan, S., Spagnolo, P. (eds.) Visual Object Tracking with Deep Neural Networks. IntechOpen (2019)

9.1 Contribution of the Author

Journal Articles

82. Kühlmann, J., Lopez de Arcaute y Lozano, Christina, Hanke, S., Kaiser, S.A.: In-situ Investigation of the Onset of Cavitation Damage from Single Bubbles on Technical Alloys. Tribol Lett (2022). https://doi.org/10.1007/s11249-022-01665-5

I built the experimental apparatus, performed the experiments, and analyzed the data. I wrote the first draft of the manuscript. I contributed to the study conception and was responsible for the management of the paper.

90. Kühlmann, J., Lopez de Arcaute y Lozano, Christina, Hanke, S., Kaiser, S.A.: Correlation of laser-induced single bubbles with cavitation damage via in-situ imaging. Wear (2023). https://doi.org/10.1016/j.wear.2023.204723

I built the experimental apparatus, performed the experiments, and evaluated the data. I wrote the first draft of the manuscript. I contributed to the study conception and was responsible for managing the paper.

78. Lopez de Arcaute y Lozano, C., Kühlmann, J., Kaiser, S.A., Hanke, S.: Observing early cavitation damage evolution from repeated laser-induced single bubbles on aluminium, austenitic steel and nickel-aluminium bronze. Wear (2023). https://doi.org/10.1016/j.wear.2023.204862

I performed the single-bubble experiments of this work. I reviewed the manuscript.

No results of this article are included as a part of this work. However, the relevant results are discussed in Section 3.3.2.

60. Kühlmann, J. and Kaiser, S.A.: Single-Bubble Cavitation-Induced Pitting on Technical Alloys. Tribol Lett (2024). https://doi.org/10.1007/s11249-024-01851-7

I built the experimental apparatus, performed the experiments, and evaluated the data. I wrote the first draft of the manuscript. I contributed to the study conception and was responsible for managing the paper.

Conference Contributions

Papers with oral presentation:

Kühlmann, J., Lopez de Arcaute y Lozano, Christina, Hanke, S., Kaiser, S.A.: Correlation of laser-induced single bubbles with cavitation damage via in-situ imaging, April 16th -20th 2023, Banff, Canada.

Oral presentations:

Kühlmann, J., Lopez de Arcaute y Lozano, Christina, Hanke, S., Kaiser, S.A.: Investigation of surface damage caused by multiple laser-induced single bubble events, at the Cavitation Colloquium November 29th – December 1st 2021, Drübeck, Germany.

Kühlmann, J., Lopez de Arcaute y Lozano, Christina, Hanke, S., Kaiser, S.A.: Correlation of laser-induced single bubbles with cavitation damage via in-situ imaging, at the Cavitation Colloquium 2022 November 9th – November 10th 2022, Mühlheim, Germany.

Kühlmann, J., Hanke, S., Kaiser, S.A.: Single-bubble cavitation-induced pitting on technical alloys, at the Cavitation Colloquium 2023 November 1st – November 3rd, Drübeck, Germany.

Supervised Theses

Susek Gazi, Investigation of the damage of different materials by laser-induced single cavitation bubbles, master's thesis, University of Duisburg-Essen, 2022.

Veysel Ersoy**,** Detection of cavitation-induced pitting on metal samples via neural-network based image processing, master's thesis, University of Duisburg-Essen, 2024.

10. Appendix

10.1 Appendix - Single-bubble cavitation Induced Pitting on Technical Alloys

10.1.1 Bubble Dynamics in Top View

Fig. 52 shows additional images of the bubble collapses in Fig. 42 and Fig. 43 in top view. The visual appearance is consistent with other works [11]. The depth of field is very shallow, and therefore only the surface and the bubble dynamics very close to it are in focus. The bright-dark rings in the upper-right corner of Fig. 52 ($\gamma = 1.35$) and the lower-right corner of upper right corner Fig. 52 ($\gamma = 1.6$) are caused by ripples in the water/air interface. They are far away from the bubble and do not affect it.

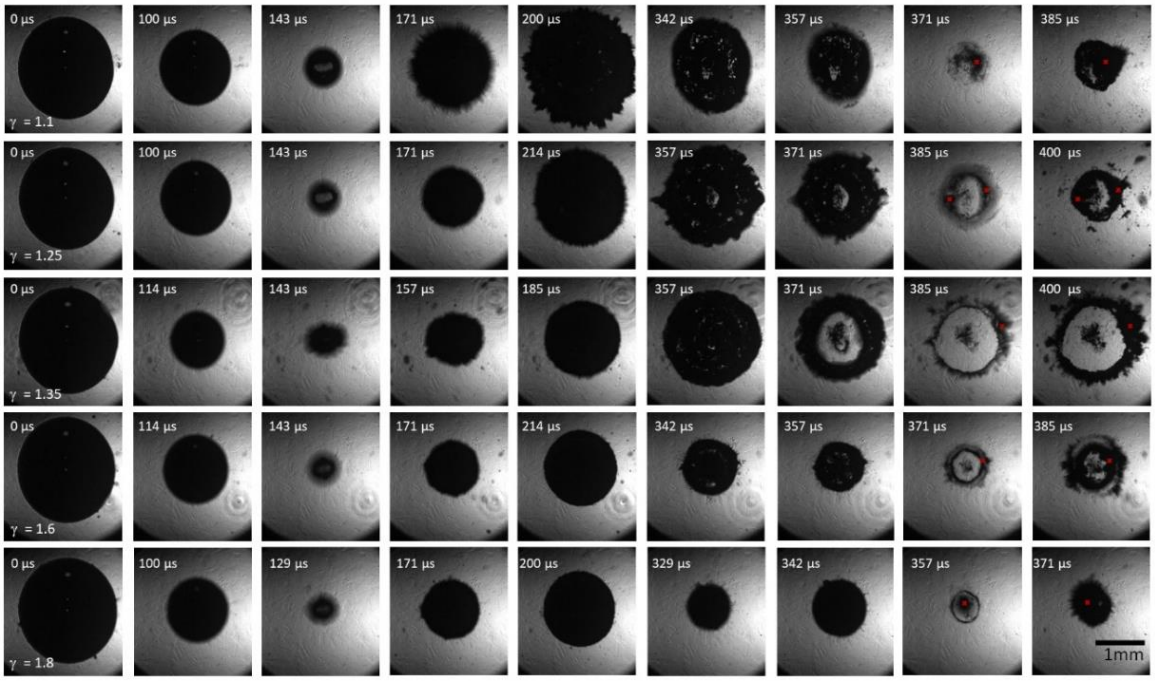

Fig. 52 Additional images of the collapse process of the bubbles shown in Fig. 42 and Fig. 43.

10.1.2 Bubble Dynamics, SCAs, and Pit Locations on NAB

Fig. 53 shows images of bubble collapses at different stand-off distances. Each of the bubbles shown here caused at least one pit. The dynamics are consistent with other work [11, 54, 55]. A discussion of the dynamics can be found in [11].

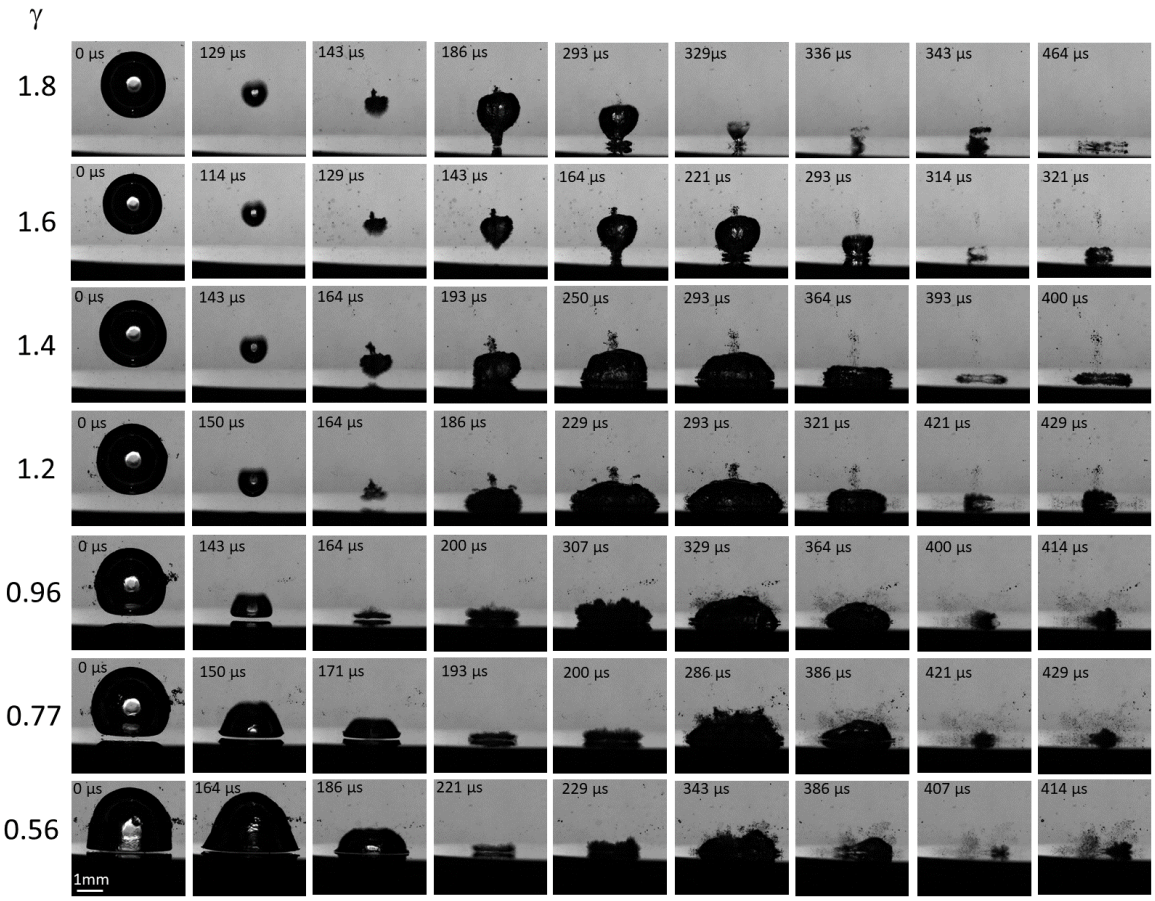

Fig. 53 Selected side-view images of bubble collapses on NAB at different stand-off distances

Fig. 54 shows the second collapse of the bubbles shown in Fig. 53. Pit locations are marked with a red x. Again, the pit location could be linked to SCAs at all stand-off distances.

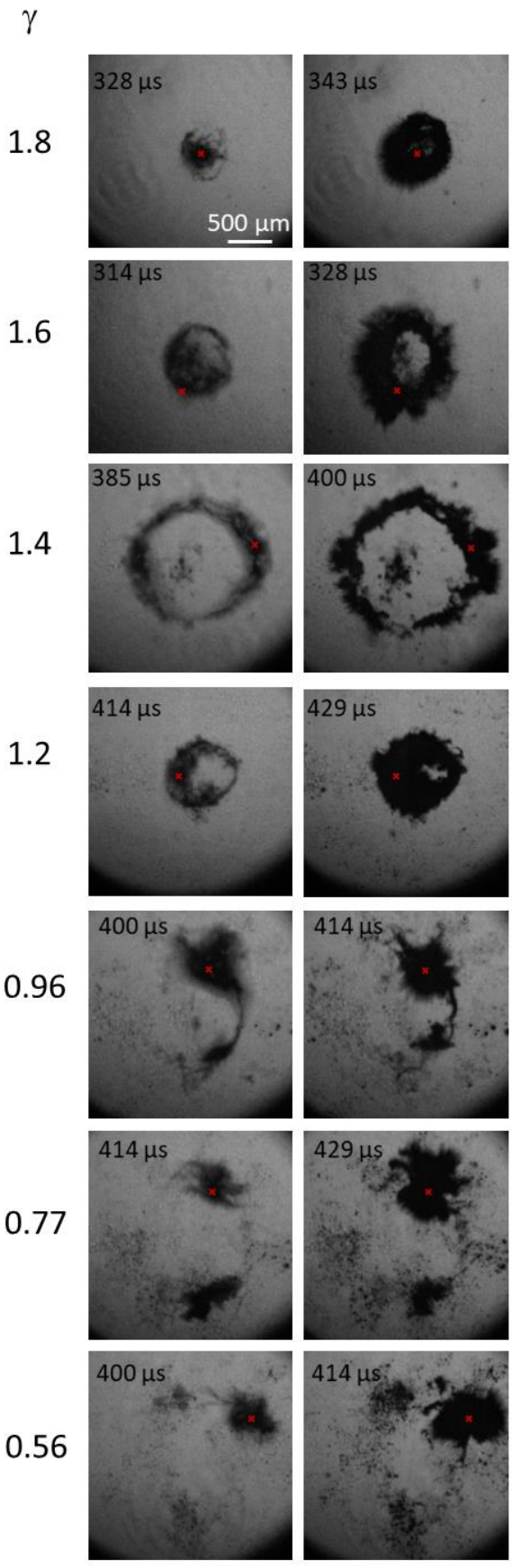

Fig. 54 Top view of the second collapse of the bubbles shown in Fig. 53. The red x marks the location of the pit found after that bubble.

10.1.3 Bubble Detachment

Fig. 55 shows two bubbles at the second collapse. The first bubble is the same shown in Fig. 45 and the second is a bubble from the same bubble sequence that did not cause a pit. The edges of the gas phase are marked in color to aid distinguishing the bubble shape from its reflection on the surface. While the bubble in Fig. 55a is only partially detached from the solid surface, detachment appears almost over the complete torus of the bubble in Fig. 55b.

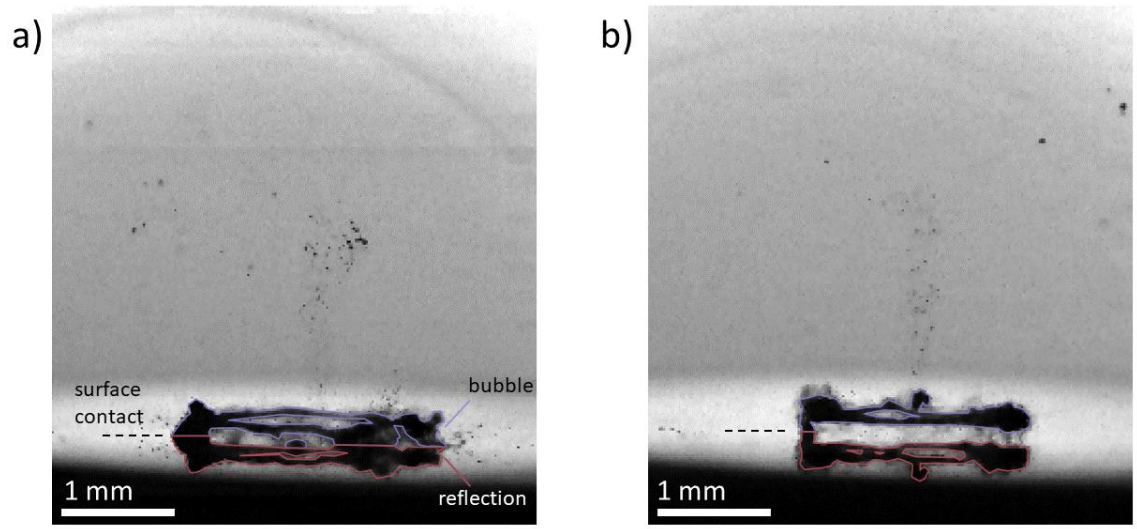

Fig. 55 Second collapse of two bubbles with short illumination. a) The same bubble as in Fig. 45. b) A bubble that did not cause a pit. The edge of the gas phase is marked in blue for the bubble and red for the reflection.

10.1.4 Repetition-Rate Dependence of the Pitting Rate

Fig. 56a shows the pit count at four different bubble repetition rates. After 50 bubbles, there are 25 or 26 pits at all repetition rates. Fig. 56b shows the pitting rate calculated from Fig. 56a. The errors bars represent the uncertainty of the linear fit. All four measurements are quite close. At the highest repetition rate of 5 Hz, the rate slightly decreases. However, the average bubble radius was also slightly lower for this measurement. This may be due to the fact that more dissolved gas bubbles refract part of the laser beam which can result in smaller bubbles. We conclude

that within the range relevant for our experiment, the repetition rate has no significant effect on the pitting rate.

These measurements allow further conclusions regarding the influence of the experimental conditions on pit formation. Fig. 56c and d show example images of the sample in water a few microseconds before the plasma breakdown at a repetition rate of 1 Hz and at 3 Hz. In the latter case, more dissolved gas bubbles are seen in the bulk liquid and also directly on the surface (white arrows) than in the former case. However, the pitting rate is the same. Thus, more dissolved-gas bubbles, which is the main effect of higher frequencies, do not seem to have a significant effect on pitting.

Two aspects can be inferred from the dissolved-gas bubbles in the fluid and the lack of change in pitting rate over the repetition-rate variation. First, these bubbles did not move in the high-speed sequences, indicating that there is no significant flow left in the fluid from the previous bubble. Second, pitting in connection with bubbles on the surface excited by a shock wave – as described in Section 5.3.4 – is not a dominant mechanism in our experiment.

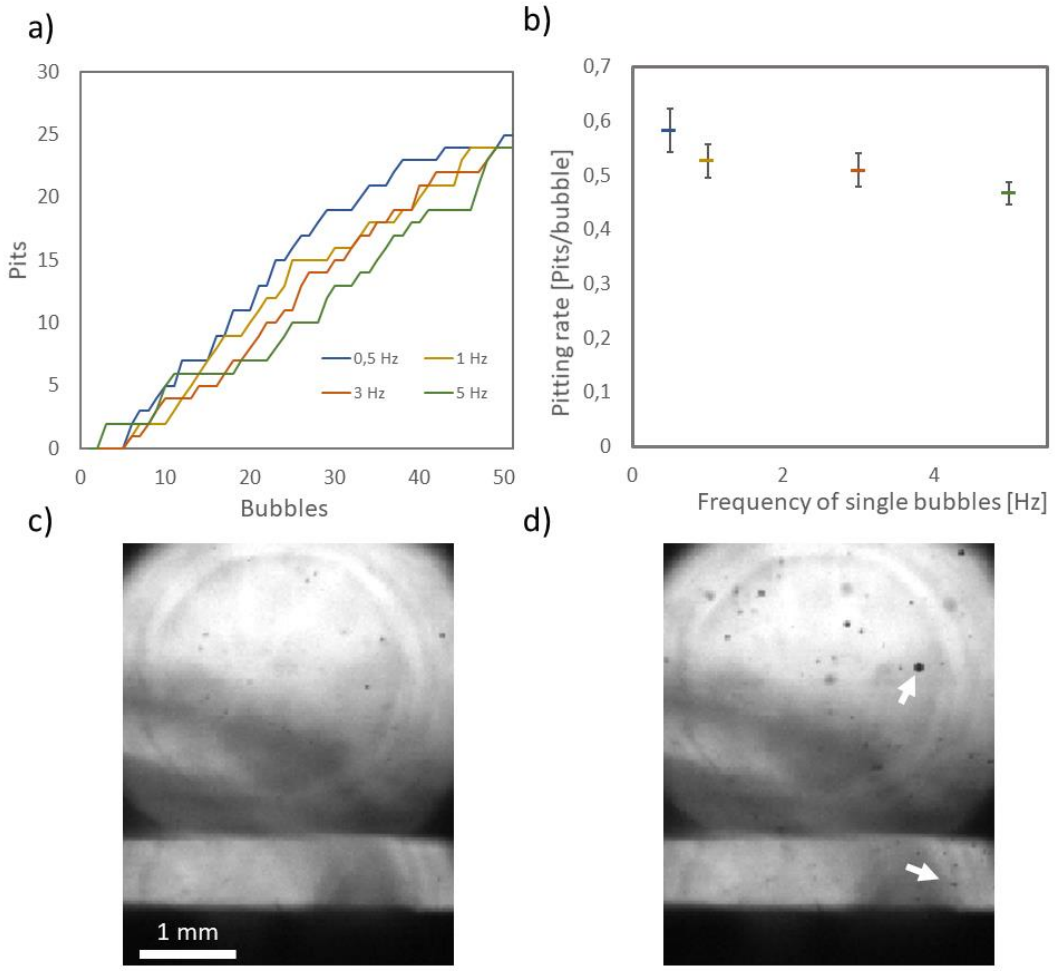

Fig. 56 a) Pit count for 50 bubbles at different frequencies b) Repetition rates dependence of the pitting rate c), d) Liquid in the region where the bubble is induced just before the plasma breakdown at a bubble repetion rate of 1 Hz and 3 Hz, respectively. Arrows mark two of many gas bubbles in the liquid.

10.1.5 Aluminum Example

Fig. 57 shows the damage to an aluminum sample and the first and second collapse of a bubble at γ = 0.5. The first bubble caused a pit (red circle). After fifty bubbles, more pits can be observed in this region (A), but there are also surface changes that do not look like the previously described pits (B). This change appears more like a large-scale displacement of material that builds up over the whole area at the same time. The images of the first collapse (Fig. 57 110 µs, 120 µs) and the second collapse (Fig. 57 250 µs, 260 µs) show that the first collapse is not responsible for the pit. In the second collapse, however, there is a

SCA that can be associated with the pit. In addition, it can be seen that the damaged region (B) lies on the first collapse (red semicircle). In contrast to the technical materials, there is a surface change here that is not in the form of pits and is caused by a wide area of the collapse.

Finally, Fig. 57 also shows a confocal microscope image of the damage after 100 individual bubbles. The material displacement can be seen very well. The center of the bubble collapse is marked with a black X. This is where the liquid jet hits the sample surface. It can be seen that despite the small stand-off distance, no surface change occurred in this area. This shows the limitations of aluminum as a model material in the sense that the damage mode here that cannot necessarily be transferred to technical alloys. On aluminum, damage occurs that can be associated with the initial collapse and cannot be attributed to SCAs and pits. Corresponding damage due to many bubbles at these stand-off distances was not observed on either the 316L or the NAB.

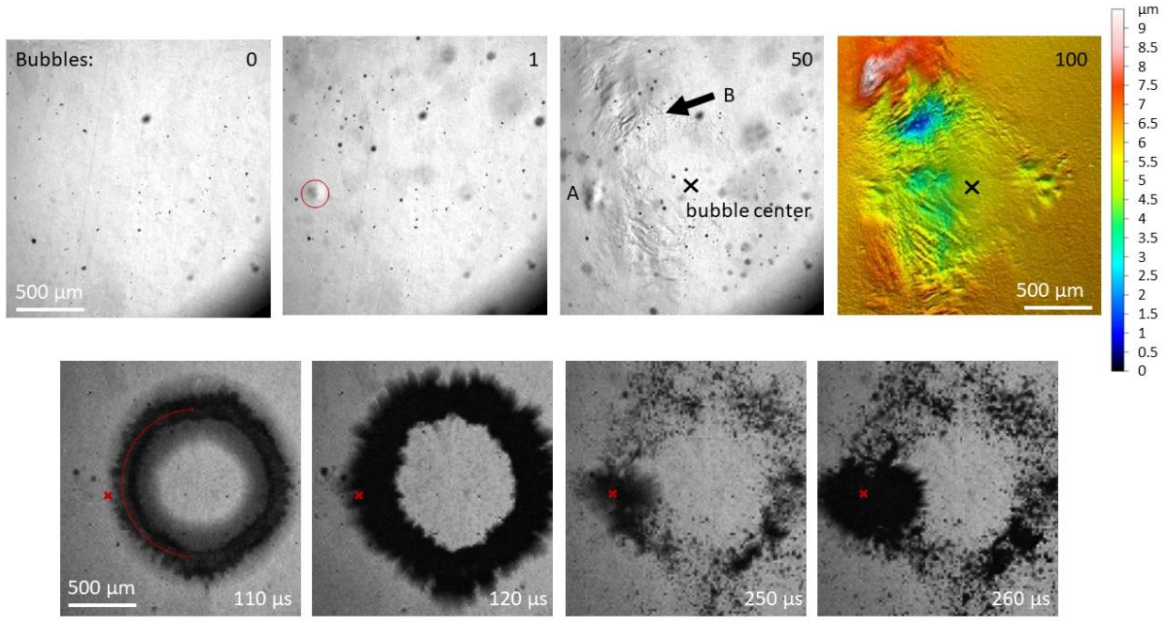

Fig. 57 Aluminum surface after 0, 1, and 50 bubbles in-situ recorded and a confocal recording after 100 bubbles at γ = 0.5 and r = 1.3. Additionally, the first and second collapse of the first bubble are shown. The red x marks the location of the pit found after this bubble.

10.2 Pit Detection via AI

In the presented work pit counting was done by visual inspection (VI). Even if this method works, it is time consuming and might be subjective to the person counting.

As part of a Master thesis [100] supervised by the author, Ersoy established a system to automate the detection of pits using artificial intelligence (AI). More information about object tracking with AI can be found in [101]. The model that was used was Faster R-CNN [100]. This model has proven effective for various scientific applications with labeling objects in the context of material analysis [102, 103].

The material used for this project was 316L. In 135 full-size images (2560 x 2160 pixels) 17.725 pits were annotated. The images were subdivided into patches of 512 x 432 pixels. The annotated images were used for training and validation of Faster R-CNN.

As an individual image is typically part of larger series of images, the detection was supplemented by a SORT algorithm and a persistence analysis – an established method in video tracking [104]. Fig. 58 shows the used programs and their functions. After the detection of individual images, the SORT algorithm links pits over images to tracks. The persistence analysis then uses criteria like the short interruption of tracks or the track being consistent to the end of the series of images to fill in missing pits or delete tracks that were falsely assigned to a pit.

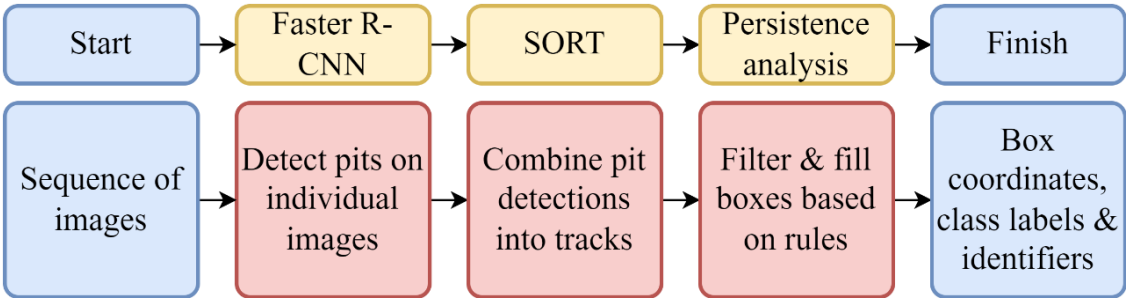

Fig. 58 Schematic view of the used programs for pit detection and their functions. (adapted from [100])

Fig. 59 shows an example of an evaluation by the AI system compared to visual inspection. Both the pit count and the pitting rate are shown. Bubbles were at $\gamma = 1.35$ and had maximum bubble radius of r = 1.95 mm. The general trend of the pit count of all curves is quite similar (Fig. 59 i & ii). Only the blue curve (S58) shows

a slightly lower value overall. The same applies to the resulting pitting rates (Fig. 59 iii & iv). In detail, the pitting count determined by the AI shows a higher fluctuation. This is caused by the fact that pits are re-evaluated in each image and can disappear and reappear depending on the image. In addition, it should be noted that visual inspection itself is prone to errors. Therefore, any deviation between the results of visual inspection and those generated by the AI system does not necessarily indicate an error of the AI system.

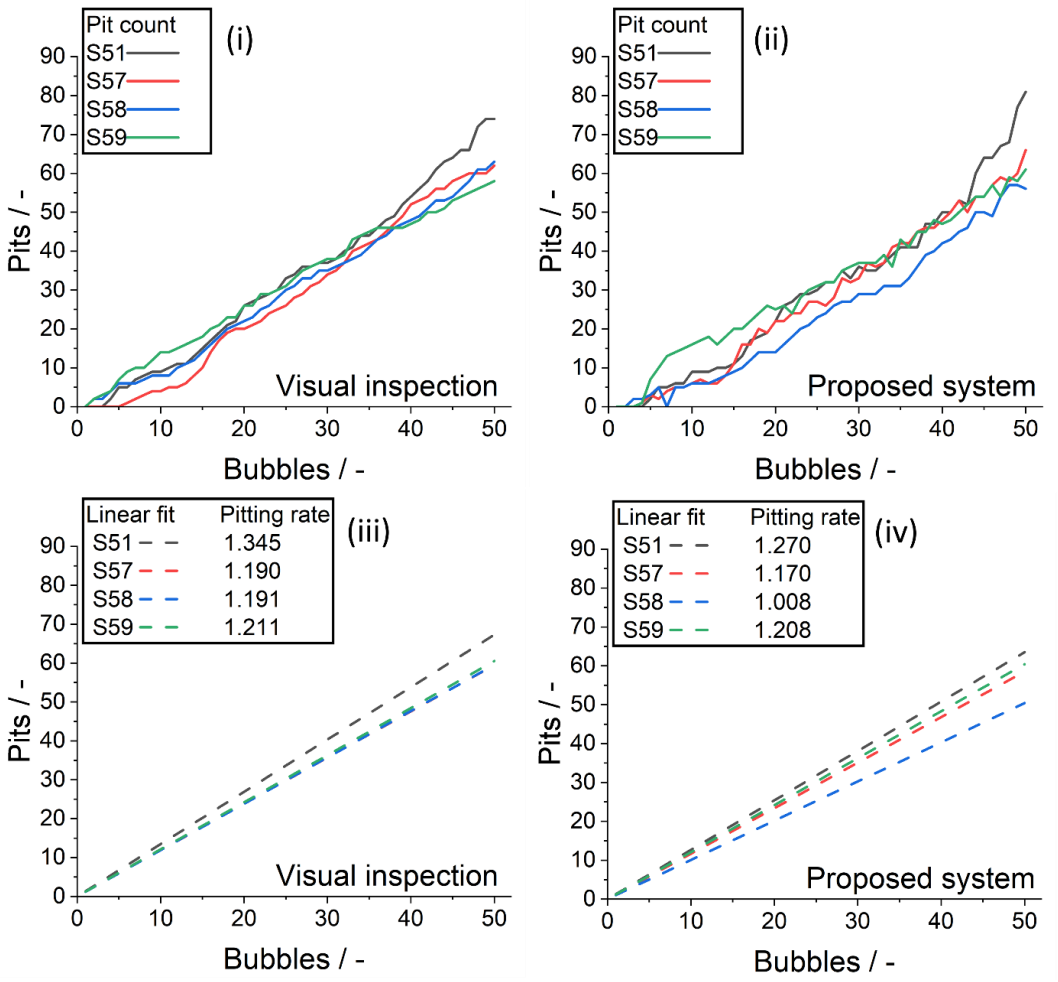

Fig. 59 Pit count and pitting rate of four sample evaluated by visual inspection and the AI system (adapted from [100]).

Fig. 60 shows data from Fig. 49a (blue, [60]) which is extended with data from the AI project (orange) stemming from experiments with larger radii. In contrast to the measurements presented above, fewer parameters varied here, but more measurements were carried out for each combination of γ and r. This makes it easier to estimate the dispersion of the pitting rate and thus the significance of the

values. For this purpose, the figure also contains mean values and standard deviation at points r = 1.65 and r = 1.95. The pitting rate represented by the blue points (VI) was also compared to the AI evaluation and showed good agreement. A more detailed discussion is beyond the scope of this section but can be found in [100].

Overall, the linear trend found for smaller radii is seen to continue for larger radii. However, the pitting rate fluctuates significantly more with constant experimental parameters than for the lower radii. Also, the possible number of pits found after a single-bubble collapse was up to five pits on 316L (it was three for smaller radii). This might explain the larger standard deviation.

The AI evaluation was significantly faster than with visual inspection and looks promising for further experiments.

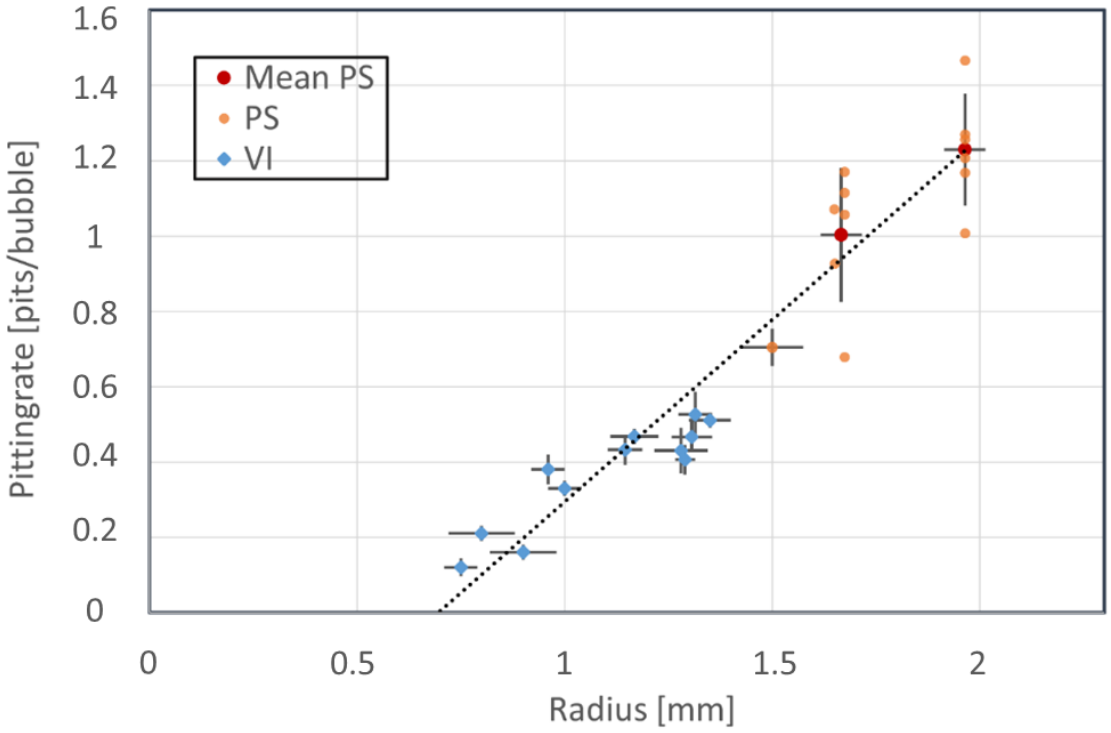

Fig. 60 Pitting rate versus radius at $\gamma = 1.35 \pm 0.05$. Data from Fig. 49a (blue, [60]) extended with data from the AI project (orange) (adapted from [100]).

10.3 Plasma Formation and Visualisation

An important part of this work is the generation of bubbles. A bubble in an experiment is never perfectly spherical – neither flow-induced nor laser-induced

bubbles are. Nevertheless, for the best comparison to simulations, as discussed in Section 3.2, and to avoid further complexty of experiments, the experiments typically aim at bubbles that are as close to spehrical as possible. To that end, the shape of the plasma breakdown is crucial. This chapter presents some investigations on plasma shape and its optimization. The in-situ microscope was used to study the plasma shape.

The wavelength of the laser is important for laser-induced single bubbles. Fig. 61 shows 3 single shots as well as the mean and the standard deviation of 50 shots of recordings of the plasma for 1064 nm and 532 nm laser wavelengths. The single shots with both wavelengths show plasma breakdown in a similar region. However, consistent with previous studies, the plasma is fragmented into many smaller entities (also shown in Fig. 63b) [10]. The main difference between the plasmas at the two wavelengths is that these small entities appear smaller at 532 nm. However, the bubbles did not differ significantly for the two wavelengths. This indicates that single-bubble experiments are most likely roughly comparable across wavelengths.

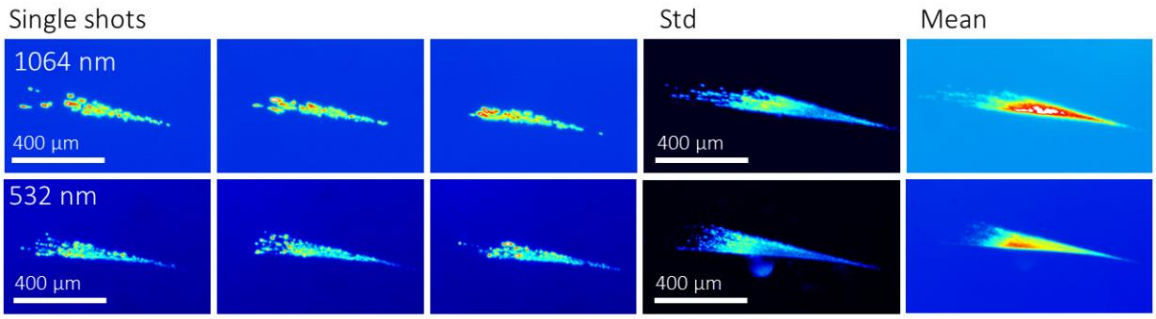

Fig. 61 Three single shots of the plasma formation as well as the standard deviation and the mean of 50 single shot.

Fig. 62 shows a scheme for the spatial formatting of the laser beam. First, the beam is expanded and passes a first aperture. An axicon is used to shape the beam into a ring. A second axicon realigns and collimates the now toroidal beam. It can be moved along the optical axis to define the ring diameter. Following the axicon a second aperture is used to reduce the thickness of the ring from the outside. This ring is then focused into the cuvette filled with water. The focus of an aspheric lens is corrected with an additional lens because the aspheric lens is optimized for focusing in air and not water. Not shown in Fig. 62 is an attenuator that consists of

a half-wave plate and a Brewster window. With this element the laser energy, and therefore bubble radius, can be adjusted. The improvement of the plasma through this arrangement is presented in the next paragraph. The idea of shaping the laser beam into a ring was based on the observation that the plasma does not form mainly at the beam waist, but in the conical area in front of it (see Fig. 61). Therefore, it is important to minimize the volume in which the absorption of energy is sufficient to trigger a plasma breakdown. Furthermore, this means a perfect optimization of the focus alone is not sufficient to avoid an elongated plasma.

The apertures and ring size were adjusted to yield the shortest plasma length with minimal pulse-to-pulse variation due to laser mode fluctuation.

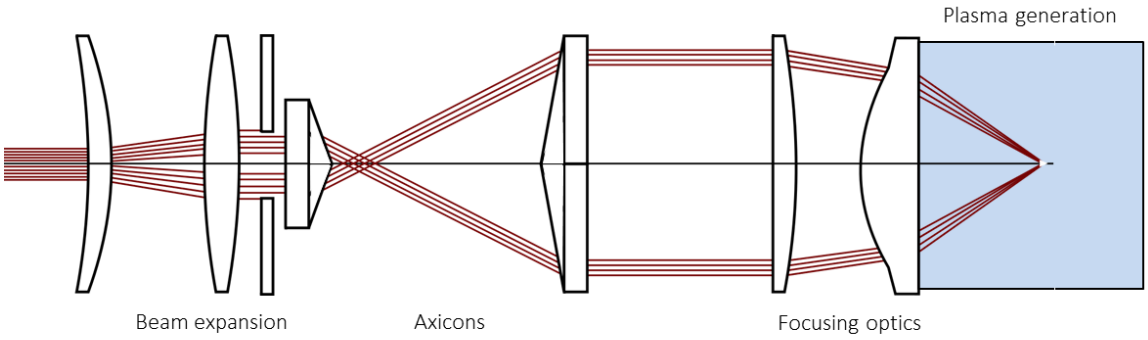

Fig. 62 Optical setup for laser beam formatting with paired axicons

Fig. 63 gives a comparison of the plasma shape achieved with these axicon optics with the plasma shape published in the previous work of Sagar et al. [10] without axicons. In the work of Sagar et al. the focus angle was already identified at an important parameter of plasma optimization following the idea of a minimized volume of the plasma breakdown presented above. However, Fig. 63 shows an improvement of the plasma, which is more than halved in length in comparison to the previous work. Additionally, the plasma of the new arrangement is more axisymmetric along the beam direction, which is most likely due better centering of the optics, which is crucial for the axicon arrangement.

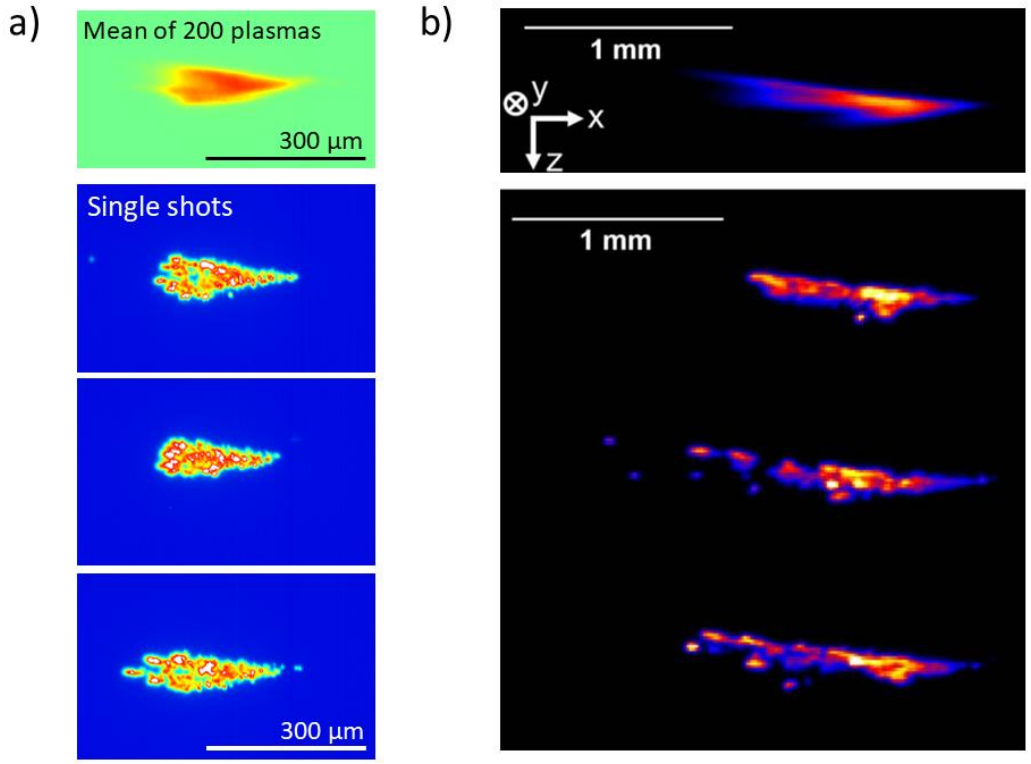

Fig. 63 a) Plasma with axicon arrangement shown in Fig. 62 b) Plasma in previous work without axicons (adapted from [10])

10.4 Grain Size and Pitting

Despite the observation that especially the summation of many pits can lead to a damaging of the material through adding up plastic deformation, Fig. 64 shows one pit that individually already induced a surface change on 316L beyond its plastic deformation. A change of the grain boundaries is clearly visible after the occurrence of the pit. For this to occur it is most likely needed that the grain itself is quite small and is not that much larger than the pit. Here, the plastic flow of just one pit seems to be already stopped at the grain boundaries closest to the pit. This supports the idea that grain size is a very relevant parameter in experiments investigating cavitation damage and the formation of erosion.

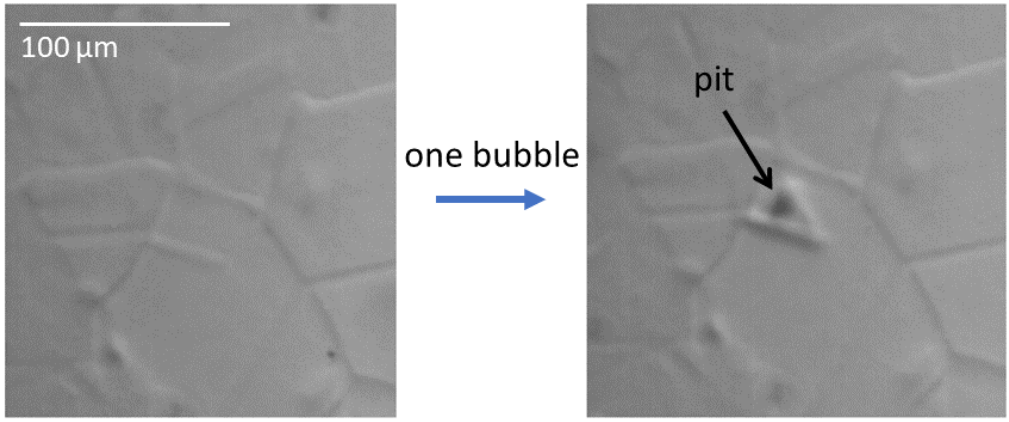

Fig. 64 Effect on grain boundaries from just a single pit from a bubble at r = 1.25 mm and γ = 1.4 on 316L